WARSAW UNIVERSITY OF TECHNOLOGY

Ph.D. Thesis

Physical Sciences/
Natural Sciences

Magdalena Dobrowolska, M.Sc.

Muon Scattering Tomography as a Tool For Inspection of Large and Reinforced Concrete Structures

Supervisor
Ph.D. D.Sc. Eng. **Daniel Kikoła**

Assistant Supervisor
prof. dr **Jaap Velthuis**

Warsaw 2025

Acknowledgements

Many people have crossed my path during the preparation of this thesis, and I am very grateful to all of them. I would like to express special thanks to my supervisors, Dr Daniel Kikoła and Prof. Jaap Velthuis. I am especially grateful to Jaap for encouraging me to write this thesis in the first place. I sincerely appreciate both of my supervisors for their openness to my many questions, for their valuable guidance, and for their endless patience. I also owe particular thanks to Daniel for his support throughout the process of obtaining my degree externally. I am grateful to both of them for creating such a friendly and supportive atmosphere.

I would also like to thank the entire Particle Physics Group from the University of Bristol for their help and kindness, especially Dr Chiara De Sio, Dr Lana Beck, and Keith Clark for their support, friendship, encouragement, and constant smiles that made my work so much more enjoyable.

Finally, I would like to thank my loved ones, who were by my side throughout this journey.

For Jaap

Abstract

Different branches of industry need non-invasive solutions for non-destructive testing. Especially in civil engineering, there are major challenges, where thick, reinforced concrete structures must be checked regularly. Many different methods already exist, but they do not fulfill all the requirements for inspections of civil structures. Common methods for the detection of rebars in concrete have limited penetration depths, which are not satisfactory for vast concrete constructions.

Muon scattering tomography is a non-destructive and non-invasive method which shows great potential for a high-depth, 3D imaging and can address remaining challenges in civil engineering. It uses cosmic muons as probes, which are free, highly-penetrating, ubiquitous particles that are part of the naturally occurring background radiation. Their flux at sea level is about 10 000 $\mathrm{m^{-2}min^{-1}}$.

This dissertation presents applications of muon scattering tomography to detect, locate, measure and image different configurations of steel reinforcement structures within big concrete buildings. The work was done in cooperation with an industrial partner based on Monte Carlo simulations of a system of detectors and a scanned object. Using a cosmic ray database, the behavior of muons while passing through detectors and a concrete object was simulated. The parameters of the detector system used in the simulations correspond to the actual parameters of an existing prototype detector system.

The presented method is based on the reconstruction of muon tracks and establishing an estimated place of the scattering - a vertex. The distances between the vertices and the scattering angles are used to implement a reconstruction method. The method was further developed here for structural engineering needs.

This thesis presents a method for detecting and measuring reinforcement bars, showing that bars with a minimum diameter of 33.7±7.3 mm and a length of 100 cm can be detected using the developed method. For reinforcement bars with a volume above 2 500 cm^3, the volume was reconstructed with a resolution of 5.4±0.3%. Further studies have shown that when using the fact that the reinforcement is a repetitive structure and periodic signal can be detected using a Fourier transform, the minimal detectable diameter of a 100 cm long rebar can be decreased to 6 mm, when the rebar is a part of a bigger reinforcement network. In the resulting spectrum, the peak amplitude depends on the rebar diameter and the peak locations indicate the spacing between the rebars. Furthermore, a method was developed to distinguish between the presence of one and two reinforcement grids and to locate the depth of the second layer of the grid. What is more, a method to image the interior of a scanned concrete block is also presented. With this method it is possible to locate objects in concrete.

In the dissertation a prototype system for muon tomography using CO_2 was also characterized. Since stricter rules for the use of greenhouse gases in scientific experiments have come into force, previously employed freon was not allowed to used in the muon system again. Therefore, it was attempted to run the system with CO_2 instead. However, the required resolution and efficiency could not be obtained when using CO_2.

The last chapter focuses on using scattering tomography methods for imaging in proton therapy. Initial research showed that it was possible to distinguish four materials from one another: soft tissue, bone, air and uranium. Then, a human phantom was simulated, where the ribs were successfully distinguished from the surrounding tissue.

Key words: Muon Scattering Tomography, cosmic muons, 3D imaging, concrete imaging, reinforcement location, rebar location

Streszczenie

Wiele branży przemysłowych potrzebuje nieinwazyjnych metod obrazowania w celu zapewnienia bezpieczeństwa i wysokiej jakości swoich usług. Szczególne wyzwania występują w budownictwie, ponieważ wielkie, żelbetowe budowle muszą być regularnie sprawdzane. Istnieją różne techniki obrazowania i inspekcji, ale nie spełniają one wszystkich wymagań dotyczących kontroli takich obiektów. Powszechnie dostępne metody wykrywania prętów zbrojeniowych w betonie mają ograniczoną głębokość penetracji, która nie zawsze jest wystarczająca.

Tomografia rozproszeniowa mionów jest nieniszczącą i nieinwazyjną metodą, która daje duże możliwości trójwymiarowego obrazowania na dużej głębokości. Wykorzystuje ona kosmiczne miony, które są częścią promieniowania tła. Charakteryzują się one dużą przenikliwością materii, są powszechnie dostępne, a ich strumień nad poziomem morza wynosi około 10 000 $\mathrm{m}^{-2}\mathrm{min}^{-1}$.

Niniejsza rozprawa przedstawia techniki do wykrywania, lokalizacji, pomiaru i obrazowania stalowych zbrojeń w dużych strukturach betonowych przy użyciu tomografii rozpraszania mionów. Metody te zostały opracowane we współpracy z partnerem branżowym na podstawie symulacji Monte Carlo. Scenariusze obejmowały system detektorów oraz betonowy obiekt ze zbrojeniem wewnątrz. Przy użyciu bazy danych promieniowania kosmicznego zasymulowano zachowanie mionów podczas przechodzenia przez detektory i betonowy obiekt. Parametry systemu detektorów użyte w symulacjach odpowiadają rzeczywistym parametrom prototypowego systemu detektorów.

Opracowane metody opierają się na rekonstrukcji torów lotu mionów i ustaleniu przybliżonego miejsca ich rozproszenia mionów - wierzchołka rozpraszania. Następnie, odległości między wierzchołkami i kąty rozproszenia są wykorzystane w metodzie metrycznej. Jest ona podstawą, na której bazowano, opracowując techniki inspekcji żelbetowych konstrukcji.

W niniejszej rozprawie przedstawiono metodę detekcji i pomiaru prętów zbrojeniowych. Wykazano, że pręty o minimalnej średnicy 33,7±7,3 mm i długości 100 cm można wykryć przy użyciu opracowanej metody. Dla prętów zbrojeniowych o wymiarach powyżej 2 500 cm^3, objętość zrekonstruowano z rozdzielczością 5,4±0,3%. Dalsze badania wykazały, że minimalna średnica pręta o długości 100 cm możliwa do detekcji możne zostać obniżona do 6 mm wykorzystując fakt, że siatka zbrojeniowa jest strukturą powtarzalną, a sygnał okresowy można wykryć za pomocą transformaty Fouriera. W otrzymanym widmie amplituda piku zależy od średnicy pręta zbrojeniowego, a położenie pików zmienia się wraz ze zmianą odstępu między prętami zbrojeniowymi. W dalszej części pracy opracowano sposób rozróżniania jednej od dwóch warstw siatki zbrojeniowej oraz lokalizowania położenia obydwu siatek. Ważnym elementem rozprawy doktorskiej jest technika obrazowania wnętrza skanowanego obiektu. Dzięki niej możliwe jest zlokalizowanie przedmiotów znajdujących się w betonie.

W rozprawie scharakteryzowano również prototypowy system do tomografii mionowej wykorzystujący CO_2. Poprzednio stosowany freon, który jest gazem cieplarnianym, nie mógł być ponownie użyty ze względu na ścisłe przepisy dotyczące wykorzystywania gazów cieplarnianych w eksperymentach fizycznych. Istnieje więc pilna potrzeba znalezienia zamienników zapewniających zadowalającą rozdzielczość i wydajność.

W ostatnim rozdziale skupiono się na możliwości zastosowania metod tomografii rozproszeniowej do obrazowania w terapii protonowej. Wstępne badanie wykazało, że możliwe jest odróżnienie od siebie czterech materiałów: tkanki miękkiej, kości, powietrza i uranu. Następnie, zasymulowano ludzki fantom, w którym pomyślnie odróżniono żebra od otaczających je tkanek.

Słowa kluczowe: tomografia mionowa, kosmiczne miony, obrazowanie 3D, obrazowanie betonu, lokalizacja zbrojenia, lokalizacja prętów zbrojeniowych

Declaration

This thesis mainly focuses on the challenge of locating rebars in concrete with muon tomography based on Monte Carlo simulations. In addition, a detector setup operated with CO_2 was used to gather experimental data. The potential of the scattering technique for the proton radiotherapy was tested as well. The development of muon tomography for rebar detection, location, measurements and imaging was fully the work of the author. The technique is based on previous work done at the University of Bristol on the development of muon tomography for the detection of smuggled high-Z materials [1, 2] The author employed Geant4 simulations from [1, 2], further developed them and used to perform research in chapters 5, 6, 7. The Bristol discriminator algorithm which was the starting point for the analysis presented in chapters 5, 6, 7, 8 and 9 was described in detail in [1]. The phantom Geant4 simulations used in chapter 9 were based on code provided in advanced examples in the Geant4 framework and further developed by the author. Further development of the analysis methods presented in these chapters and software was entirely written by the author. The simulations were conducted by the author using the computing resources of the University of Bristol's Advanced Computing Research Centre (http://www.bris.ac.uk/acrc/). The detector system presented in chapter 8, was a further development of an existing system [3]. The author further developed the readout system to allow the use of modern FPGAs, which required an update of the DAQ. In addition, software required to perform analysis of the collected data shown in chapter 8 was entirely written by the author.

Contents

1 Scientific achievements and research outputs 15

1.1 Remaining research outputs 17

2 Non-destructive imaging of civil structures 19

2.1 Existing inspection methods 20
  2.1.1 Ground penetrating radar 20
  2.1.2 Active infrared thermography 21
  2.1.3 Ultrasonics 23
  2.1.4 Radiography 24
  2.1.5 Remaining challenges 25

3 Muon imaging methods 27

3.1 Relevant physics of muon imaging methods 27
  3.1.1 Cosmic rays 27
  3.1.2 Muons 28
  3.1.3 Muon interactions with matter 28
  3.1.4 Energy loss of muons 29
  3.1.5 Multiple scattering 30
3.2 Muon techniques 32
3.3 Muon radiography 32
3.4 Muon scattering tomography 33
  3.4.1 Determine the muon path in matter 34
  3.4.2 PoCA 34
  3.4.3 Bristol discriminator algorithm 35
3.5 Limitations of muon methods 38

4 Monte Carlo simulations of the detector prototype 39

4.1 Geant4 39
  4.1.1 A database of cosmic ray data - CRY 39
4.2 Detector setup 40

5 Muon Scattering Tomography as a tool for detection and imaging of rebars 43

5.1 Study of reinforced concrete 43
  5.1.1 Case 1: Rebar inside a variable size concrete block 43
  5.1.2 Case 2: Rebar inside fixed size concrete block 43

5.1.3 Case 3: Reinforcement in concrete 44
5.2 Signal extraction 44
5.2.1 Signal in a variable-sized concrete block 46
5.2.2 Signal in a fixed-sized concrete block 46
5.2.3 Reconstruction of the rebar volume in the concrete object 47
5.2.4 Imaging of a single rod 47
5.2.5 Imaging of reinforcement 52
5.3 Conclusions 58

6 Improvement of the method for the detection of reinforcement in concrete 59
6.1 Simulation study scenarios 59
6.2 Improved background removal 59
6.3 Exploiting the periodicity of the reinforcement 60
6.4 Dependence on the rebar diameter 64
6.5 Extracting the rebar spacing 64
6.6 Detecting the smallest rebars used in industry 65
6.7 The effect of detector geometry and resolution on the performance of the method 73
6.7.1 Method performance as a function of detector resolution 73
6.7.2 Method performance as a function of different number of detector layers 73
6.8 Conclusions 77

7 The study of two layers of reinforcement grid in a concrete object 79
7.1 Simulation setup 79
7.2 Development of method to localize second reinforcement grid 79
7.3 Results of the adapted method 80
7.4 Conclusions 84

8 Experimental studies 85
8.1 Introduction 85
8.2 The muon tracker 85
8.2.1 High-resolution resistive plate chambers 85
8.2.2 Gas selection 86
8.2.3 Mechanical structure 87
8.3 MAROC3 88
8.4 Data format 89
8.5 Pedestal and noise calculation 90
8.5.1 Preparing raw data for pedestal calculation 90

8.5.2 Pedestal and noise calculation 91
8.5.3 Common mode noise correction 93
8.5.4 Improved random noise estimate 94
8.6 Hit finding 97
8.6.1 Hit characteristics 97
8.6.2 Dead strips within a cluster 99
8.6.3 Inverted hit correction 99
8.7 Track reconstruction 102
8.7.1 Track candidates and timestamp matching 102
8.7.2 Sanity check on track candidates 103
8.7.3 Event display 106
8.7.4 Track finding 106
8.8 Residual and spatial resolution 107
8.8.1 Residual 107
8.9 Spatial resolution 107
8.10 Efficiency 108
8.11 Imaging of the concrete object 110
8.12 Conclusions 112

9 Scattering tomography for proton radiotherapy **113**
9.1 Simulation setup 114
9.1.1 Basic material description 115
9.1.2 Distinguishing between tissues in the human phantom 115
9.2 Conclusion 120

10 Future development of the methods **121**

11 Summary **123**

1 Scientific achievements and research outputs

This doctoral dissertation is partially based on a collection of articles on applications of muon scattering tomography in inspection of big concrete structures published in well-known, peer-reviewed journals during the period of 2018-2022. Research for author's first publication (M. Dobrowolska et al 2018 JINST **13** P05015) was carried out during masters course and was included in master's thesis. Remaining articles and contributions to scientific conferences were produced while working as a research associate at the University of Bristol between 2018 and 2023 and later as an honorary research associate of the University of Bristol and as well as through work carried outside academia.

A complete list of peer-reviewed articles:

1. Dobrowolska M., Velthuis J., Frazão L., Kikoła D., *A novel technique for finding gas bubbles in the nuclear waste containers using Muon Scattering Tomography*, JINST, **13** (2018) P05015.

   DOI: https://doi.org/10.1088/1748-0221/13/05/P05015
   $\mathrm{IF}_{2022} = 1.3$

2. Dobrowolska M., Velthuis J., Kopp A., Perry M., Pearson P., *Towards an application of muon scattering tomography as a technique for detecting rebars in concrete*, Smart Mater. Struct. **29** (2020) 055015.

   DOI: https://doi.org/10.1088/1361-665X/ab7a3f
   $\mathrm{IF}_{2022} = 4.1$

3. Dobrowolska M., Velthuis J., Kopp A., De Sio Ch., Milne R., Pearson P., *Development of muon scattering tomography for a detection of reinforcement in concrete*, Eng. Res. Express **3** (2021) 035037.

   DOI: https://doi.org/10.1088/2631-8695/ac21a8
   $\mathrm{IF}_{2022} = 1.7$

4. Dobrowolska M., Velthuis J., De Sio Ch., Kopp A., Milne R., Pearson P., *Development of muon scattering tomography for detection of reinforcement in concrete*, JINST **17** (2022) C09011.
   Peer-reviewed proceedings of 12th International Conference on Position Sensitive Detectors, 12-17 September 2021, Birmingham, U.K.

DOI: https://doi.org/10.1088/1748-0221/17/09/C09011
$\mathrm{IF}_{2022} = 1.3$

5. Mhaidra M., Alrheli A., Barker D., De Sio Ch., Kikoła D., Kopp A., Stowell P., Thompson L., Velthuis J., Weekes M., Dobrowolska M., *3D imaging of gas bubbles in nuclear waste containers via Muon Scattering Tomography*, Progress in Nuclear Energy **186** (2025) 105803.

   DOI: https://doi.org/10.1016/j.pnucene.2025.105803
   $\mathrm{IF}_{2024} = 3.2$

6. Abu Sabah L., Ballisat L., De Sio Ch., Dobrowolska M., Chambers A., Duan J., Guatelli S., Sakata D., Shi Y., Velthuis J., Rosenfeld A., *AlphaGlue: A novel conceptual delivery method for α therapy*, BioMedInformatics **5** (2025) 58.

   DOI: https://doi.org/10.3390/biomedinformatics5040058
   $\mathrm{IF}_{2024} = 3.4$

Apart from articles, I contributed to scientific conferences by giving talks and presenting posters:

1. Frazão L., Dobrowolska M., Poole C., Kikoła D., Tietze-Jaensch H., Velthuis J., *Measurement of Gas Bubbles Encased in Bitumen Nuclear Waste Drums with Muon Scattering Tomography*, co-author of the results presented by Frazão L. on Waste Management 2018, March 18-22, 2018, Phoenix, Arizona, USA
   proceedings available at: https://www.xcdsystem.com/wmsym/2018/pdfs/FinalPaper_18237_0117065458.pdf

2. Dobrowolska M., Kopp A., Velthuis J., *Muon Scattering Tomography as a novel technique in rebar and crack detection*, poster presented by me on Nuclear Frontiers 2019 Conference, January 15, 2019, Bristol, UK

3. Dobrowolska M., Kopp A., Velthuis J., Perry M., Pearson P., Cooke Ch., *Muon scattering tomography as a method for detecting rebars and cracks in concrete*, first author of the poster presented by Cooke Ch., at the 2019 IEEE Nuclear Science Symposium and Medical Imaging Conference, October 26-November 2, 2019, Manchester, UK

4. Mhaidra M., Kopp A., Alrheli A., De Sio Ch., Barker D., Stowell P., Weekes M., Dobrowolska M., Kikoła D., Thompson L., Velthuis J., *A robust method to find gas bubbles inside large nuclear waste containers using muon tomography*, co-author of the results presented by Mhaidra M. on Waste Management 2021, March 8-12, 2021, Phoenix, Arizona, USA
   proceedings available at `https://s3.amazonaws.com/amz.xcdsystem.com/A464D2CF-E476-F46B-841E415B85C431CC_abstract_File698/FinalPaper_21151_0206050115.pdf`
5. Dobrowolska M., *Development of muon scattering tomography for a detection of reinforcement in concrete*, speaker on The 12th International Conference on Position Sensitive Detectors, September 12-17, 2021, Birmingham, UK
   proceedings available at `https://doi.org/10.1088/1748-0221/17/09/C09011`
6. Dobrowolska M., *Development of muon scattering tomography for a detection of reinforcement in concrete*, speaker at the Virtual 2021 IEEE Nuclear Science Symposium and Medical Imaging Conference, IEEE, October 16-23, 2021, Yokohama, Japan

1.1 Remaining research outputs

As of the date of submission, the following article has been accepted for publication:

1. Bożek R., Dobrowolska M., Obłuski A., Velthuis J., Zabari N., Katrankova K., *Rozwój metod analizy strukturalnej stanowisk archeologicznych i formacji geologicznych oraz pojedynczych obiektów dziedzictwa kulturowego przy zastosowaniu nieniszczącej metody radiografii i tomografii mionowej.*

As of the date of submission, the following article was under peer review:

1. Bożek R., Chabera M., Dobrowolska M., Bielewicz M., Zabari N., Kiecana M., Katrankova K., *Identification of archaeological heritage using non-invasive cosmic muon imaging methods.*

2 Non-destructive imaging of civil structures

Maintaining civil infrastructures safe and reliable for daily use is of high importance. Operation and maintenance become more complex with the increased age of structures. The process of determining and tracking structural integrity and assessing the nature of damage in a structure is often referred as health monitoring.

Non-destructive evaluation (NDE) methods are crucial for health monitoring. Current NDE methods (see chapter 2.1) cover a subset of inspection challenges but there are still some areas where one does not have sufficient tools for inspection yet. In addition, several of the available techniques are not always safe to operate. Challenges remain for larger structures like bridges, buildings etc. Civil and construction engineering need a non-invasive tool to assess the location, type and quality of reinforcement placed at great depths in concrete structures. In particular, old buildings are challenging, because construction records may not exists any more so NDE methods are the only way to gain information about the internal state of the buildings. Human mistakes or neglection is another element that can lead to serious design errors and defects that could be found during inspections [4]. A reliable control method may prevent tragic failures of a big concrete structures like a collapse of the Morandi bridge in Italy in 2018 or the Carola Bridge (Carolabrücke), which fell into the Elbe River in Dresden in 2024.

This work focuses on unsolved challenges of non-destructive inspection of big concrete buildings using muon scattering tomography (MST). As MST has been successfully used for the detection of lumps of high-density materials like uranium in concrete, it should also be applicable to the detection of rebars in vast concrete structures. However, it is still a big challenge because the thinnest rebars used in industry have a 6 mm diameter [5, 6] and are mostly made from iron which has a much lower atomic number than uranium. The smallest lump of uranium that can be detected in concrete cylinder of 13 cm radius and 40 cm length, inside a 1.5 mm thick steel container is $50 \times 50 \times 50$ mm^3 [7]. Thus novel methods need to be developed to detect the iron rods.

This thesis is organized as follows. Firstly, in chapter 2.1, the state-of-the-art in inspection methods are reviewed. Secondly, muon imaging methods and the physics principles behind muon interactions with matter are presented in chapter 3. Chapter 5 shows a proof-of-principle method to detect a single iron rod embedded in concrete and to image it. Next, an improved algorithm to detect smaller rods is demonstrated in chapter 6. In chapter 7, the way to distinguish between one and two layers of reinforcement is shown. In addition, the experimental verification of the method is presented in chapter 8 using CO_2. Last but not the least, the application of the methods developed for muon scattering tomography to the challenge of real time proton radiotherapy was studied in chapter 9.

2.1 Existing inspection methods

The challenge of inspecting reinforced concrete structures is very complex. A lot of NDE methods exist [8, 9, 10, 11, 12] to perform such inspections. Most commonly used techniques are ground penetrating radar (GPR) [13, 14, 15, 16], infrared thermographics [15, 17, 18], ultrasonics [19, 20, 21, 22], X-ray [23, 24]. They all have their own range of applicability. Comparison of detection capability ranges of most commonly used methods is shown in figure 1. All of the techniques are suitable for shallow, less than ~1 m, investigations. Deeper investigations are possible only with radiography, however radiation protection must be implemented when using this technique. An overview of the key aspects of each of these techniques is presented below.

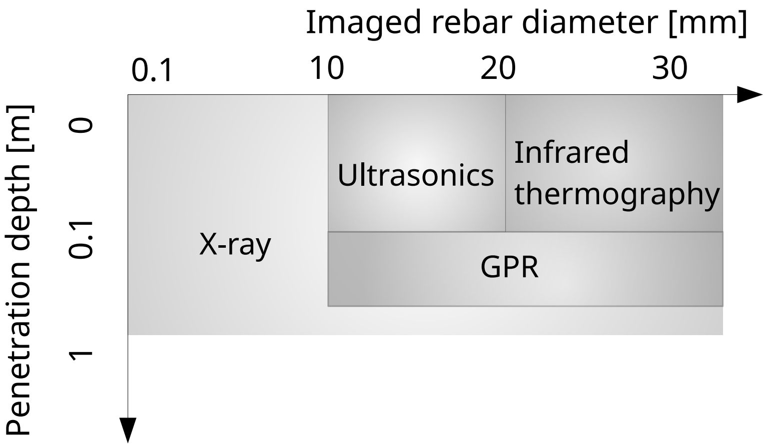

Figure 1: Rebar imaging capabilities of the most common techniques [13, 14, 15, 16, 17, 19, 20, 23].

2.1.1 Ground penetrating radar

Ground penetrating radar [13, 14, 15] is employed to monitor the structural health of concrete constructions such as buildings, bridges, and tunnels. In structural concrete, it can be used for the estimation of element thickness from one surface, delaminations, voids, cracks and their lengths, cavities, detecting steel reinforcement and its diameter, position of reinforcement elements, estimation of their depth or location of moisture variations and to produce contour maps of subsurface features [13, 16, 25, 26, 27].

Physics principle It is a method that is based on reflection of electromagnetic waves. Different frequency antennas are utilised depending on details and penetration depth.

Typical signal frequencies range from 500 MHz to 2.5 GHz for practical applications. The GPR system includes a transducer composed of transmitting and receiving antennas. To perform a test, grid lines are first marked on the building at various intervals (typically around 76 cm). After that, the GPR equipment is moved on these grid points to gather data across the surface. Electromagnetic pulses are sent inside the object and the time between emission and arrival of the reflections and the signal amplitude are recorded. Any impurities, such as rebar or any flaws, reflects some of the energy back to the surface. The remaining GPR energy penetrates further down and some is constantly reflected back to the receiver. GPR detects signal responses induced by variations in the electrical characteristics (electrical conductivity and relative dielectric permittivity (dielectric constant)) of the tested materials. The travel time of the reflected signal is dependent on the depth of layer boundaries and the velocity of the electromagnetic signal in given material. The velocity of the signal is inversely proportional to the square root of the relative dielectric permittivity of the material, ϵ_r. This is $\epsilon_{air} = 1$ for air and $\epsilon_{water} = 81$ for water. For concrete, values of permittivity vary between 5 and 12 which give velocities between 87 m/s and 134 m/s. These mostly dependent on the moisture level and frequency of the signal. Smaller velocity values refer to wet concrete. The signal amplitude is primarily affected by the effective electrical conductivity. Radar waves travel faster in dielectric than in conductive materials. This affects the depth of penetration. The best penetration is observed for dry concrete at low frequencies. However, the chance to detect small objects increases with higher frequency so the choice of antenna type and its frequency is a compromise between penetration depth and resolution [13, 25, 26]. Ground penetrating radar testing is shown in figure 2.

Limitations The application of GPR in reinforced concrete structures surveys is limited, since GPR depends on conductive properties of the material. Metal, closely spaced reinforcement or highly conducting materials cannot be penetrated. Thus, the method allows only for a shallow investigation with only one or two layers of reinforcement at penetration depths of up to 400 or 500 mm depending on moisture content and chosen frequency [13, 28]. This makes this method not suitable for high-depth inspections.

2.1.2 Active infrared thermography

Active infrared thermography is another method used for the detection and characterization of defects in reinforced concrete structures and it is suitable for testing the subsurface area up to 10 cm deep [29]. This type of inspection method can be used for detecting internal voids, delaminations or cracks in concrete buildings like bridge decks, highway pavement or building pavements etc. The benefit of using infrared thermography is that it is safe, efficient, time efficient, non-invasive, and non-contact [18, 25, 30].

Figure 2: Ground penetrating radar testing [26].

Physics principle Infrared thermography detects heat at any temperature and changes it into a thermal image [31]. The basic principle behind this method is recording infrared radiation (wavelengths range from 0.7 µm to 14 µm) emitted by a physical object and maps of surface temperature are generated.

There are two types of thermography: passive and active. Passive thermography does not interfere with the heat exchange processes inside and around the body while the infrared radiation emitted by the tested body is measured. In active thermography, the external thermal stimulation is used. It leads to propagation of the heat inside and on the surface of the tested object through the processes of the heat exchange like radiation and conduction.

Thermal conductivity (λ), specific heat capacity (C_p), and density (ρ) are the three basic parameters that govern heat movement and distribution inside a material [26]. Infrared thermography relies on the fact that anomalies in concrete disturb heat flow through the material and this causes local variations of the temperature on the surface. When the tested object is heated, it radiates some energy back. Void or delaminated regions are often filled with air or water. These materials have a different thermal conductivity and heat capacity than concrete around it. As a result, delaminated areas heat up and cool down faster than concrete and the difference in temperature can be between 1°C to 3°C compared to surroundings [25, 30]. Figure 3 shows an infrared image of a bridge span where a damp patch and a pipe were identified. These two areas are characterized by different temperatures.

Limitations The main drawback of this method is that not all of the anomalies lead to a sufficiently large temperature difference compared to bulk material. To get reliable results, the thermal stimulation must be as uniform as possible thus the testing is influenced by environmental conditions [17, 25]. What is more, the equipment is very expensive and since it takes an image of a surface, it cannot provide the depth of the defects. To record and analyse data appropriately, a qualified operator and analyst are necessary [25]. What is more, it is suitable for testing the subsurface area up to 10 cm deep [29].

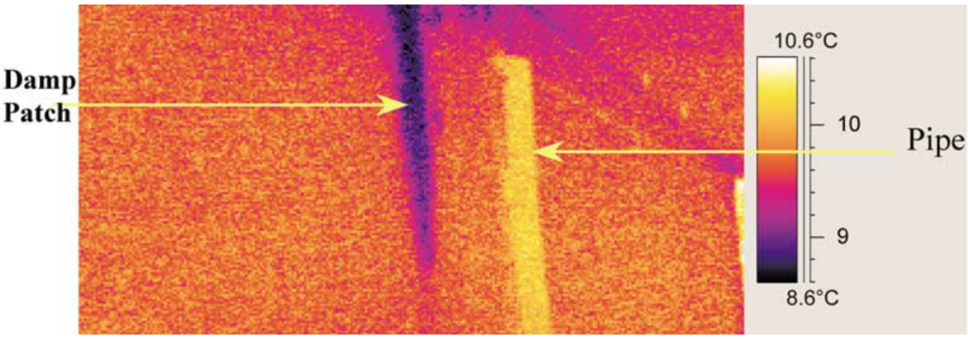

Figure 3: An infrared image of a bridge wall. A damp patch characterized by lower temperature and a pipe characterized by a higher temperature were identified [29].

2.1.3 Ultrasonics

Non-destructive testing using ultrasonic pulses is a well-established method for detecting interior objects in metals and other materials [32]. It can be utilised to identify abnormal areas in the concrete, the water-to-concrete ratio, hardening, strength, damage and inspecting reinforcement bars [21, 33].

Physics principle Ultrasonic echo pulses and ultrasonic pulse velocity techniques can be distinguished. These methods use the transmission and reflection of mechanical stress waves at sonic and ultrasonic frequencies through a tested object [31]. A transmitting and a receiving transducer comprise the ultrasonic device. The transmitting transducer generates a stress pulse (usually 50 kHz) that travels through the member and is recorded by a receiver, either on the opposite side or on the same side of the member. The characteristics of the examined object can be retrieved for example by measuring the Time-of-Flight (ToF), energy scattered back to the receiver or by analysing the attenuation of the wave [25]. The receiving transducer displays the data in the form of travel time. The sound propagates in the physical object thanks to the vibrations of atoms and molecules of that object. Defects are defined as any acoustical impedance anomaly that differs from the tested concrete object. Any flaws, inhomogeneities, interfaces or discontinuities in the material disturb the wave and lead to scattering, reflection, distortion or attenuation of the propagating sound wave. As compared to concrete in undamaged regions, concrete with substantial degradation or microcracking has a considerably lower velocity of the stress waves [25, 33].

Limitations The main drawback of that method is that it provides shallow imaging at the depth less than 20 cm [19, 20]. What is more ultrasonic pulse echo surveys are time-consuming because they need very narrow spacing between test spots to create pictures of the tested material. The data quality is heavily reliant on the sensor unit's coupling, which might be challenging on uneven surfaces [26]. The application to concrete runs into problems due to the inhomogeneous concrete structure. Since the acoustical characteristics of aggregate and pores differ significantly from those of the cement matrix, ultrasonic wave dispersion occur [21, 33, 34].

2.1.4 Radiography

Radiography is the most commonly used imaging technique. Radiographic systems are mainly used to locate voids, cracks, reinforcement. Radiography may identify any characteristic in a component or structure if there are enough differences in thickness or density inside the tested piece. Radiography's sensitivity varies depending on numerous factors, but in general, if a feature causes a 2% or higher change in absorption compared to the surrounding material, it will be detected [12, 24, 35].

Physics principle It uses electromagnetic radiation such as X-ray or gamma rays. X-ray systems require a linear accelerator to generate X-rays, while gamma rays are emitted from radioactive source. As X-rays are generated by linear accelerators, their energy may exceed those of gamma radiation, as can their capacity to penetrate materials [36]. The X-rays wave lengths range from 10^{-6} µm to 10^{-2} µm and gamma rays are characterized by wave lengths that smaller than 10^{-4} µm [11]. The rays travel through the tested object and are partially absorbed by the medium. The amount of absorption depends on the density, thickness of the material the radiation is passing through and also the characteristics of the radiation. The transmitted intensity, I, is defined as follows [11]:

$$I = I_0\, exp\left[-\int_0^t \mu(x,y,z)dt\right] \tag{1}$$

where, I_0 is incident intensity, $\mu(x,y,z)$ is the attenuation coefficient which depends on the sample density at (x, y, z) position, t is the thickness of the object. Attenuation coefficients differ between materials; for steel it is 1, for concrete 0.3 and for air 0. The radiation is detected and recorded behind the scanned object and a two dimensional projection of the attenuative properties of the object is created.

Limitations The major limitations of this method are its expense and the long scanning time. Additionally, operation with radioactive sources requires highly trained staff and radioactive shielding [11]. Another limitation is the penetration depth. For gammagraphy it is below 60 cm [9], for radiography, depends on the device between 10 cm and 60 cm [11, 12].

2.1.5 Remaining challenges

Many techniques for NDE exist. However, there are still remaining challenges which cannot be addressed with existing NDE methods. These include scanning of large-volume objects and objects with several layers of reinforcement. These challenges can be addressed using muon tomography. This is the main topic of this thesis.

3 Muon imaging methods

Muon tomography exploits ubiquitous secondary cosmic rays - muons. This radiation traverses objects and interacts with it. It results in changes in the rays direction and energy. Measuring the changes allows imaging of the traversed objects.

3.1 Relevant physics of muon imaging methods

3.1.1 Cosmic rays

Cosmic rays are high energy, charged particles which travel at a speed close to the speed of light. Their energies range from a few MeV to 10^8 TeV [37]. They were discovered in 1912 by Victor Hess in balloon experiments. For this discovery, he was awarded the Nobel Prize in Physics in 1936 [38]. He proved cosmic rays exist by comparing the presence of dark currents in ionisation chambers at sea level and at an altitude of 9 km.

Cosmic rays are divided into primary and secondary. The vast majority of primary cosmic rays are atomic nuclei: most, about 74% are hydrogen nuclei and 70% of remaining ones are helium nuclei [39]. Secondary cosmic rays are produced in interactions of the primary cosmic rays in the upper atmosphere. These collisions lead to air showers of secondary radiation. This produces muons, X-rays, protons, alpha particles, pions, electrons, neutrinos, and neutrons [40], see figure 4, where the altitude where Victor Hess carried out his experiment is indicated as well.

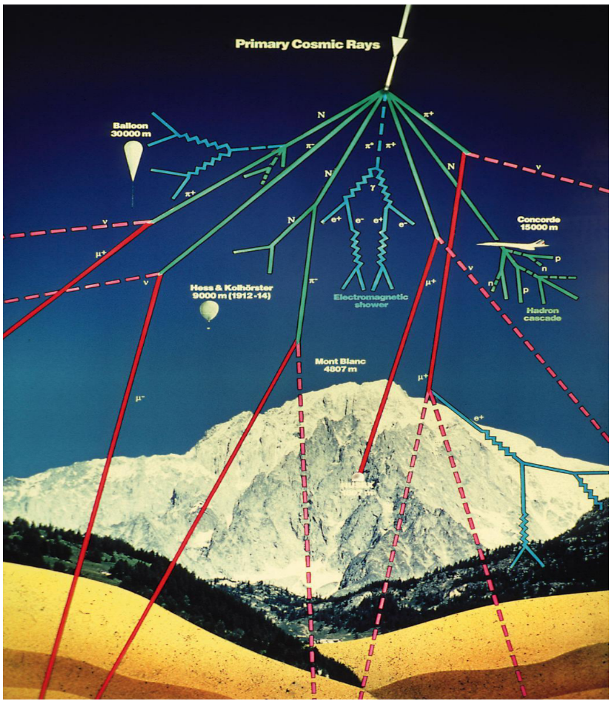

Figure 4: An example of a shower of secondary cosmic rays [41].

3.1.2 Muons

Classified as leptons, muons are elementary particles with a mass of 105.65 MeV/c^2, a mean lifetime of $2.2 \cdot 10^{-6}$ s [39], an electric charge of -1e and a spin of 1/2. Muons are 207 times heavier than electrons. They are unstable particles, but due to relativistic effects (time dilatation and length contraction) they can reach the Earth surface. Muons are the most abundant charged particles at sea level. The vast majority of them are created in the higher atmosphere, typically at an altitude of 15 km in the decay of pions and kaons in the reactions [39]:

$$\pi^- \rightarrow \mu^- + \bar{\nu_\mu} \qquad \pi^+ \rightarrow \mu^+ + \nu_\mu \tag{2}$$

$$K^- \rightarrow \mu^- + \bar{\nu_\mu} \qquad K^+ \rightarrow \mu^+ + \nu_\mu \tag{3}$$

Muons have a very wide energy and angular spread, see figure 5. At ground level, their mean energy is about 4 GeV which is sufficient to penetrate metres of rock. The integral intensity is about 70 m^{-2}s^{-1}sr^{-1} [42, 43] for vertical muons above 1 GeV/c at sea level [39].

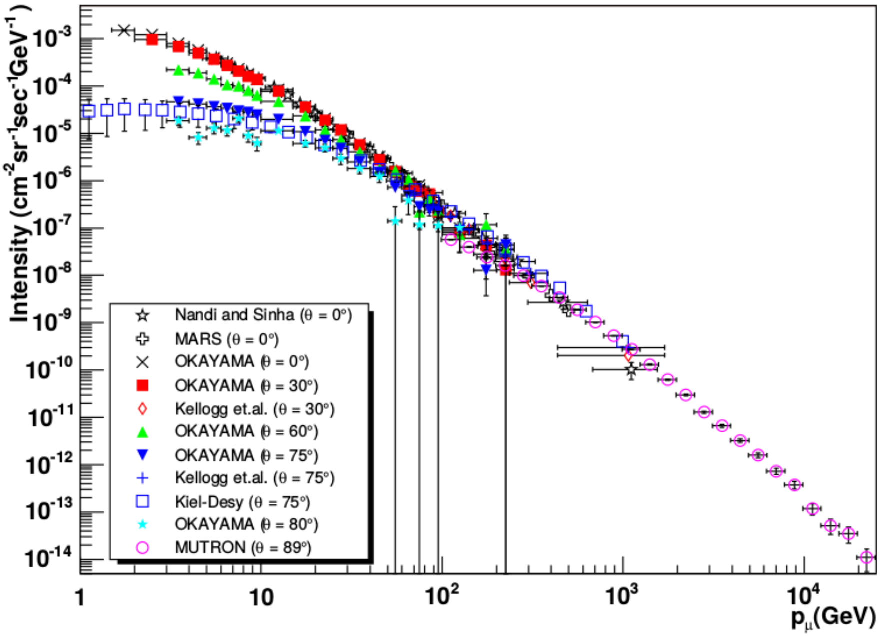

Figure 5: Muon intensity versus muon momentum for different zenith angles, θ [44].

3.1.3 Muon interactions with matter

When travelling through matter, muons undergo different processes; the most important is multiple scattering [39] in which momentum is transferred from the muons to the material through electromagnetic interactions. This results in energy loss and changes in direction. Measuring these allows to extract information on the traversed object. Here an overview of the key processes is presented.

3.1.4 Energy loss of muons

The average energy loss of high energy muons when traversing matter, dE, per unit of path, dx, also known as a stopping power, can be described as:

$$\langle -dE/dx \rangle = a(E) + b(E)E \tag{4}$$

where $a(E)$ represents the energy loss due to ionisation and atomic excitation processes, $b(E)$ describes the energy loss occurred through three radiation processes: bremsstrahlung, pair production and photonuclear interactions and E is the total kinetic energy. The individual contributions in $b(E)$ part can be seen in figure 6. The $b(E)E$ part is less than 1% of $a(E)$ for $E \lesssim$100 GeV for most materials. Since muons which reach Earth and used in this analysis have energy of about a few GeV, see figure 5, the $b(E)E$ part will not be discussed here.

For moderately relativistic, charged, heavy particles at intermediate energies, $a(E)$ part is represented by the Bethe formula:

$$\left\langle -\frac{dE}{dx} \right\rangle = Kz^2 \frac{Z}{A} \frac{1}{\beta^2} \left[\frac{1}{2} \ln(\frac{2m_e c^2 \beta^2 \gamma^2 W_{max}}{I^2}) - \beta^2 - \frac{\delta(\beta\gamma)}{2} \right] \tag{5}$$

where K is a combination of constants ($K = 4\pi N_A r_e^2 m_e c^2 / A$), N_A is the Avogadro number, r_e the classical radius of the electron, m_e the mass at rest of the electron, c the speed of light in vacuum, A the atomic mass of the matter the muon travels through, z the electric charge of the particle, Z the atomic number, β the speed of the particle normalized to the speed of light in the vacuum, γ the Lorentz factor, W_{max} the maximal kinetic energy transferable in a single collision, I the ionisation potential in eV and δ is the density-effect correction.

The total energy loss of positive muons in copper combining all process over a large energy range is shown in figure 7. Formula 5 is valid in the region $0.1 \lesssim \beta\gamma \lesssim 1000$ with an accuracy of a few percent and it is marked in figure 7 as "Bethe". Up to an incident energy of 10 GeV, ionisation is the main cause of energy loss. Above 100 GeV, the energy loss is mainly due to radiation processes. Moreover, energy loss due to ionisation does not change much over a big range of the muon incident energy. Since most of muons have energy between 1 and 100 GeV, the stopping power is relatively low, e.g. the energy loss for cosmic muons when passing through standard rock is 1.688 MeV cm^2/g [45]. Thus, cosmic muons are characterized by high penetration properties.

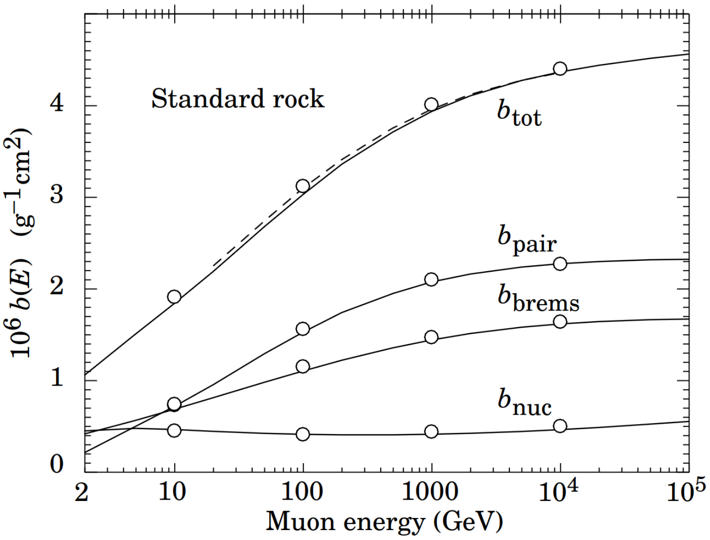

Figure 6: Contributions to the energy loss of muons in standard rock due to bremsstrahlung, production of pairs and photonuclear interactions [39].

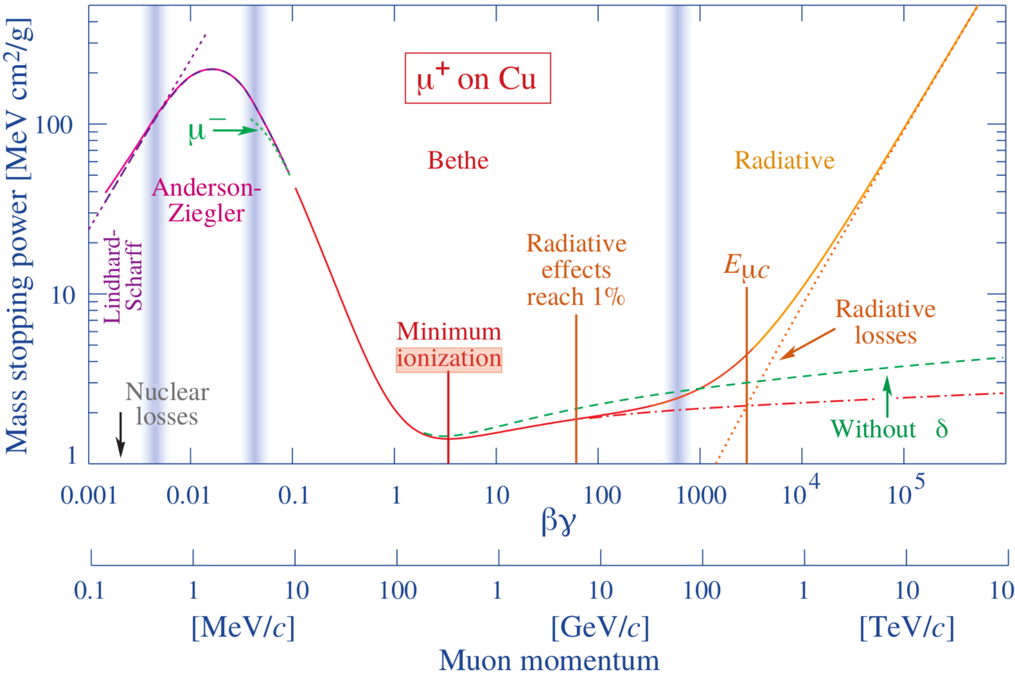

Figure 7: Energy loss for positive muons in copper as a function of $\beta\gamma$. Solid curves indicate the total stopping power where the vertical lines show boundaries between different approximations used [39].

3.1.5 Multiple scattering

Coulomb interactions of the nuclei and the electric fields of the electron clouds cause many small-angle deflections for the charged particle when it travels through matter. As a result, a number of small, random changes in direction occur and the particle leaves the matter at an angle with respect to the incoming direction, see figure 8. This is knows as multiple scattering. The scattering angle is not fixed but follows a well-known spectrum which depends on the material type, its thickness and the particle momentum and thus can be used for material differentiation. For many applications, it is adequate to use a Gaussian approximation for the angular distribution with a mean of 0 and a standard deviation given by [39]:

$$\sigma_\theta = \frac{13.6\text{MeV}}{\beta c p} z \sqrt{\frac{x}{X_0}} \left[1 + 0.038 \ln\left(\frac{x}{X_0}\right)\right] \tag{6}$$

where p is particle's momentum, β its speed divided by the speed of light c, z charge number of the incident particle, x is the thickness of the material and X_0 the radiation length of the traversed material. The radiation length is a material constant, described by the distance after which an electron's energy has dropped to 1/e of its starting number. The radiation length is the characteristic range for scattering and other electromagnetic interactions. It decreases with increasing Z number of material. The standard deviation of the angular distribution depends, through the radiation length, on the atomic number, Z, of the traversed material, thus, the scattering angle distribution is characteristic for every traversed medium. The radiation length is approximated as follows:

$$X_0 = \frac{716.4A}{\rho Z(Z+1)\ln\left(\frac{287}{\sqrt{Z}}\right)}[\text{cm}] \tag{7}$$

where, ρ is material density. The radiation length can be also defined in units of g cm^{-2}.

In muon scattering tomography, the muon scattering angle is measured. Since the scattering angle depends on the radiation length, the radiation length becomes a main property of the material that muon scattering tomography is responsive to. The radiation length for relevant elements are given in table 1 and relevant materials are given in table 2.

element	Z	X_0 [g cm^{-2}]	X_0 [cm]
iron	26	13.84	1.757
uranium	92	6.00	0.3166

Table 1: Radiation lengths for relevant elements [46].

material	Z/A [mol g^{-1}]	X_0 [g cm^{-2}]	X_0 [cm]
air	0.49919	36.62	30390
concrete	0.50274	26.57	11.55
glass	0.49731	25.66	10.69
soft tissue	0.55121	37.63	37.63
bone	0.52740	32.11	22.15

Table 2: Radiation lengths for relevant materials [46]. Soft tissue and bone are relevant for results in chapter 9.

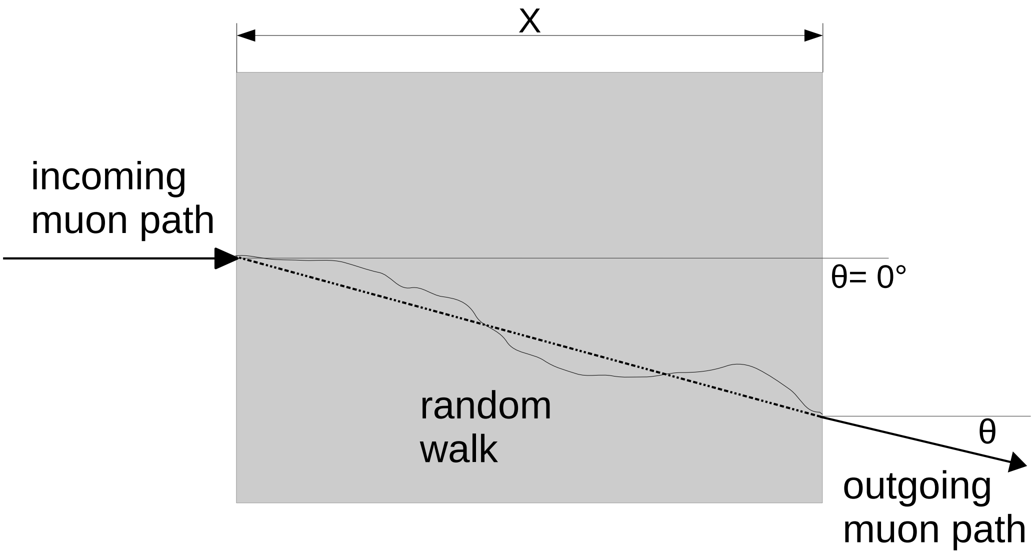

Figure 8: Illustration of multiple Coulomb scattering in the context of muon scattering tomography.

3.2 Muon techniques

Muons make excellent probes to images the insides of (large) objects, because they mainly interact through electromagnetic interactions in which they only lose a small fraction of their energy resulting in very large penetration depths. This overcomes some limitations of the existing techniques because of little attenuation. In contrasts to methods described chapter 2.1 muon techniques are able to scan a few layers of reinforcement or kilometres of rocks with no use of artificial radiation. Muon radiography and muon scattering tomography are briefly described below.

3.3 Muon radiography

When muons scatter, they lose energy. If their energy becomes too low, they stop. This leads to a reduction in the muon flux. The path length depends on the muon energy, the amount and type of material they traverse, see equation 7. Measuring the flux reduction and the outer dimensions allow to determine the density along that particular line of sight. The most straightforward way of measuring the reduction in flux is by comparing with the flux along the opposite line of sight, i.e. muons coming in from the opposite direction and not traversing the object under study. Repeating this from two different orientations allows to extract a 3D density map of the object under study. The image obtained is not as detailed as with tomography but has the main advantage that only one detector system is needed, which can image a large object. It is a very appropriate technique to image vast structures and thus it is used to inspect pyramids [47, 48], volcanoes [49, 50, 51, 52, 53] or subsurface inspection [54, 55, 56].

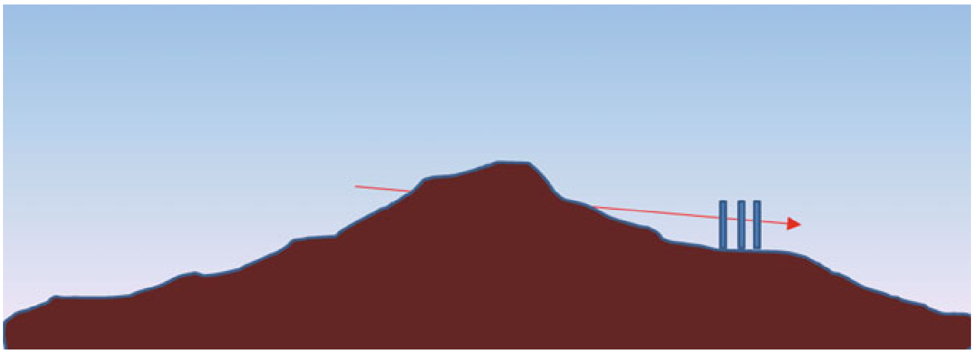

Figure 9: Schematic sketch of a muon radiography approach for a volcano's summit. A muon tracking detector measures muon flux as a function of arrival direction. This provides data of a region that muons passed through. Data are collected at various directions [57].

3.4 Muon scattering tomography

Tomography is an imaging method of an object using any form of penetrating probe. Muon scattering tomography uses multiple Coulomb scattering of cosmic muons as information source, see section 3.1.5, and extracts information about the object by reconstructing incoming and outgoing muon tracks. MST is used for imaging dense and large objects, where other methods do not provide satisfactory results, see chapter 2.1. The main benefit is that the scanning process is safe and non-invasive, both for scan operators and the scanned objects. Moreover, cosmic muons are ubiquitous probes, thus no additional source of artificial and harmful radiation is needed for system operation. The imaging can be done using sandwiched detector placed above or below, or at angles to the tested volume, see figure 10.

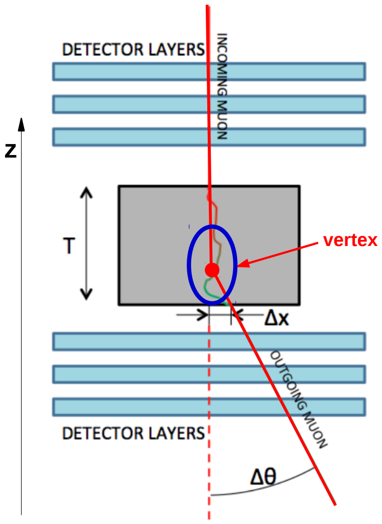

Figure 10: Muon scattering tomography principle [58].

3.4.1 Determine the muon path in matter

Muon scattering tomography relies on measuring the incoming and outgoing muon hits and then reconstructing likely paths for that muon. Various imaging methods based on exploiting information about the incoming and outgoing muon tracks exist [59, 60, 61]. A commonly used concept is the scattering angle of the muon. This is a very useful but nonphysical concept. If one assumes that the change of direction occurs at a single point, a vertex, a scattering angle can be defined. This scattering angle will then yield key information about the traversed matter. The assumption works well for high-Z materials where there are many muons displaying large changes in direction. It can be also employed for low-Z materials but the scattering angles are smaller there.

3.4.2 PoCA

One of the most common and simple algorithm is a three-dimensional object reconstruction method called PoCA - it is based on the point of closest approach of the incoming and outgoing muon tracks [62]. It is illustrated in figure 11. The two-dimensional sketch is used to simplify the introduction, however the method is three-dimensional. In this approach the object is treated as a set of 3D voxels. The incoming and outgoing muon paths are treated as straight lines and extrapolated to the edges of the object. Inside the medium, muons undergo multiple Coulomb scattering and perform a random walk. The muon scattering angle is of order milliradians, thus it can be approximated as a straight line which spans from muon entry to muon exit point. Next, all of the voxels along the line in the medium are identified. Then, the scattering angles in X and Y planes are calculated assuming that the scattering occurs in a single place and by extrapolating the incident and scattered muon path to find their point of closest approach. Then, the estimated scattering strength signal, S_{PoCA}, is calculated [62]:

$$S_{PoCA} = \frac{\Delta\theta_x^2 + \Delta\theta_y^2}{2L(1 + E_p^2)} \cdot \left(\frac{\hat{p}}{p_0}\right)^2 \tag{8}$$

where $\Delta\theta_x^2$ is the scattering angle in X, L is the voxel size in radiation length, $\hat{p}$ estimate of the particle momentum, p_0 is a reference momentum, for example 3 or 4 GeV, E_p is relative uncertainty of the momentum.

The S_{PoCA} is assigned to the voxel which contains the point of closest approach and 0 is assigned to all other traversed voxels. Next, the mean of the signal is calculated for each voxel, including the values of S_{PoCA}=0 and thus a 3D image with the estimated scattering strength in each voxel is created.

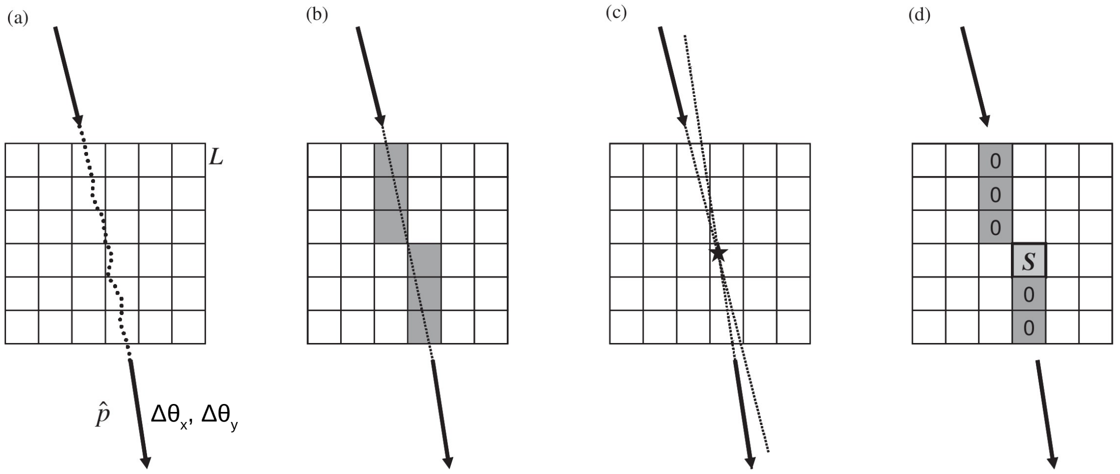

Figure 11: PoCA imaging reconstruction algorithm, shown in 2D for clarity [62].

The PoCA algorithm works but suffers from several issues. For example, one value per voxel is calculated and these voxels need to be reasonably large such that enough statistics is collected for that voxel. In addition, the reconstructed point of closest approach should be in a voxel where the muon actually went. These two considerations lead to large voxels where maybe a material interface is located or the signal from a rebar can be smeared out with the concrete signal in the rest of the voxel. Furthermore, because all traversed voxels besides the one with the point of closest approach will receive a value of 0, there is a tendency to end up with low scores for voxels containing medium-Z material that are in the neighbourhood of high-Z materials. As such, material identification with PoCA is complicated [61].

3.4.3 Bristol discriminator algorithm

To improve on PoCA, a group from the University of Bristol created a discriminator algorithm called the metric method [63]. It has been employed to check cargo containers in search of lumps of special nuclear materials [63, 64], to image nuclear waste [7, 58], to discriminate high-Z materials in concrete-filled containers [65] and to detect the presence and location of gas bubbles [66]. It is a decision-making algorithm which, in contrast to PoCA, takes advantage of the spatial clustering of muon scatter vertexes in the tested medium. In higher-Z materials, vertices for large angle scattering will be spatially closer together than in lower-Z materials. The whole process starts with reconstructing the muon paths before and after leaving the scanned medium and determining a scatter location, the vertex, and the scattering angle, see figure 10. The tested volume is treated as a set of 3D sub-volumes called voxels. In the research presented here voxels were $10 \times 10 \times 10$ mm^3. One advantage that this method has is that the voxel grid can be easily moved without recalculating everything. Voxels must be big enough to cover a tested sample and small enough to provide desired resolution. Based on the vertex locations, tracks are assigned to voxels, thus, in every voxel there is a number of reconstructed vertices. Next, for every voxel, the algorithm computes a weighted 'clusteredness' value, a weighted metric distance $\widetilde{m_{ij}}$ between each pair of vertices for the N most scattered tracks in that voxel, which is defined as:

$$\widetilde{m_{ij}} = \frac{\|\boldsymbol{V_i} - \boldsymbol{V_j}\|}{\theta_i \cdot \theta_j} \tag{9}$$

where $\boldsymbol{V_i}$ is the location of muon i vertex and θ_i is the scattering angle. The distribution of ln(weighted metric) was calculated for every voxel. In figure 12 an example of the distribution of the ln(weighted metric) for single voxels is shown, were $10 \times 10 \times 10$ cm^3 U and Pb lumps were studied together with an air scenario. One can see that the distributions are different depending on the analysed scenario which means that weighted metric value indicates the material in the voxel. Finally, the algorithm returns the median of the ln(weighted metric) distribution for a given voxel. This variable is the final discriminator. The returned discriminator value depends on two factors; the type of material in the sub-volume, and the number of muon tracks used. Most muons do not scatter at all and go straight through. To boost the sensitivity to heavily scattered muons, in every voxel, muons are sorted by the scattering angle and the N most scattered tracks are used, where N must be the same for every voxel in given analysis. If a voxel has not got the required N vertices it is disqualified from further analysis. When the same number of muons is used for every voxel, the median depends on the sub-volume content only.
Discriminator values gathered from every sub-volume are used to prepare a discriminator distribution which is the basis for further analysis. An example is shown in figure 13. Data were taken from a simulation of a solid concrete-filled object, a solid concrete-filled object with a rebar inside and a solid concrete-filled object with a gas void. It can be clearly seen that the inclusion of the iron rebar (which is a higher-Z material) gives lower discriminator values. Adding lower-Z components (like gas) returns greater discriminator values.

The approach described above was a starting point of the research presented here and developed for new challenges as shown throughout the thesis.

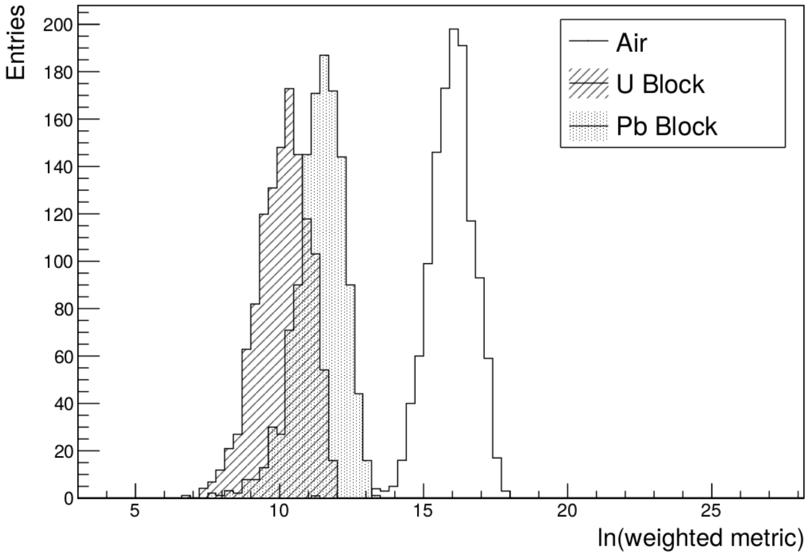

Figure 12: An example of the distribution of the ln(weighted metric) for single voxels containing different materials [63].

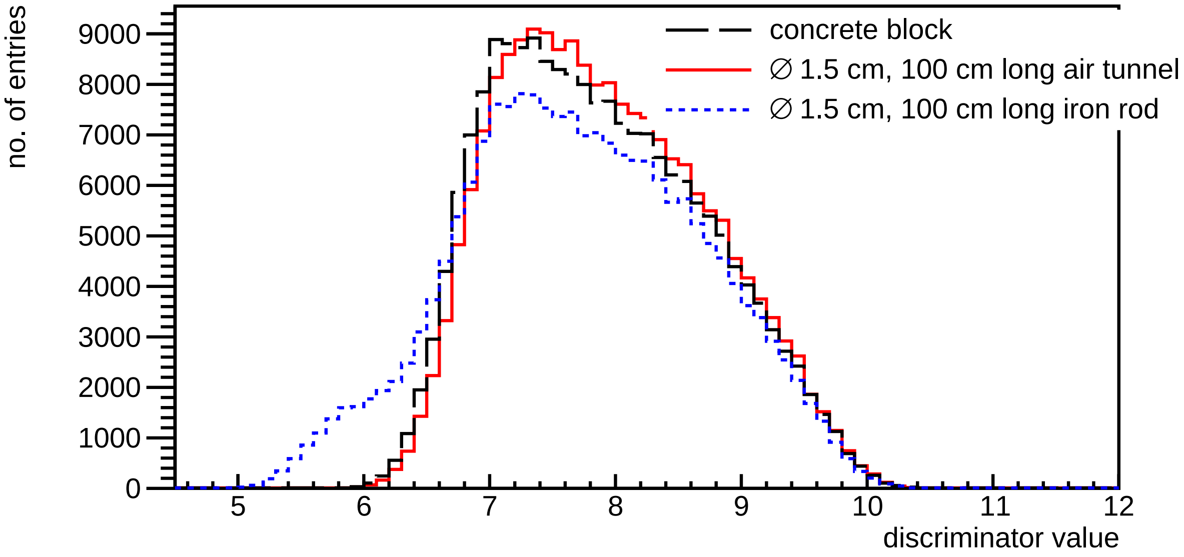

Figure 13: The discriminator distribution for a concrete-filled object, a concrete-filled object with rebar inside and concrete-filled object with gas void inside.

3.5 Limitations of muon methods

The main limitations of muon tomography are due to the flux and direction of the muons. The flux is limited and thus data taking cannot be sped up. Most muons come from vertical, fewer are present on the sides. Hence detector positions must be adjusted to this, which is sometimes difficult to do. Muons are therefore useful in cases where time is not an issue, for example when scanning geological objects or concrete objects where detectors can be left for a longer time.

4 Monte Carlo simulations of the detector prototype

The development of muon tomography algorithms relies to a large extent on detailed simulations. This is mainly because the muon rate is limited and most reconstruction algorithms are based on statistical methods that require large data samples to tune the algorithms. There are several Monte Carlo codes developed for tracking charged particles through materials [67, 68, 69, 70] and several libraries that provide muon spectra [71, 72, 73, 74]. In this thesis Geant4 [67] is used to track the muons while CRY [75] is used to generate the muons. In this chapter the concepts and infrastructure for the simulations are presented.

4.1 Geant4

The Geant4 environment is a toolkit that performs Monte Carlo simulations of particles traversing matter and is widely used in applied physics, high energy physics, space and radiation science and medical physics. Using Geant4, any radiation source, detectors and setup can be simulated. Interactions of particles with the material of the setup can be tracked. As an output, physical quantities of the outgoing particles can be recorded and analysed. The Geant4 contains a total collection of physics processes for electromagnetic, strong and weak interactions of particles in matter over a huge energy range between meV up to 100 TeV.

The setup can be simulated in great detail down to the constituent elements. The composition of the concrete, air and glass used in analysis is shown in table 3. Reinforcement was simulated as an iron object with density of 7.874 g/cm^3.

4.1.1 A database of cosmic ray data - CRY

As an input to the simulation studies, muons were generated using the CRY software. The CRY software is a database of cosmic-ray particle shower distributions. CRY database is created based on precomputed data from MCNPX simulations [68] of primary cosmic rays on and corrected against published cosmic-ray measurements. Primary particles can be generated for energies ranging from 1 GeV to 100 TeV while and secondary particles for energies between 1 MeV and 100 TeV. One of three altitude can be used (sea level = 0 m, 2100 m, and 11300 m). Generated particles are fired from a square plane surface of $n \times n$ metres, where n can be 1, 3, 10, 30, 100, and 300 m. In study presented here an altitude and latitude of 0 m and 51.46° respectively was used, where 51.46° corresponds to location of Bristol. The plane surface was 1 × 1 m^2 for 1 × 1 m^2 detectors or 3 × 3 m^2 for 2 × 2 m^2 detectors.

Air, ρ_{air}=0.0012 g/cm^3	
element	% composition
Carbon	0.01
Nitrogen	75.53
Oxygen	23.18
Argon	1.28

(a) Air composition.

Glass, ρ_{glass}=2.4 g/cm^3	
element	% composition
Oxygen	45.98
Sodium	9.64
Silicon	33.66
Calcium	10.72

(b) Glass composition.

Concrete, ρ_{concr}=2.3 g/cm^3	
element	% composition
Hydrogen	1.00
Carbon	0.10
Oxygen	52.91
Sodium	1.60
Magnesium	0.20
Aluminium	3.39
Silicon	33.70
Potassium	1.30
Calcium	4.40
Iron	1.40

(c) Concrete composition.

Table 3: Composition of materials used in simulations.

4.2 Detector setup

A brief description of the detector setup used in the work is given here. The performance of the simulated detector was based on the detection system detailed in chapter 8.

In muon scattering tomography incoming and outgoing muon paths need to be reconstructed using detectors placed on either side of the scanned item, see figure 14, where a sketch of the laboratory setup is shown. Six pairs, unless otherwise stated, of resistive plate chambers (RPCs) were used in this study. Three of them were placed above and thee below the scanned sample. In the simulation studies, realistic parameters of the RPCs' performance were used based on RPCs container scanner prototype that was built in Bristol [3, 76]. The RPCs had a position resolution of approximately 450 µm. For the simulation the exact design was included in the Geant4 geometry.

For the study presented here, the RPC planes were chosen to be 1 × 1 m^2 or 2 × 2 m^2. The efficiency of the detectors was set to 100%.

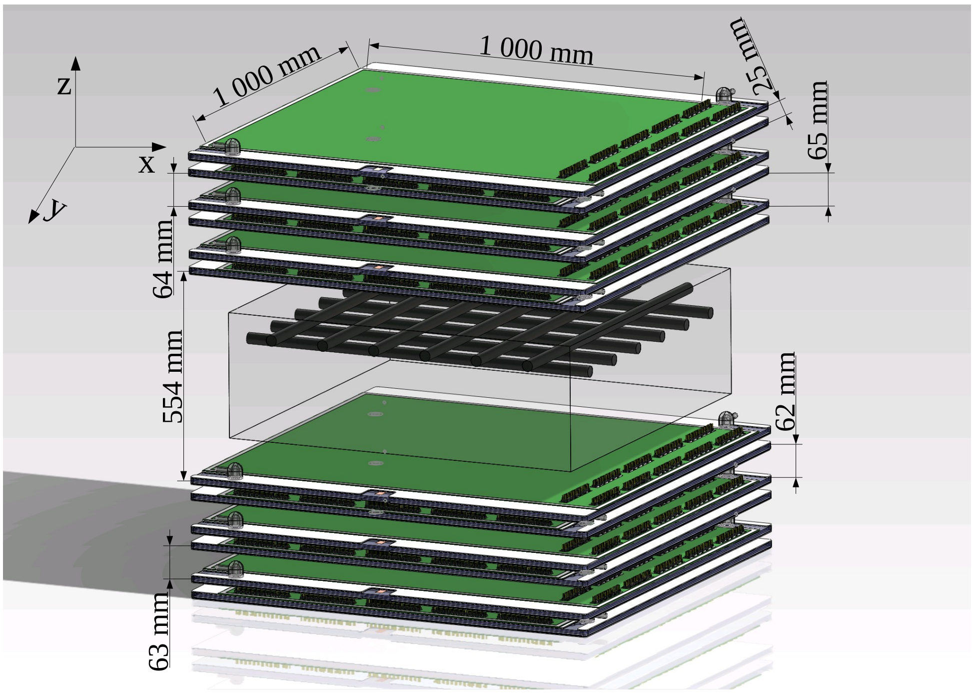

Figure 14: Schematic drawing of the detector setup used in the laboratory [77].

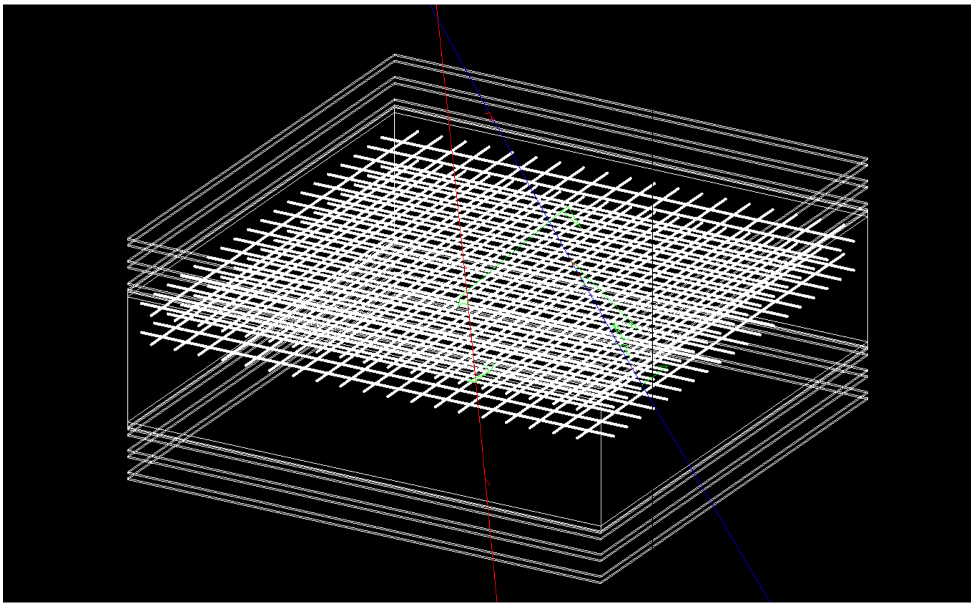

Figure 15: A simulation with a concrete block and two layers of iron rebar grid. The lines visible in the picture show muons passing through the detectors and the scanned object.

5 Muon Scattering Tomography as a tool for detection and imaging of rebars

Muon scattering tomography can be successfully employed as an NDE method in civil engineering to detect the presence of reinforcement in big concrete structures including measuring the size, spacing and location of single rods. Distinguishing between a single and a double layer of the reinforcement grid is also possible. The concept used for the inspection of reinforcement in concrete is based on the approach described in chapter 3.4.3 and is further developed to adapt it for this application using Monte Carlo simulations.

In this chapter, it is demonstrated that a rebar embedded in concrete can be detected with MST. Next the limits in terms of minimum detectable inclusion volume are established. Next, it is shown that it is possible to distinguish two rods as two separates objects when they are more than 4 cm apart. Finally, the imaging of a reinforcement grid is performed.

5.1 Study of reinforced concrete

As muon tomography is sensitive to differences in radiation length and thus density, so it should be able to detect the presence of rebars in large concrete slabs like floors. To test this, different scenarios were simulated to develop a method for rebar detection in concrete using MST. Rebars were modelled as cylindrical iron rods with diameters up to 150 mm. Three cases were considered: rebar inside variable size concrete block, rebar inside a fixed size concrete block and a real-sized reinforcement in concrete. Each time 216 million muons were simulated which corresponds to about three weeks of data taking at sea level. The CRY plane surface was 1 × 1 m^2 and 1 × 1 m^2 detectors were used.

5.1.1 Case 1: Rebar inside a variable size concrete block

A single 35 cm long rebar was placed in the centre of a concrete block. The size of the concrete block was increasing with increasing diameter of the rebar so that there was always a 10 cm thick concrete layer above and below the rod. The length of the concrete sample was set to 40 cm. The smallest simulated concrete block, without any rebar inside was 20 cm × 20 cm × 40 cm. For every rebar diameter a corresponding concrete background sample with the same dimensions was simulated. In figure 16 a sketch of this case is shown.

5.1.2 Case 2: Rebar inside fixed size concrete block

A single, 50 cm rebar was placed in a concrete block of a fixed size of 100 cm × 100 cm × 50 cm. The diameter of the rebar was varied in this study. A corresponding concrete only background sample with the same dimensions was simulated as well. The sketch of this scenario is shown in figure 17.

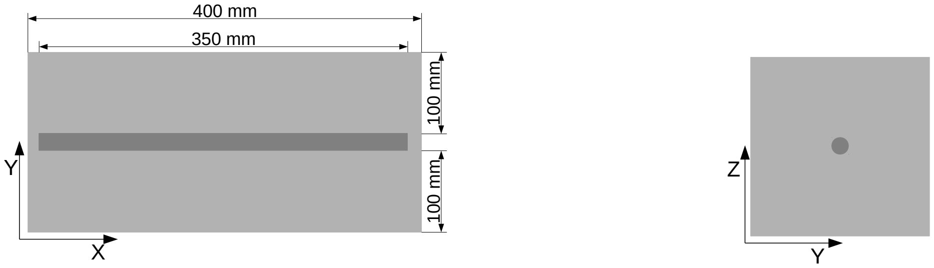

(a) Top (YX) view **(b)** Side (ZY) view

Figure 16: Sketch of the geometry with a rebar inside a variable size concrete cuboid. Front (ZX) view is identical as YX view [78].

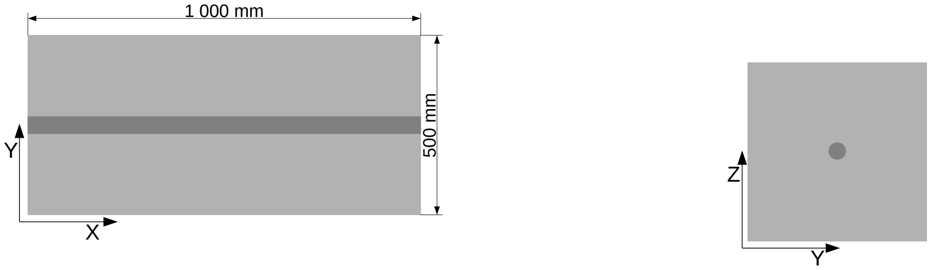

(a) Top (YX) view **(b)** Side (ZY) view

Figure 17: Sketch of the geometry with the rebar inside a fixed size concrete cuboid. Front (ZX) view is identical as YX view [78].

5.1.3 Case 3: Reinforcement in concrete

This scenario is to reflect the actual reinforcement grids used in civil engineering. It was divided into 4 sub-scenarios, where the concrete block always measured 100 cm × 100 cm × 34 cm.

1. A solid concrete block was generated as a background sample.
2. A single layer of rebars with diameters of 30 mm and length of 100 cm was placed in that block such that a 5 cm thick concrete layer covered the bars, see figure 18. The spacing between the rods was 15 cm.
3. Two layers of the same parallel rods, perpendicular to each other creating a grid were simulated, see figure 19.
4. Two grids were placed in the concrete block and the distance between them was 15 cm from centre to centre. Figure 20 shows details of this scenario.

5.2 Signal extraction

Every scenario described in section 5.1 has been simulated and for each one the discriminator distribution, as described in section 3.4.3, has been prepared. As shown in figure 13, discriminator distributions for different materials simulated look different. Using differences

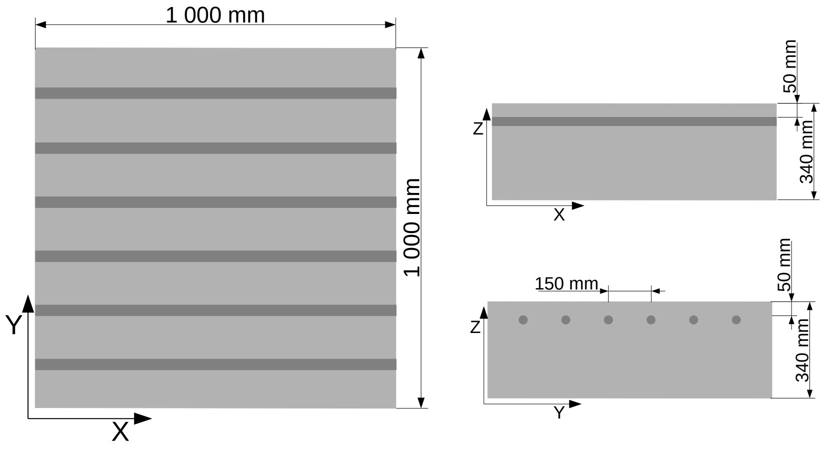

Figure 18: A single layer of rods in a concrete block [78].

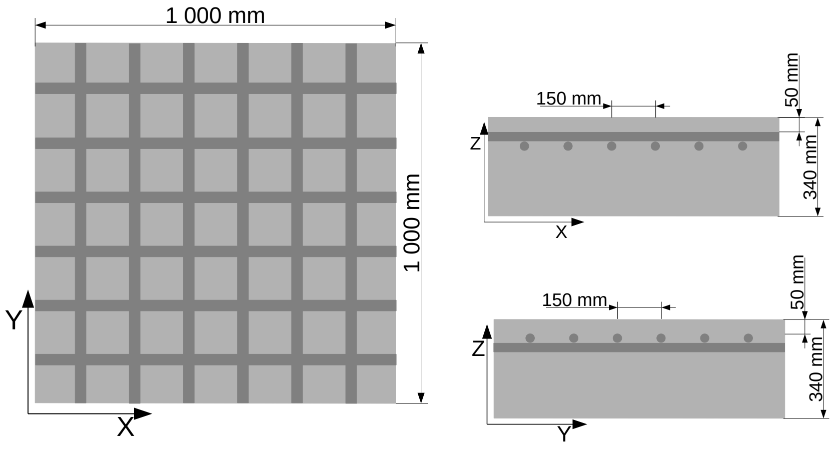

Figure 19: A single layer of a grid in a concrete block [78].

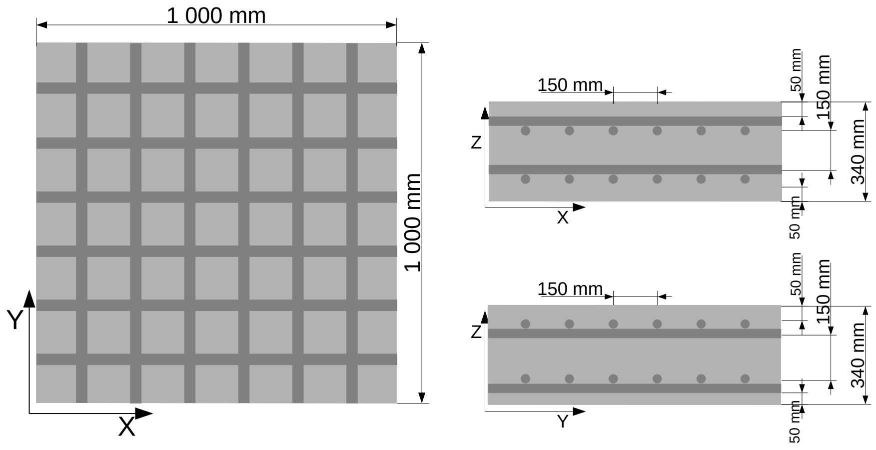

Figure 20: A two grid layer scenario in a concrete block [78].

between the discriminator distributions of a scenario with a rod and a concrete only scenario, the rod signal can be quantified. To evaluate the presence of a rebar, the signal (S) has been defined as the sum of the absolute differences between bins in the discriminator distribution for a case with a rebar (H_{rebar}) in the concrete and a concrete only case (H_{concrete}), where both samples had the same dimensions and were simulated for the same time. Signals for concrete only scenarios were calculated based on two concrete-only samples with the same dimensions.

$$S = \sum_{bin} |H_{\text{rebar}}(i) - H_{\text{concrete}}(i)| \tag{10}$$

5.2.1 Signal in a variable-sized concrete block

Blocks of concrete with different diameter rebars were simulated and their signals calculated. The signal as a function of the total rebar volume is shown in figure 21. The signal shows a monotonic dependence on the rebar volume. This proves that this approach is appropriate to reconstruct the total volume of rebars. Since the bin to bin values of H are influenced by statistical fluctuations, the signal is never zero even for the non-rod scenarios. When the total volume of the concrete sample increases, the background signal grows as well. The signal of the background grows because for larger concrete blocks, more voxels with concrete reach the threshold of the minimum number of vertices to be included in the discriminator distribution, see chapter 3.4.3. For each populated bin in the distribution, H, a positive addition to the signal is made, see equation 10. Therefore, the signal increases with the size of the concrete block, both for signal and background. Hence, in the non-fixed size concrete block case, the signal depends on both the iron volume and concrete volume. Although, with a separate method of assessing the volume of the concrete structure, the only unknown will be the rod volume.

5.2.2 Signal in a fixed-sized concrete block

The same study was repeated for a fixed size concrete block. Figure 22 shows the dependence of the signal as a function of rebar volume in the fixed size concrete block. Also here the signal increases monotonically with increasing rebar volume. Next, the minimum detectable diameter for 100 cm long rod was determined. To determine the detection threshold, the background scenario (concrete only block) was simulated 14 times, and the signal was extracted for every pair of concrete samples, where one concrete sample was treated as a signal sample and the other as a background sample. This results in different values of the background and a histogram of the obtained results was prepared. A Gaussian fit to the data yielded a mean, μ_b, and sigma, σ_b, of 3 994 ± 44 and 371 ± 34, respectively. The minimum detectable threshold S_{th} was set at $\mu_b + 3\sigma_b$ which is 5 107. This corresponds to a volume of 894 ± 386 cm^3 of iron which is a 100 cm long rebar with

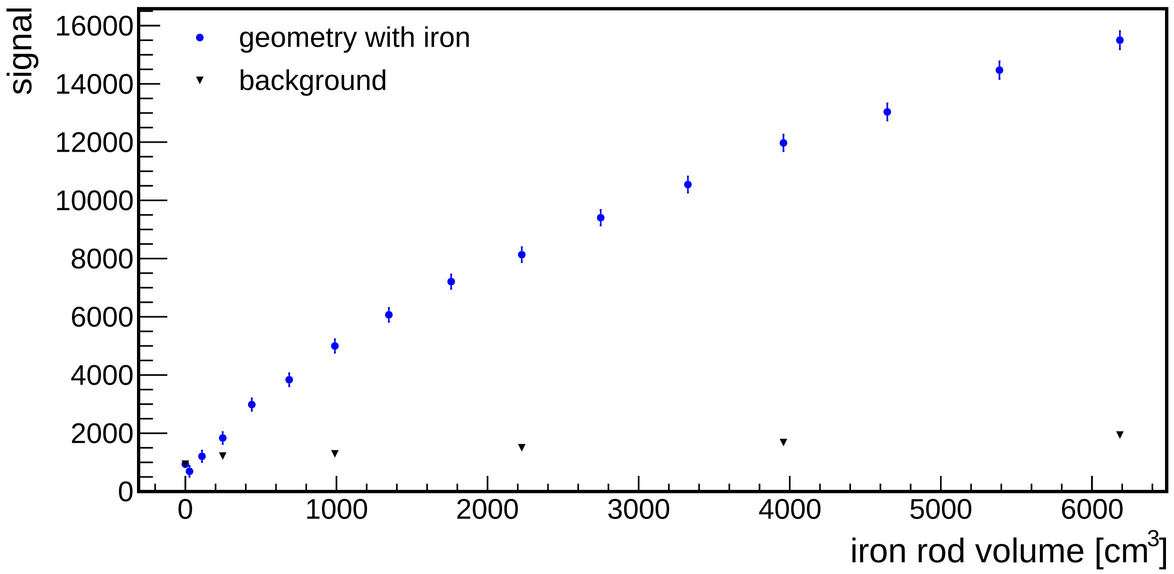

Figure 21: Signal as a function of the rebar volume for a variable size concrete block [78]. Geometry details in section 5.1.1.

a diameter of 33.7 ± 7.3 mm. The S_{th} is indicated in figure 22 as the red line.

5.2.3 Reconstruction of the rebar volume in the concrete object

As was shown, by extracting the signal, the volume of the rebar can be estimated. To reconstruct the rebar volume, the data above the detection threshold shown in figure 22 were fitted with a straight line. The χ^2/ndf was 13.37/10, proving that the linear model represents data well. The fit slope and the offset were 1.75 ± 0.03 and 4 997.3 ± 333.0, respectively. Next, the iron rod volume was reconstructed using the fit result for all simulated iron scenarios above the detection threshold. To keep the method unbiased, the straight line was fitted to all data points omitting the volume being reconstructed. Using the slope, the offset and the signal value, the volume was reconstructed. Figure 23 shows the reconstructed volume as a function of the simulated volume. There is a clear linear correlation between the reconstructed volume and the real volume. A straight line was fitted yielding a slope of 0.997 ± 0.023 and an offset of 25.9 ± 213.2. The χ^2/ndf was 16.74/10. The relative uncertainty of reconstructed volume as a function of simulated reinforcement volume is shown in figure 24. The relative uncertainty is better than 10% for volumes above 2 500 cm^3. This corresponds to a diameter of 56.4 mm for 100 cm long iron bars. For the volumes above 2 500 cm^3, a distribution of relative uncertainty was prepared and sigma of the fit yielded a resolution of 5.4 ± 0.3%.

5.2.4 Imaging of a single rod

As shown before, using muon scattering tomography it is possible to inspect the interior of a scanned sample. The next step is to image the sample. The imaging process allows

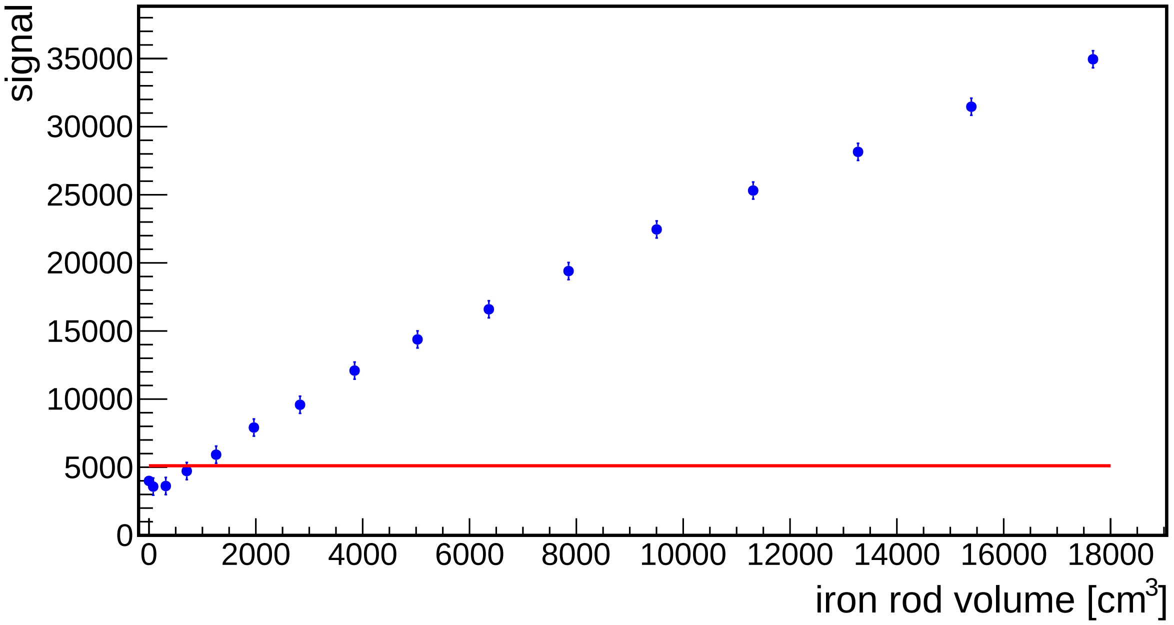

Figure 22: Signal for a rebar in a fixed size concrete block as a function of the rebar volume. The signal shows a monotonic dependence on the rebar volume for a fixed size concrete block scenario [78]. The threshold to detect rebars is shown as the red line. Geometry details in section 5.1.2.

to tell where and what shape the inclusion is and to tell if the inclusion consist of one or more objects.

To image the inside of the sample, the signal algorithm, see section 5.2, is applied to small sub-volumes of the sample. The imaging process is used on three projections separately: ZY (side view), YX (top view), ZX (front view). The imaging is done in following steps, here an example based on ZY projection is given:

1. For a given period of time, the sample with inclusion is simulated. The discriminator value is determined for a set of small voxels measuring 10 mm × 10 mm × 10 mm. Following that, a concrete sample with the same dimensions is simulated using the same amount of measurement time and the same voxel size.

2. For both samples, a 3D sub-volume, using a sliding window, is defined. In the ZY projection, a 5 cm × 5 cm window was used combining all discriminator values along the X direction into a single discriminator distribution. The definition of the sliding window is illustrated in figure 25.

3. The signal for a sub-volume is calculated based on discriminator distributions for sub-volumes for both background and geometry with inclusion.

4. Next, the sliding window is shifted by one voxel in the Y direction (see figure 25d). The sub-volume is redefined, new discriminator distributions prepared and signal for

new sub volume calculated.

5. The sliding window is moved until the entire item has been scanned and the signal for each sub-volume has been calculated.
6. A two-dimensional histogram of the signal (also called images or signal strength histograms throughout the thesis) for all sub-volumes is produced.
7. The procedure is repeated for the remaining projections to obtain a detailed information about the object.

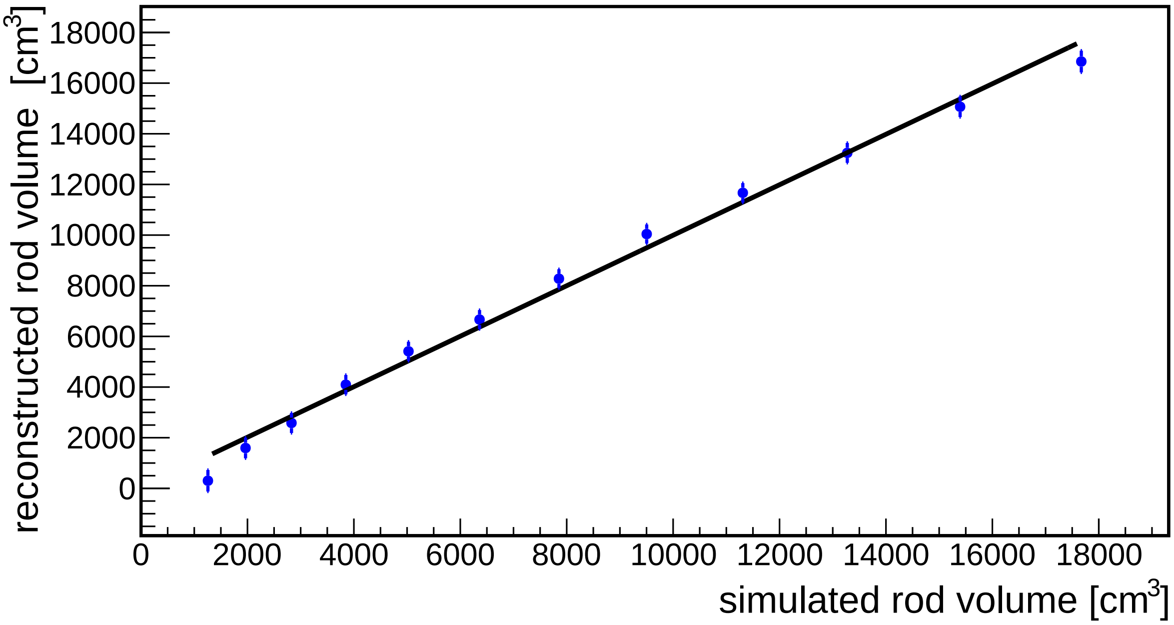

Figure 23: Reconstructed rebar volume as a function of the simulated (true) rebar volume [78].

Figure 26 shows images of the concrete only geometry and a geometry with a 50 mm diameter rebar inclusion in a fixed size concrete block. Each histogram's bin corresponds to a single sub-volume defined by a sliding window. The signal for the concrete only object (figure 26a, 26c and 26e) is clearly different from the signal obtained for the geometry with 50 mm diameter rod in concrete (figure 26b, 26d and 26f). In the ZY projection (figure 26b) a roundish object is visible in the centre of the block with the maximum signal of 1903. The shape is elongated in the Z-direction due to Z-blurring. This is a well-know effect caused by the fact that vast majority of the muons scatter with small angles and come almost straight from the top (the Z-direction). This results in large uncertainties on the position of the scattering vertex along the Z axis. This explains why the object is smeared. Nevertheless, the scattering vertices are very well defined in the X and Y direction. In the YX projection (figure 26d) a long object can be seen in the centre with the signal values varying locally between 400 and almost 600. The ZX histogram (figure 26f) is blurred in the centre because of Z-blurring, but has the signal stronger than the

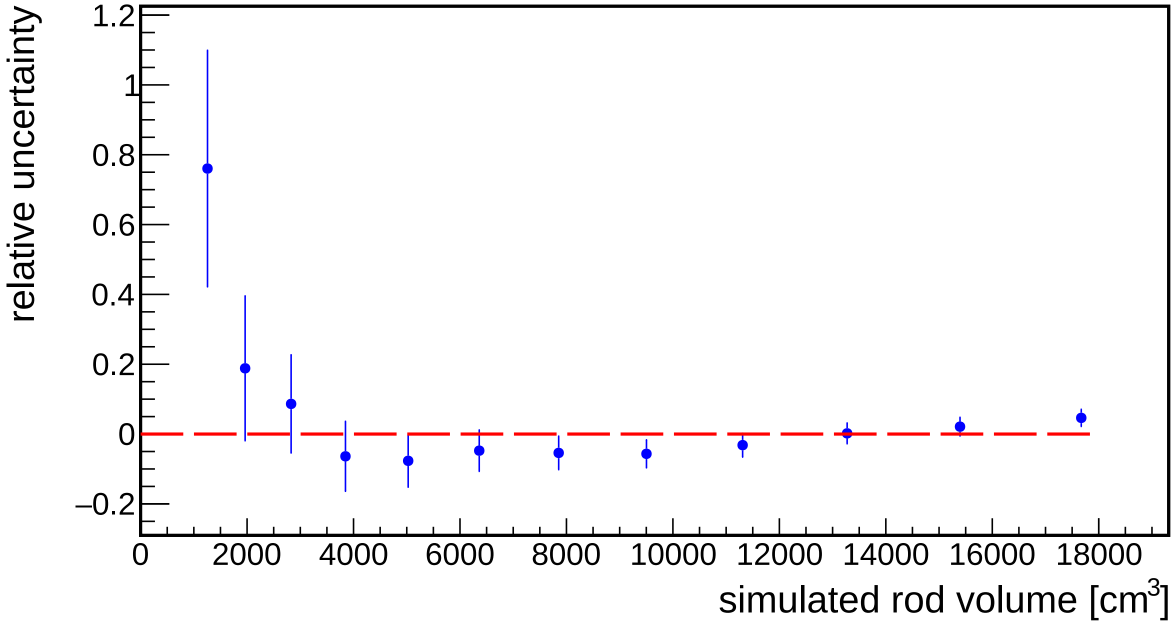

Figure 24: Relative uncertainty of the reconstructed volume as a function of the actual reinforcement volume [78].

signal produced for the concrete only geometry, where the signal oscillates around 300 for all projections.

The signal values are much higher for the sub-volumes where the iron rod is. For the ZY projection, a central region of the plot was defined as: X∈<40;55>, Y∈<10;35>. For this region, a one dimensional distribution of the signal was prepared, see figure 27. It can be clearly seen that with increasing size of the rod, more and more bins display higher signals. This was quantised by calculating the signal excess fraction. The signal from the concrete only was fitted with a Gauss which yielded mean of μ_b=307.22 ± 1.67 and sigma of σ_b=33.32 ± 1.24. The signal excess fraction is a fraction of signals larger than $\mu_b + 3\sigma_b$. Figure 28 shows the signal excess fraction as a function of rebar diameter. The expected increase is clearly visible.

Previously, it was shown that the minimal detectable diameter for a single rebar was 33.7 ± 7.3 mm for 100 cm long rod. However, the excess fraction shown in figure 27 and figure 28, indicate that smaller rebars, like a 20 mm diameter rebar, should be observable. Images of two rebars with smaller diameters than 33.7 mm in a fixed size concrete sample are shown in figure 29. The left column shows a rebar with a diameter of 20 mm in different projections, the right a rebar with a diameter of 30 mm. The maximum signal in the side view is 980 and 537 for 30 mm and 20 mm diameter rods, respectively. There is a hint of a long object in the centre with signal values around 400. Figure 29b clearly shows a 30 mm diameter rod and in figure 29a a hint of signal of 20 mm diameter rod is also visible by eye, despite being narrower than the previous lower detection limit. This

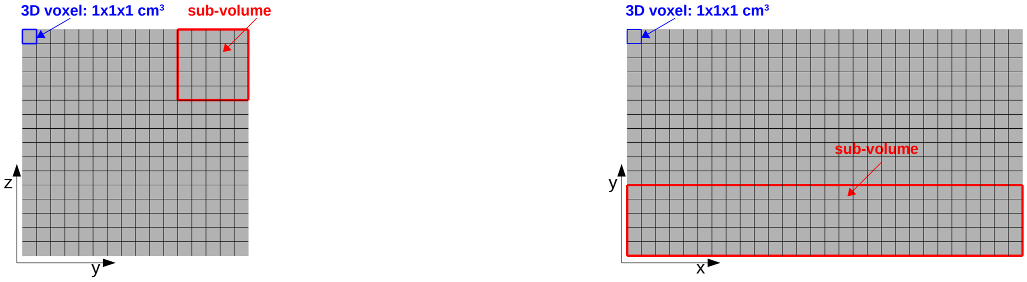

(a) Side (ZY) view.

(b) Top (YX) view.

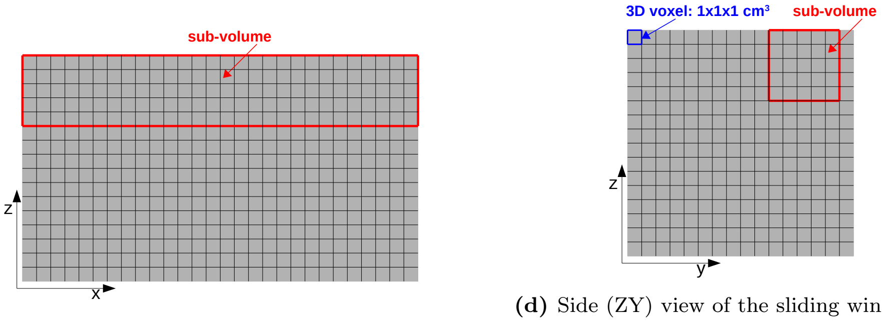

(c) Front (ZX) view.

(d) Side (ZY) view of the sliding window shifted by one voxel in Y direction.

Figure 25: The definition of the sliding window in ZY projection [78].

is because the initial method combines all signals over the entire block which inherently yields a higher background, while the comparisons in figure 29 clearly show that a bin by bin comparison can yield much better sensitivity.

To use the method in reality, it is important that the signal does not depend (too much) on the location of the rebar. This was studied by placing the 100 cm long rebar with a diameter of 30 mm inside the concrete block at four different locations. Signal graphs are shown in figure 30. In all cases, the rebar is still easy to detect. The method still works, even when the rod is close to the edge of the concrete object: in the ZY projections the local maxima are as follow: 834, 1263, 1446, 1021 for figure 30a, 30b, 30c, 30d respectively. This proves that the performance of the imaging method is not significantly dependent on the placement of the bar within the concrete block. In addition, it can be seen that the different location leads to a different signal pattern Thus, the location of the inclusion can be determined with this approach as well.
If two bars are included at different positions, they will be seen in muon image as separate objects as long as they are not too close to each other. To find the minimum distance between rods where they can be distinguished as two separate objects, concrete block with two 30 mm diameter rebars was simulated where the rebars were placed at different distances with respect to each other. Initially, the distance was set to 0 cm - the rods were touching each other. The distance was increased in steps of 2 cm. By subtracting all values blow the certain threshold, the separation between rods starts to be visible. The threshold was set at $\mu_b + 3\sigma_b$ where parameters are from the Gaussian fit to the one dimensional distribution of the signal from ZY projection of concrete only image. The

signal values were gathered only for the central region. Gaussian fit yielded a mean of 307.22 ± 1.67 and sigma of 33.32 ± 1.24. Signal images for distances up to 6 cm are shown in figure 31. The separation between rods starts to be visible when the spacing is at least 4 cm, they are fully separated when the distance is 6 cm and more. All of the above proves that with the imaging algorithm is possible to detect and evaluate position of the detected inclusion.

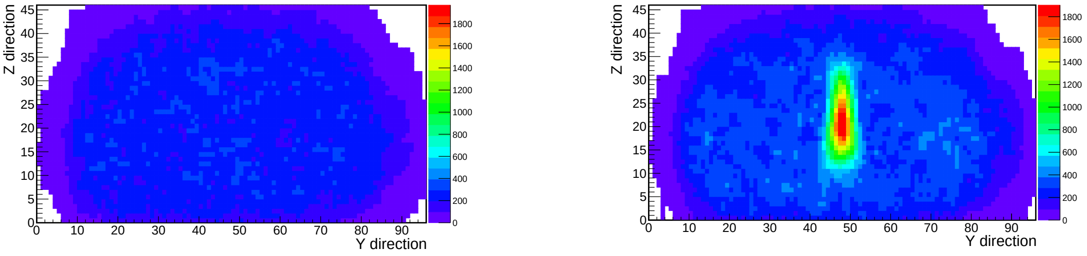

(a) concrete only: side view

(b) 50 mm diameter rebar: side view

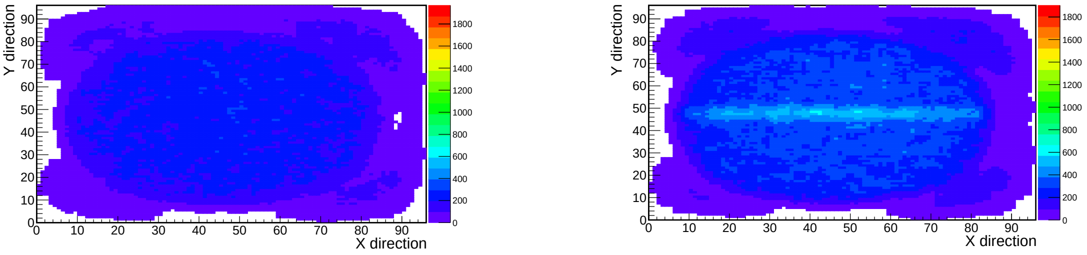

(c) concrete only: top view

(d) 50 mm diameter rebar: top view

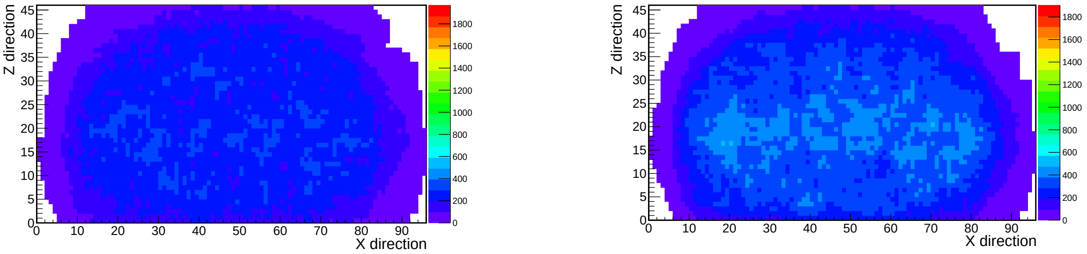

(e) concrete only: front view

(f) 50 mm diameter rebar: front view

Figure 26: Images of a concrete only geometry and images of the concrete block with a 50 mm diameter rebar [78].

5.2.5 Imaging of reinforcement

A particularly interesting inspection need is the detection and location of rebar grids. They are typically made from thin metal bars with a radius of 6 mm upwards with a spacing from 10 cm. A sketch of a grid is shown in figure 20. Since, in this scenario samples have different dimensions than discussed in previous chapters, new background samples were generated, see figures 32a, 32c, 32e. Signal distributions were prepared for the selected central region. The selected central region for the ZY and ZX projection was X∊<10;85>, Y∊<0;30>, for the XY projection it was X∊<15;75>, Y∊<15;75>. Gaussian fits to the distributions yielded means and sigmas of $\mu_{concr_{ZY}}$=311.17±1.00 and $\sigma_{concr_{ZY}}$=44.69±0.88, $\mu_{concr_{XY}}$=264.66±0.46

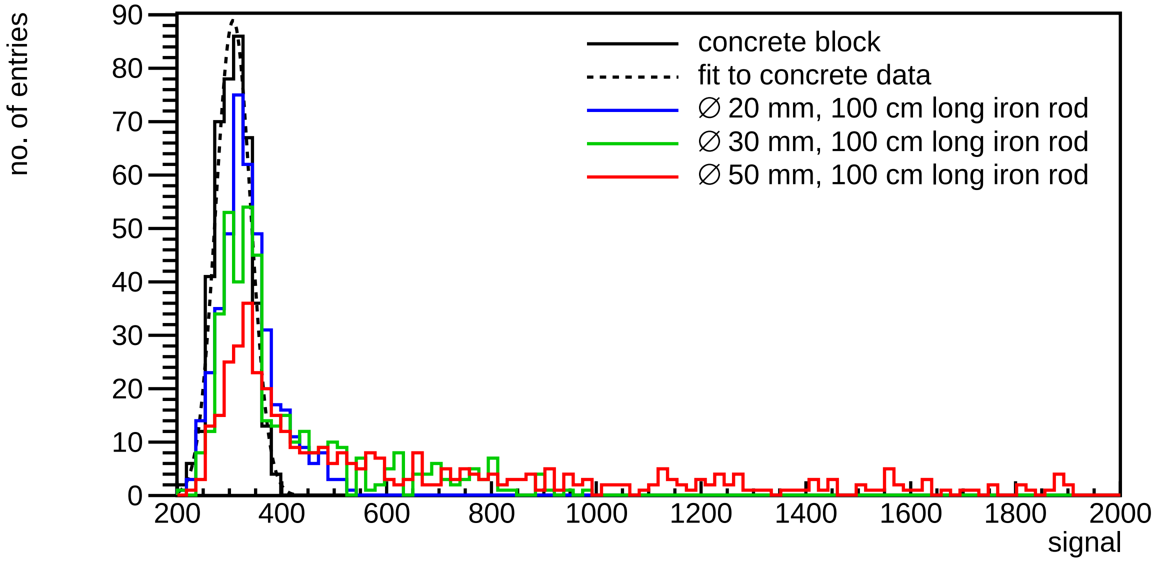

Figure 27: Signal distribution for a central region of a concrete only scenario and rebar with a diameter of 20, 30, and 50 mm. The Gaussian fit to concrete only data is also shown.

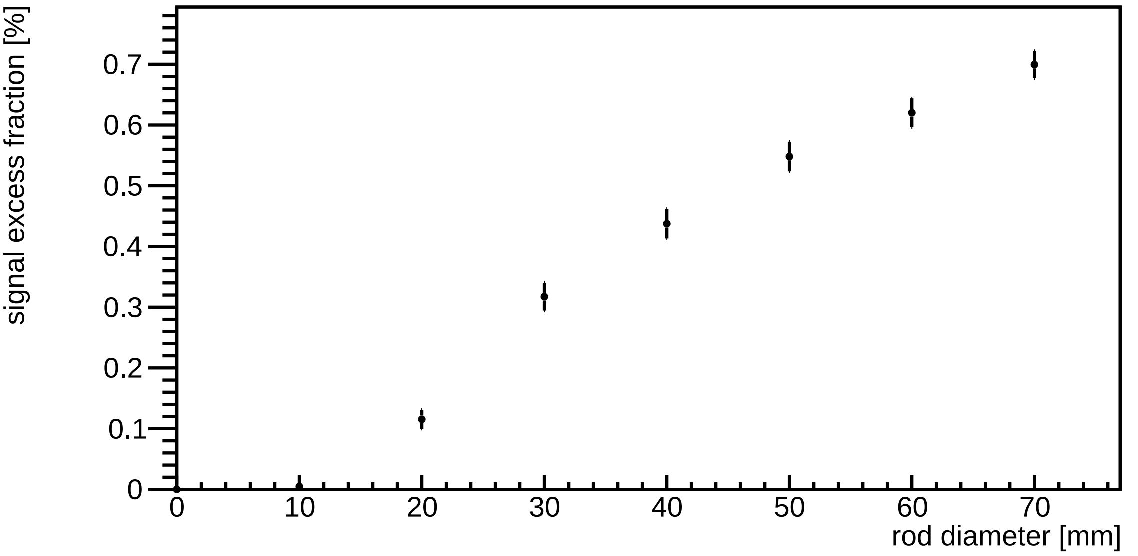

Figure 28: Signal excess fraction as a function of rebar diameter. Rebar diameters range between 0 and 70 mm. There is a monotonic rise with increasing the amount of iron inside the concrete block.

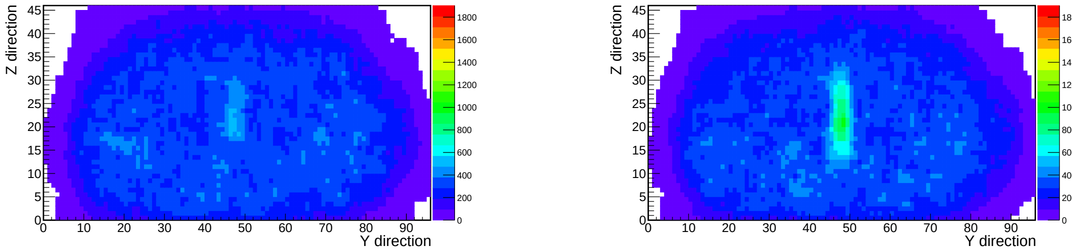

(a) 20 mm diameter rebar: side view

(b) 30 mm diameter rebar: side view

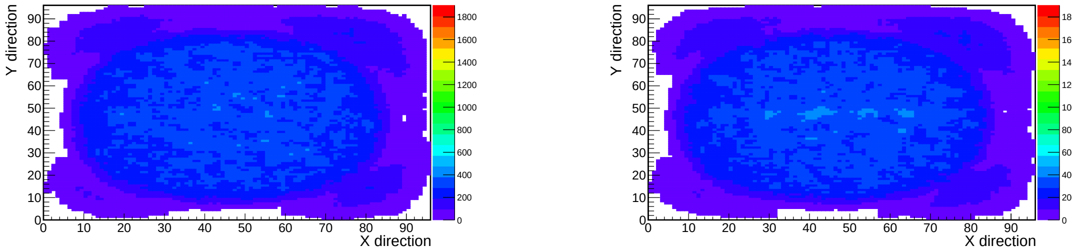

(c) 20 mm diameter rebar: top view

(d) 30 mm diameter rebar: top view

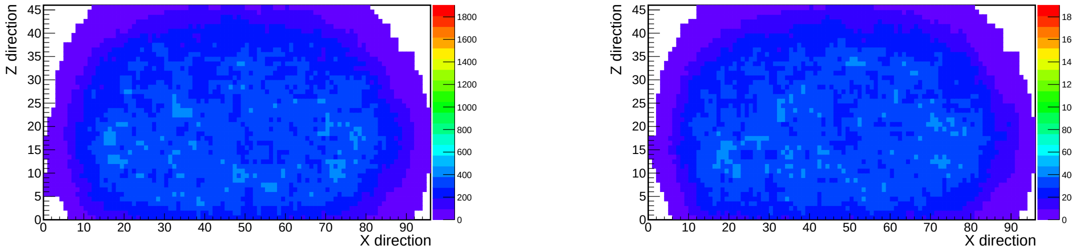

(e) 20 mm diameter rebar: front view

(f) 30 mm diameter rebar: front view

Figure 29: Images of a concrete block with a rod of 20 mm diameter (left) and rod of 30 mm diameter (right) [78].

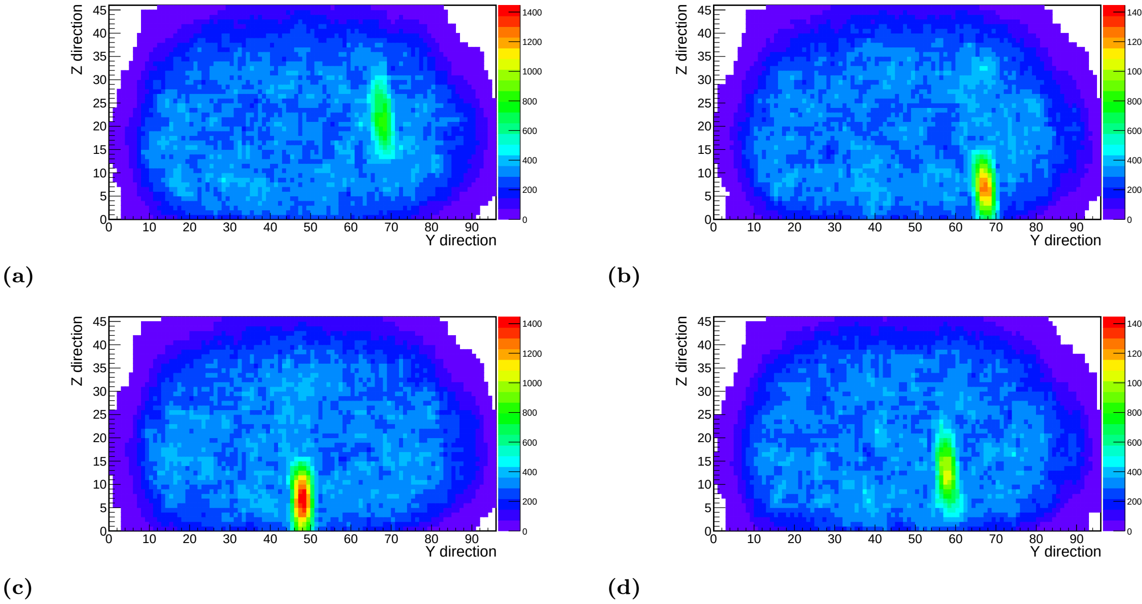

Figure 30: An iron rod with a diameter of 30 mm placed in 4 different locations of the concrete object [78].

and $\sigma_{concr_{XY}}$=26.53±0.35, $\mu_{concr_{ZX}}$=314.41±1.16 and $\sigma_{concr_{XY}}$=48.12±0.84.

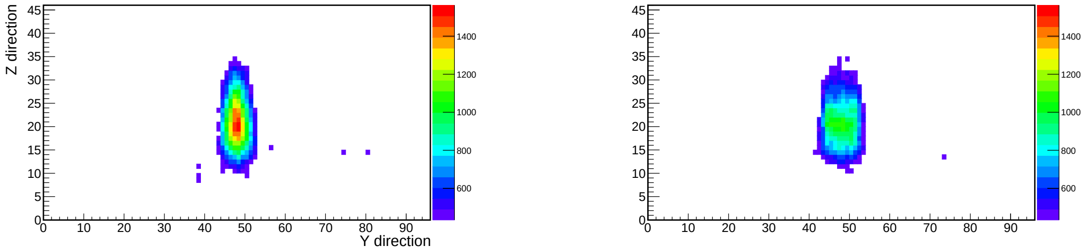

(a) No distance: side view

(b) 2 cm distance: side view

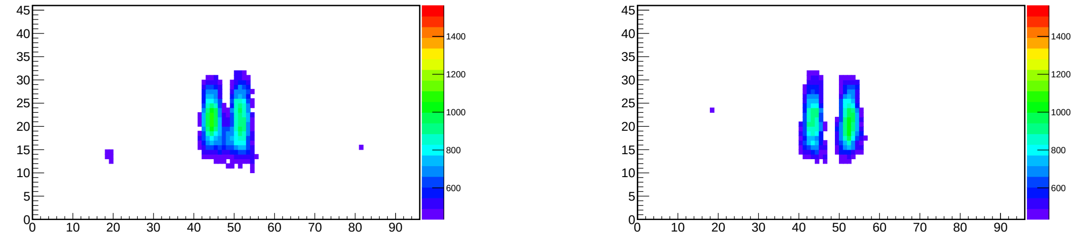

(c) 4 cm distance: side view

(d) 6 cm distance: side view

Figure 31: Images of two rods placed in different distances in respect to each other [78].

Next, a single layer of parallel iron rods along Y direction in a concrete sample was imaged, see figure 32b, 32d and 32f. In all of the projections the rebars are visible by eye and signal values are higher where the rods are present. The best image one gets from the side view where all simulated rebars are noticeable but they are smeared out due to the Z-blurring effect described in section 5.2.4. The four central rods have local maxima of 1647, 1758, 1693 and 1473. Edge rods are characterized by lower signals (local maxima of 1021 and 1036) due to limited detector acceptance. In the top (YX) view (figure 32d) only four rebars out of six are distinguishable by eye, again by the limited acceptance of the 1 × 1 m^2 detector used in this study, see chapter 4.2. By moving the detector or by using bigger detectors, the outer two rebars will become visible as well. In the ZX plane (rebar axial plane, figure 32f), the signal is much higher where the rebars are, however, due to the Z-blurring, the image is not so clear. The histogram of a signal from selected central region for this projection and concrete-only scenario is shown in figure 33. Adding rods in the concrete block results in higher signal values and the distributions shifts to the right with respect to the concrete-only case.

Figure 34 shows images of one layer of the reinforcement grid (left) and two layers of reinforcement grid (right). The maximum signal reaches 1792 in ZY projection of the one layer scenario which is similar to the single rods scenario. However, by adding a perpendicular layer of rods underneath the first layer, the signal increases locally compared to the rods only scenario. This reflects the additional amount of iron. In the top view projection, figure 34c, the grid pattern starts to be visible - where the bars intersect, the signal locally increases to values between 350 and 450. The double grid scenario (figures 34b, 34d and 34f) has even stronger signals and the grid is more clear than the signals from the single grid layer scenario. At intersections signal varies locally between around 520 and 630. In the ZX and ZY projections two layers merge into one because of the Z-smearing effect. Nevertheless, the area of the higher signal in Z extends over much larger area of Z direction and this feature can be used to distinguish between a single and a double layer of grid scenario. This proves that the imaging algorithm does work well for more realistic and complex cases and does show promise for practical applications. Detailed analysis about reinforcement grid is in chapter 6. More about study of two layers of grid is presented in chapter 6.7.2.

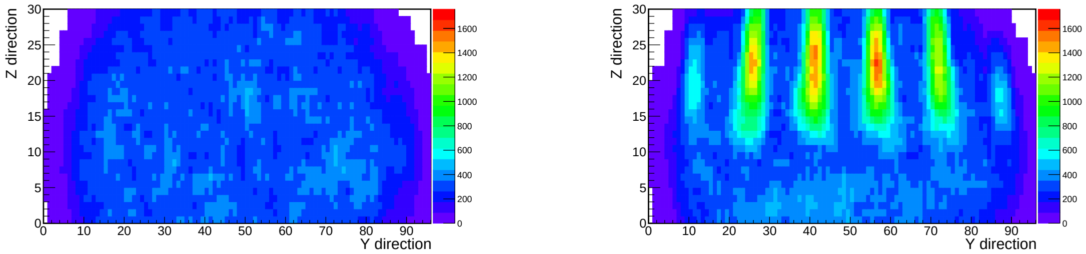

(a) concrete only: side view

(b) rebars: side view

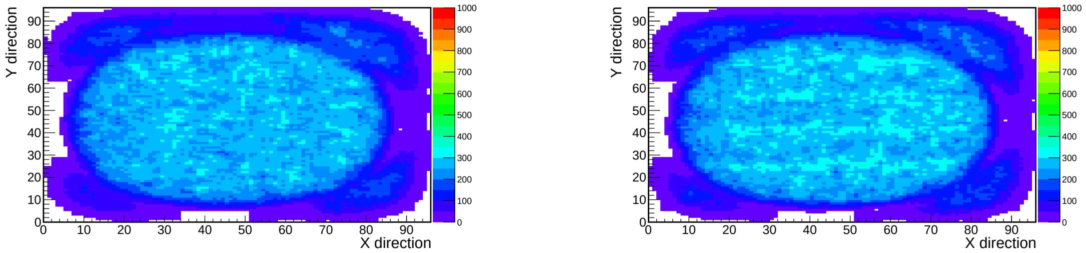

(c) concrete only: top view

(d) rebars: top view

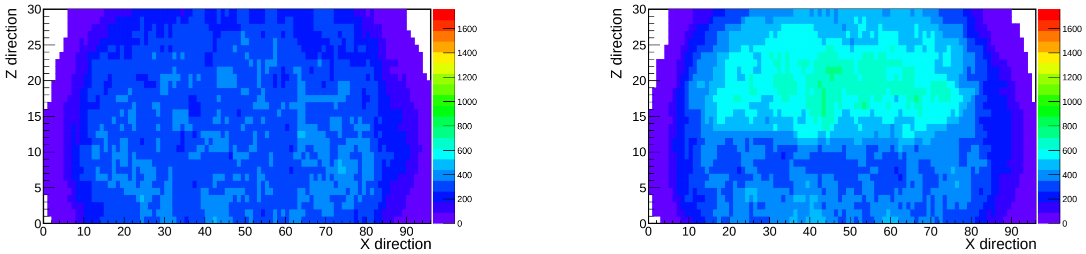

(e) concrete only: front view

(f) rebars: front view

Figure 32: Reinforcement imaging: concrete only sample (left) and one layer of 30 mm diameter parallel rebars with a spacing of 15 cm (right) [78].

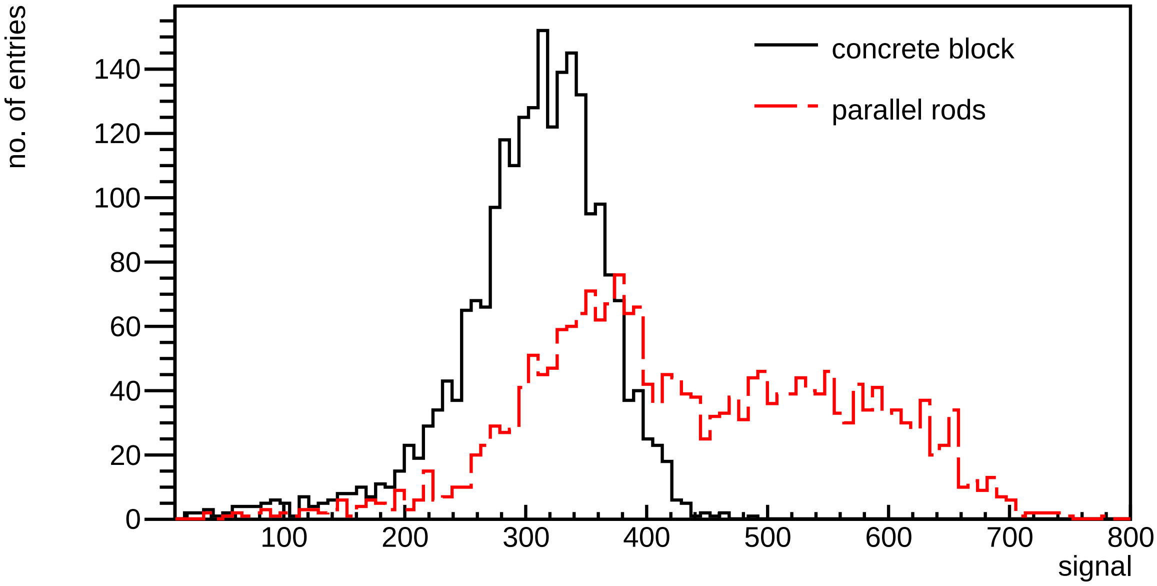

Figure 33: Distribution of the signal from a central region in ZX projection of the concrete-only case and a case with parallel rods. Added volume of iron is reflected by higher signal values.

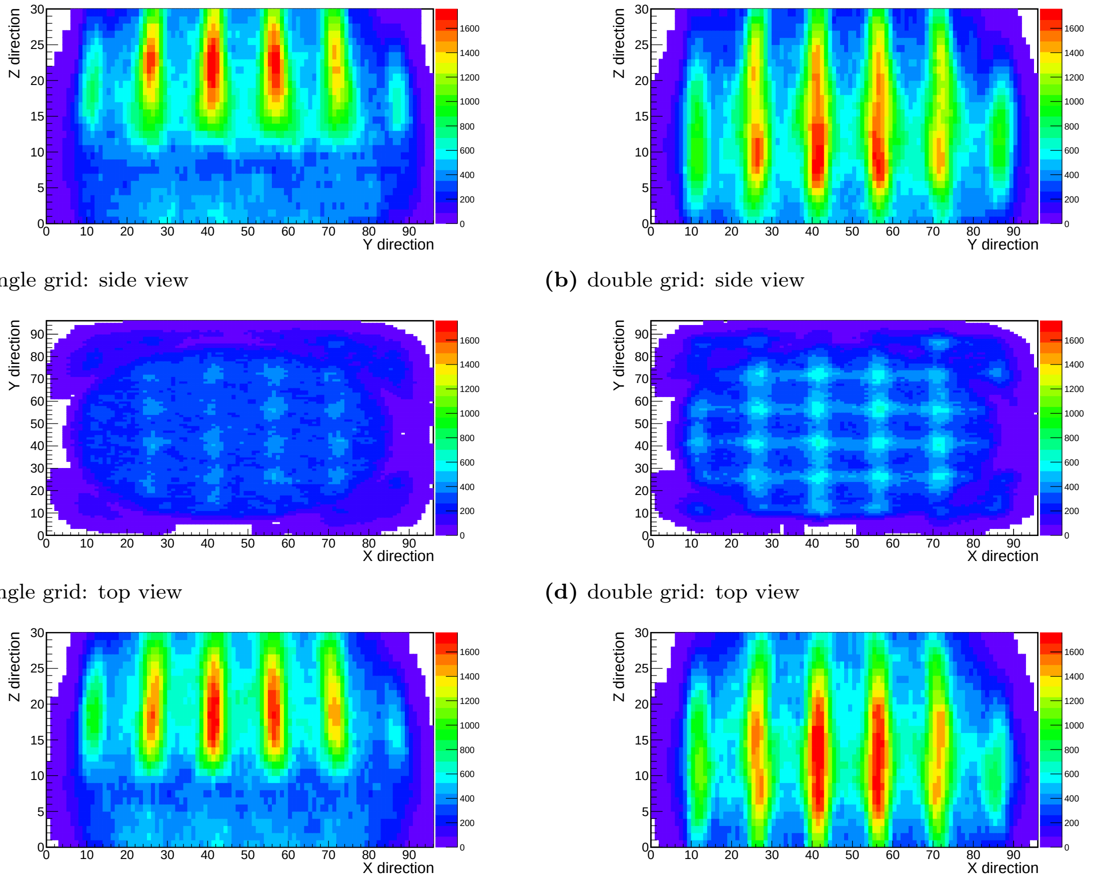

(a) single grid: side view

(b) double grid: side view

(c) single grid: top view

(d) double grid: top view

(e) single grid: front view

(f) double grid: front view

Figure 34: Reinforcement imaging: single (left) and double (right) 30 mm diameter rebar grid with a spacing of 15 cm [78].

5.3 Conclusions

Civil and structural engineering need NDE techniques to inspect the internal structures of concrete to detect, locate, measure and image reinforcement inside it at a high depth. Many methods exist but they do not fully fulfil the requirements. Using Monte Carlo simulations it was proven that MST is a technique to fill this gap. It was shown that with the metric method rebars with a minimum diameter of 33.7 ± 7.3 mm and a length of 100 cm are detected. Furthermore, it was shown that the signal has a monotonic dependence on the volume of iron in concrete. The volume of the inclusion is reconstructed with a resolution of 5.4% ± 0.3% and relative uncertainty below 10%, for rebar volumes above 2 500 cm^3. This result is independent of the rebar location. What is more, two rebars can be distinguished as two separate objects when they are placed 6 cm apart, but the separation starts to be present with a spacing of 4 cm. The technique also allows for the imaging of rebar structures in reinforced concrete and differentiation between single and double layers of rebar grids with rod diameters of 30 mm. Imaging algorithm also reduced the detectable diameter down to 20 mm.

These results prove that the presented method is a feasible way for the detection of iron rods and reinforcement in concrete structures. However, a diameter of 33 mm or 20 mm is relatively large for reinforcement. The next chapters present improvements to the method introduced to detect thinner rebars.

6 Improvement of the method for the detection of reinforcement in concrete

More study has been done to improve the method to detect smaller rods. In a previous chapter it was shown that the minimal detectable rod diameter is 33.7 ± 7.3 mm for 100 cm long rods and was improved down to 20 mm when using the imaging method. The next part of the analysis focuses on further development of the detection method to lower the minimum detectable rod diameter and to inspect complex reinforcement structures. For the research presented here, realistic dimensions of the reinforcement bars and reinforcing cages were used. Most concrete structure are reinforced with bars with diameters ranging between 8 mm and 40 mm [5]. The thinnest rebars in use are 6 mm in diameter, however for walls and bridges mostly bars with diameters of 10 mm are employed. The spacing of most reinforcing grids is 10 or 20 cm [6]. The goal was to lower the minimal detectable rod diameter to cover all rebar sizes and configurations.

When inspecting rebars, the fact that reinforcement is a periodic structure can be exploited. Therefore, much smaller bars within shorter time can be detected than for single bars. To contain a few periods, larger detectors of 200 × 200 cm^2 were used and the time of data taking was one week unless otherwise stated. The number of most scattered tracks for a voxel to be considered, N of 30, was used.

6.1 Simulation study scenarios

The reinforced block was modelled as a concrete-filled block with dimensions of 200 cm × 200 cm × 32 cm. A single reinforcement grid, which was made of two orthogonal layers of parallel rods, was put inside the concrete sample. Throughout the simulations, the diameter of the rebars varied from 6 mm to 20 mm, a spacing of the rods of 7.5 cm, 10 cm, 15 cm or 20 cm was used, see figure 35. As a background reference, a concrete block with no reinforcement inside was simulated as well. The initial data collection period was equivalent to one week of normal data taking at sea level.

The operation of the algorithm to detect rebars will be explained using a concrete block with a single reinforcement grid made of bars with diameter of 15 mm and a spacing of 15 cm. The method relies on a better background subtraction followed by exploiting the periodicity using a method similar to auto-correlation and a Fourier transform.

6.2 Improved background removal

The first step in the development of the method towards grid detection is using an improved approach for background removal. First, the signal strength histograms (or images) of three projections of the scanned reinforced sample were prepared as explained in section 5.2.4.

Following, two reference samples filled with concrete only were simulated and histograms of the background signal strength were prepared. The reinforced concrete sample and background only sample had the same dimensions. Then, bin-by-bin, the histogram with background signal strength was subtracted from the histogram with reinforced concrete signal strength. This way of background removal was employed because the background is not linear. An example of the images of the reinforced concrete case before and after additional background subtraction is shown in figure 36. Higher signal indicates where the rods are, areas with lower signal show where the concrete is.

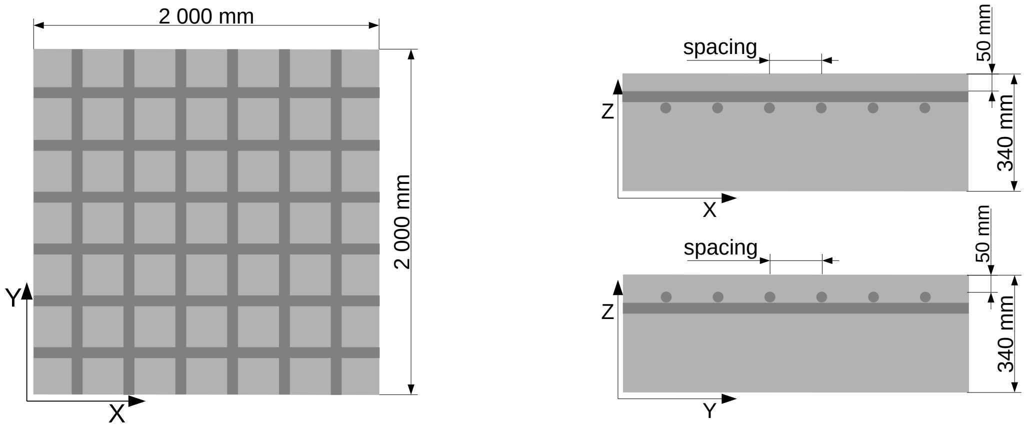

(a) Top (YX) view

(b) Front (ZX) view and side (ZY) view

Figure 35: A single layer of a grid [77].

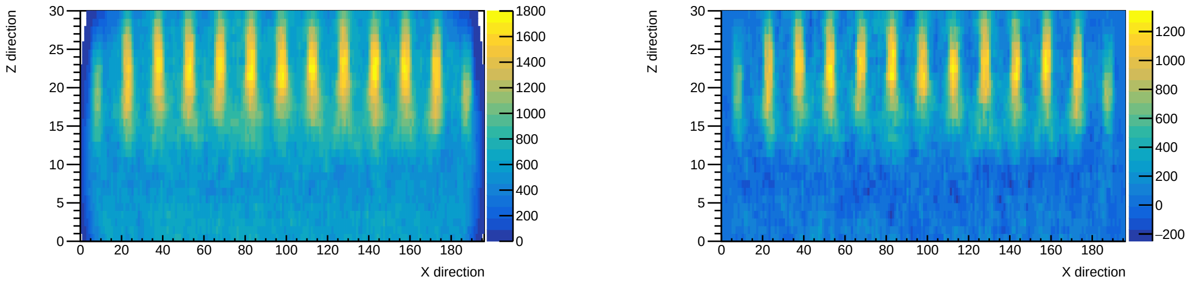

(a) Before background removal.

(b) After background removal.

Figure 36: Reinforcement imaging before (left) and after background removal (right) for a standalone reinforcement grid of 15 mm diameter rebars [77].

6.3 Exploiting the periodicity of the reinforcement

The reinforcement is a repetitive structure in a form of a grid and thus the analysis will yield a periodic signal. This fact can be used to detect the presence of the reinforcement and to reduce the minimal detectable rod diameter. In short, the signal from reinforcement is enhanced by calculating the auto-correlation of the 2D signal strength images. Next, the Fourier transform is calculated and in the resulting spectrum, peaks which are local maxima, can be found. These peaks contain information about reinforcement features -

the peak amplitude depends on the diameter of the rebars and the peak locations indicate the spacing between the rebars.

As can be seen in figure 36b, there is a repeating pattern with 15 cm spacing in the X direction. To extract this periodicity, a modified version of auto-correlation, R_s, was used, which is defined as follows:

$$R_s(\tau) = \int_{y_{min}}^{y_{max}} \int_{x_{min}}^{x_{max}} f(x', y') f(x' + \tau, y') dx' dy' \tag{11}$$

where f is the two-dimensional histogram (image) of the background subtracted signal strength as described in chapter 5.2.4 and chapter 6.2 and the τ is the shift. Due to the acceptance of the detector and the presence of the reinforcement in figure 36b, limits of the auto-correlation calculations were set to $x' \in$<20;175>, $y' \in$<10;29> and since the periodicity is in both X and Y directions, the auto-correlation is only calculated in X direction. The data was zero-padded to enable the calculation. The 2D data used to perform auto-correlation were also called a mask. The result of the auto-correlation process is shown in figure 37. The plot is triangular in shape because of the changing of the overlapping area while performing this auto-correlation calculation. The triangular background under the plot must be estimated and subtracted before a Fourier transformation can be applied. To approximate it, the auto-correlation was repeated introducing an additional shift, where the function f was modified to become periodic as illustrated in figure 38, introducing an extra shift Δ:

$$R_{b,k} = \int_{y_{min}}^{y_{max}} \int_{x_{min}}^{x_{max}} f(x', y') f(x' + \Delta_k + \tau, y') dx' dy' \tag{12}$$

where k indicates the number of columns the image has been shifted. The column shift takes place in a rolling mode, i.e. when a column is shifted further than x_{max}, it is placed in first column on the left. The shift is repeated until first column is back to its initial place. This approach results in a shift in the peak locations, but the triangular background remains unchanged, as can be seen in figure 39. Next, for every bin of the combined auto-correlations plot (figure 39) the minimum value of $R_{b,k}$ was found for every value of x, and that value was subtracted from the auto-correlation with no shift, see the red line in figure 39. The outcome is shown in figure 40. The triangular shape of the amplitude remains, but the triangular background under the function is removed.

Next, the background-subtracted result of the auto-correlation approach is subject to a Fourier transformation, where the space domain is transformed into a frequency domain. The transformation was performed using a ROOT class called TVirtualFFT [79] for Fast Fourier Transforms (FFT). The outcome of the FFT for the scenario with 1.5 cm diameter bars and a 15 cm spacing is shown in figure 41. A scenario with reinforcement is characterized by definite peaks. Due to the nature of the Fourier transform and applying FFT on a real signal, the normalized frequency spectrum is symmetrical. As shown, the peaks do not occur when the grid is not present. These results prove that with this approach, the detection of the bar grids is possible.

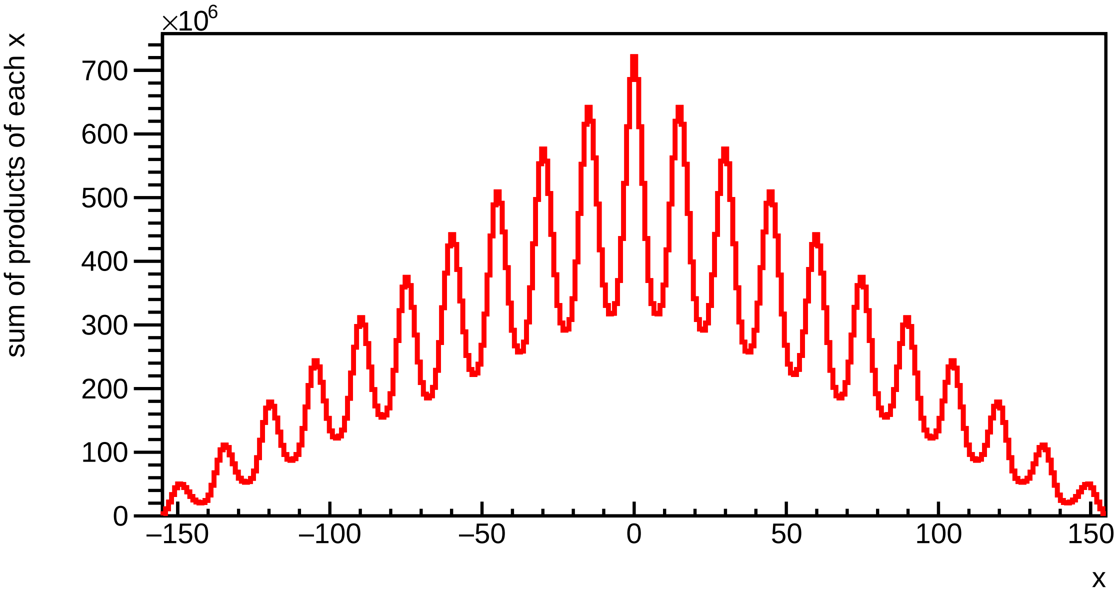

Figure 37: Result of the auto-correlation approach for the example case [77].

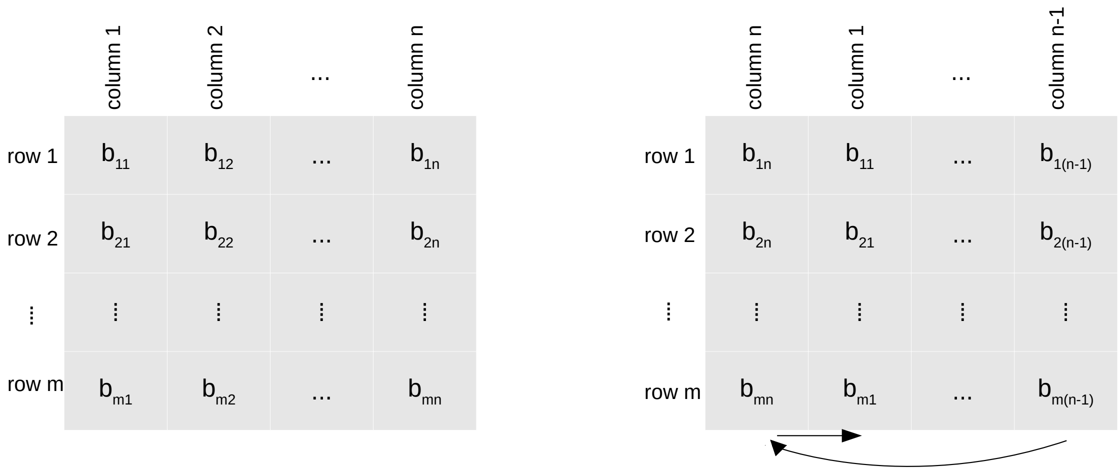

(a) Initial image with no shift.

(b) Image with one column shift.

Figure 38: Scheme of the column shift Δ_k, where b_{ij} is a bin number [77].

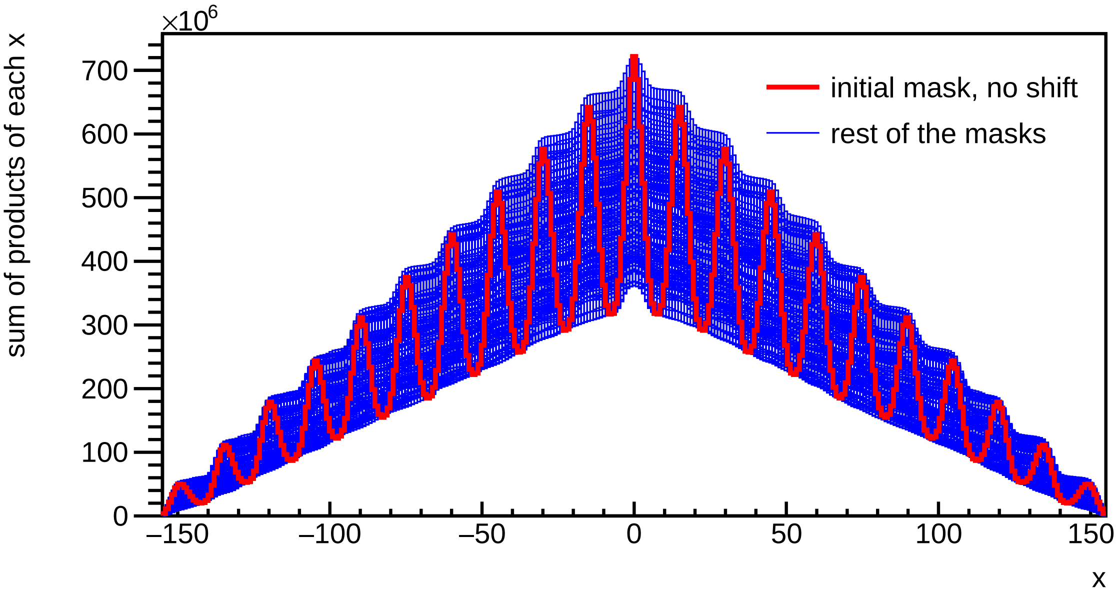

Figure 39: Result of the auto-correlation approach with additional shifts [77].

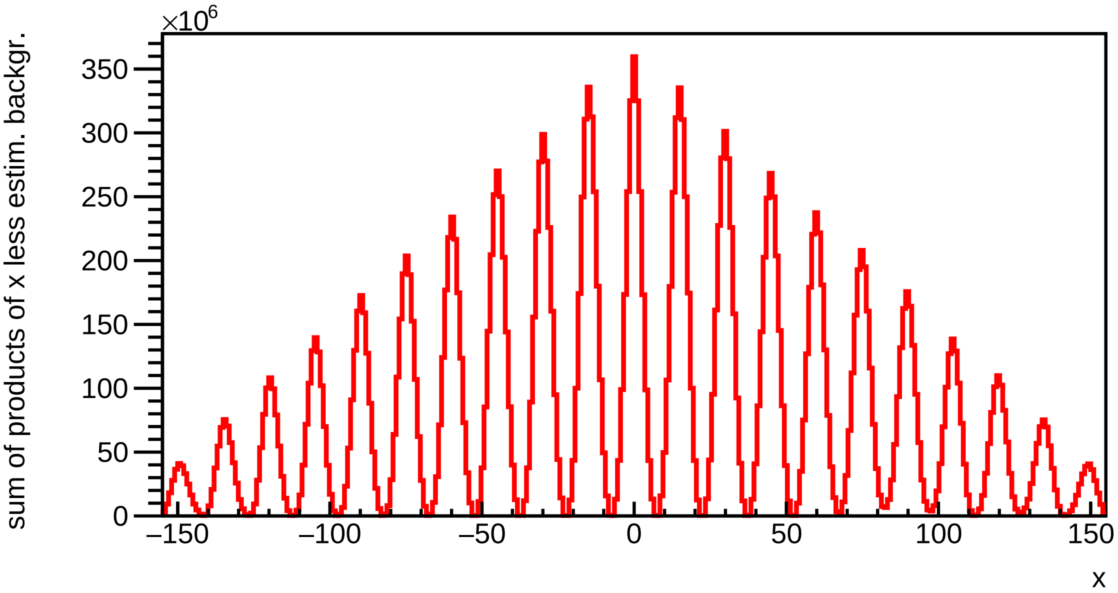

Figure 40: Result of the auto-correlation approach after triangular background subtraction [77].

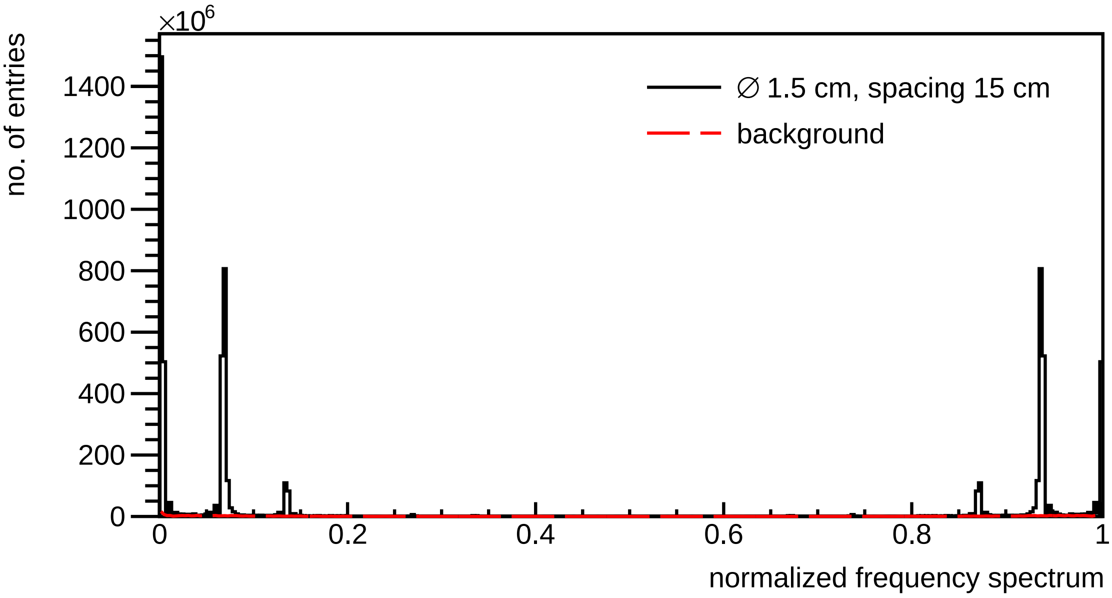

Figure 41: A Fourier frequency spectrum for the example with 1.5 cm diameter bars and a 15 cm spacing [77].

6.4 Dependence on the rebar diameter

Peaks in the Fourier spectrum contain information about the metal grid used to reinforce big concrete structures. In this section, the rebar diameter will be varied to see how the Fourier frequency spectrum changes. To do so, additional simulations of the rebar grid were made, containing rebars with a diameter of 20, 15, 10, or 8 mm with the spacing fixed at 15 cm. Figure 42 shows Fourier frequency spectra for these cases. A zoomed version is shown in figure 43. For all cases, the peaks occur in the same locations. This is as expected since the same spacing was used for all of the cases. The amplitude of the peaks increases with increasing diameter of the rod. This is more clearly visible in figure 44, where the amplitude of the peak at a frequency of 0.07 as a function of rebar diameter is shown. The amplitude grows monotonically. Even for the smallest tested diameter of 8 mm, the signal is still much higher than the background yielding $(27.9\pm0.9)\cdot10^6$ for 8 mm diameter rod and $(2.6\pm0.3)\cdot10^6$ for background. The amplitude for 10 mm diameter rebar was $(120.5\pm0.9)\cdot10^6$, for 15 mm diameter rebar was $(806.8\pm10.5)\cdot10^6$ and $(2386.1\pm25.5)\cdot10^6$ for 20 mm diameter rebar. Thus, the rebar diameter can be measured using the peak amplitude.

6.5 Extracting the rebar spacing

The peaks in the Fourier spectrum also give information about the grid spacing. To study this, the spacing of the rebar grid was varied. A number of simulations with a grid consisting of rebars with the fixed diameter of 8 mm and spacings of 20, 15 or 10 cm were performed. Figure 45 shows normalized frequency spectra for different spacings. A zoomed version of the plot is shown in figure 46. Clear peaks are observed for all rebar scenarios but not for the concrete only background case. Changing of the rebar spacing, results in moving of the peak position. Thus, the bar spacing can be extracted from peaks positions.

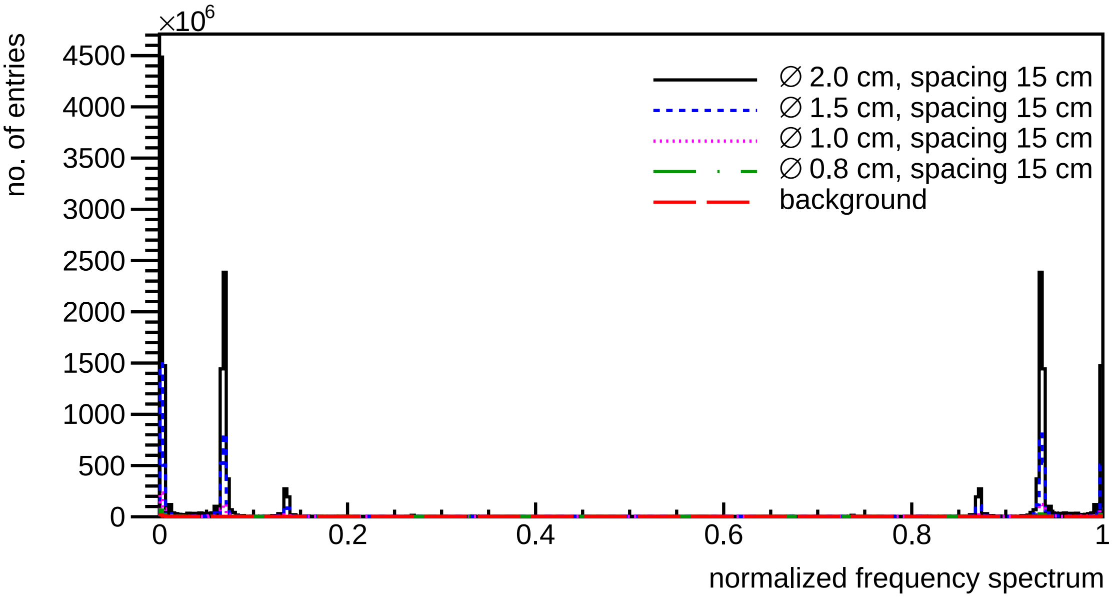

Figure 42: Fourier frequency spectra for different rebar diameters with a fixed spacing of 15 cm [77].

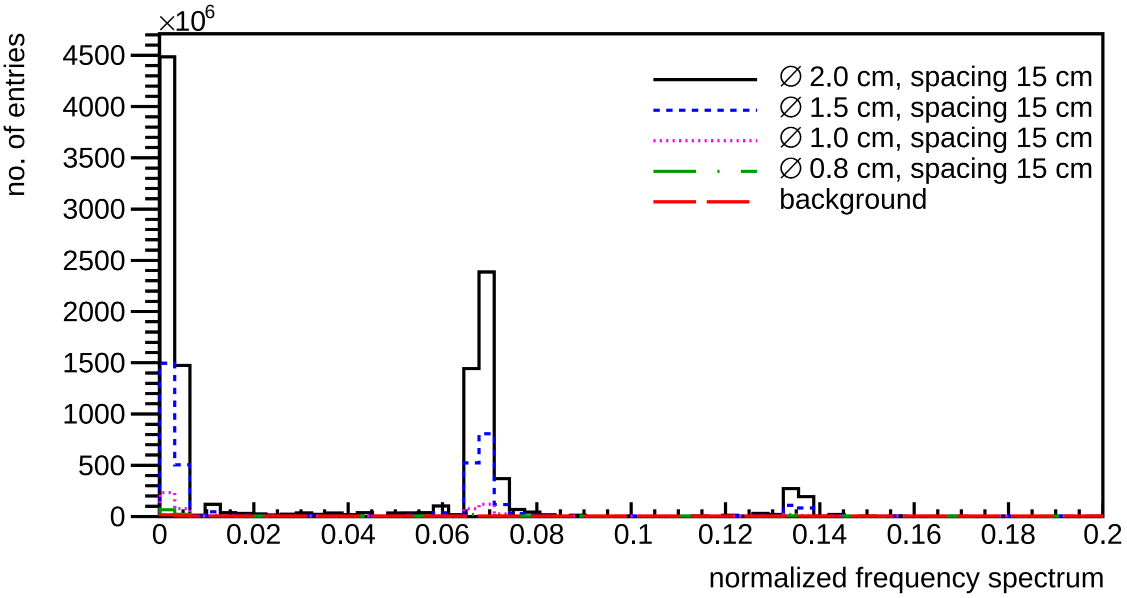

Figure 43: Zoomed version of the Fourier frequency spectra for different rebar diameters with a fixed spacing of 15 cm [77].

6.6 Detecting the smallest rebars used in industry

The above demonstrates that rods with a diameter of 8 mm can be detected within a week of data taking. The smallest rebars used in industry have 6 mm diameter. To study the potential of the technique to detect these rebars as well, additional studies of simulations

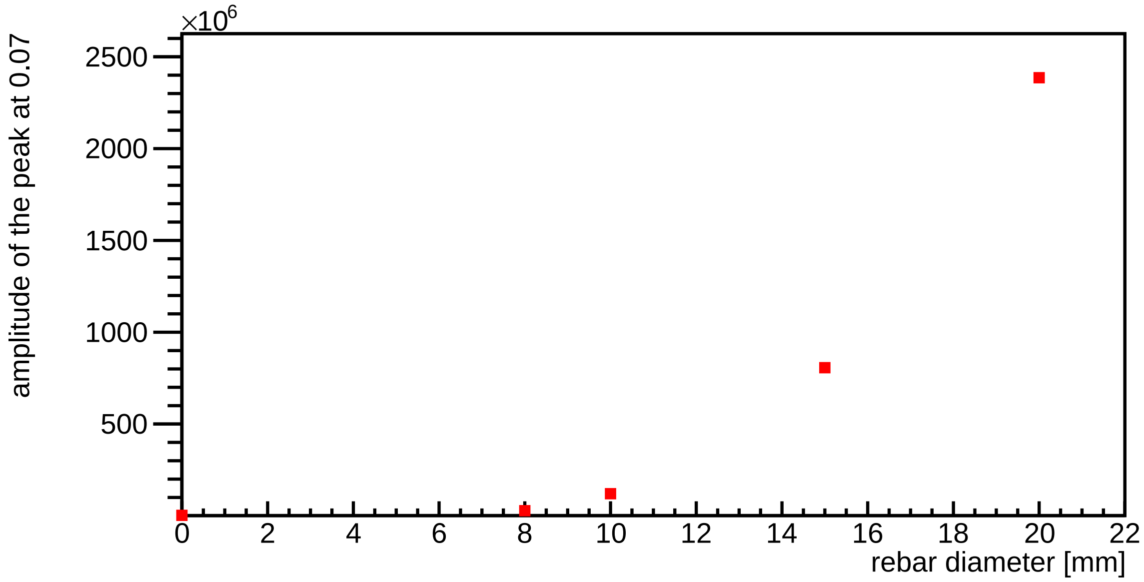

Figure 44: The amplitude of the peak at the frequency of 0.07 as a function of the bar diameter, where the spacing was fixed at 15 cm. The dependence between the rebar diameter and the peak amplitude is monotonic: the bigger the diameter, the higher the amplitude [77].

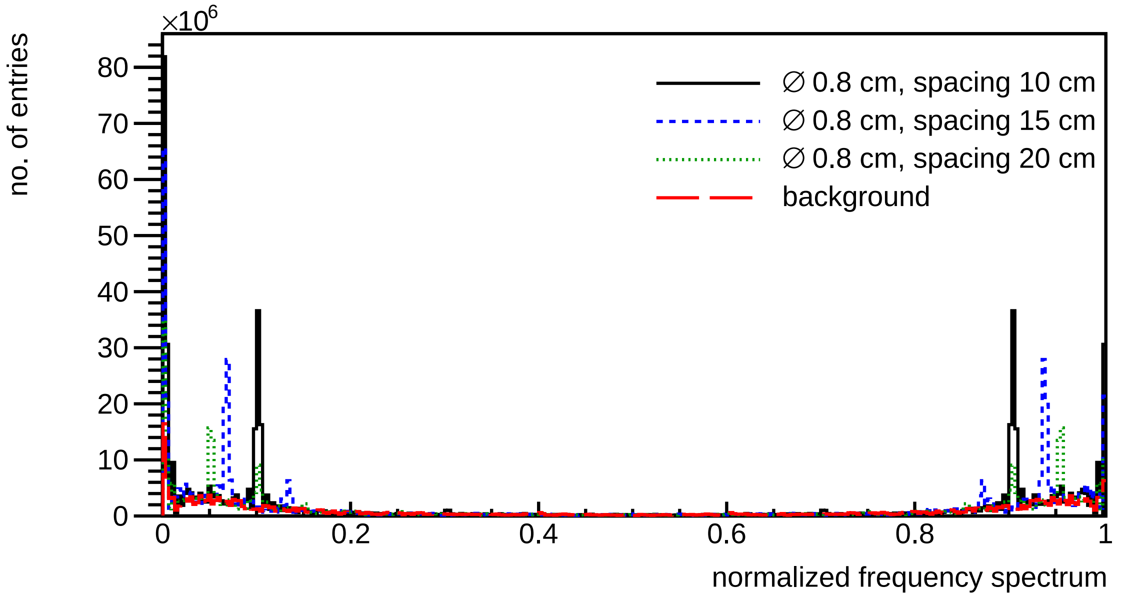

Figure 45: Fourier frequency spectra for different rebar spacings with a fixed rebar diameter of 8 mm [77].

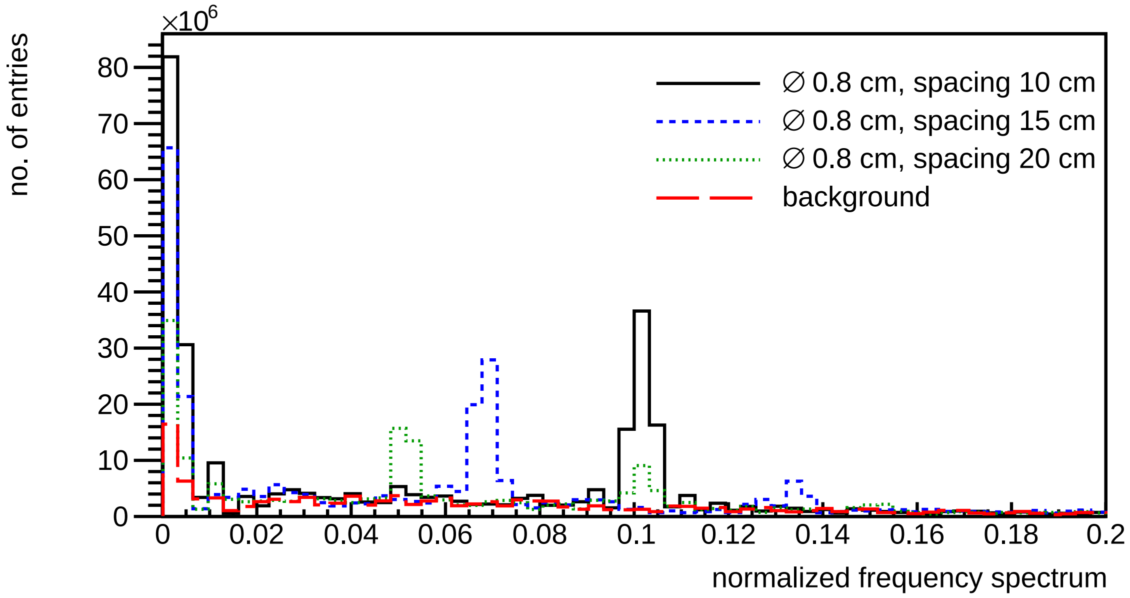

Figure 46: A zoomed version of the Fourier frequency spectra for different rebar spacings with a fixed rebar diameter of 8 mm [77].

were made where the rod diameter was decreased to 6, 7 or 8 mm with the spacing of 10 cm. One week equivalent of data was used. The results of the Fourier transforms are shown in figure 47 and the zoomed version in figure 48. Rebars with a diameter of 7 and 8 mm at frequency values of 0.1 and 0.9 are clearly separated from the background sample. The amplitude peak at 0.1 was (18.8±1.1)·10^6 for 7 mm and (36.6±1.1)·10^6 for 8 mm diameter rebars. The peak for the 6 mm diameter case is well above background as well with an amplitude of (6.4±0.2)·10^6 but with the background sample having an

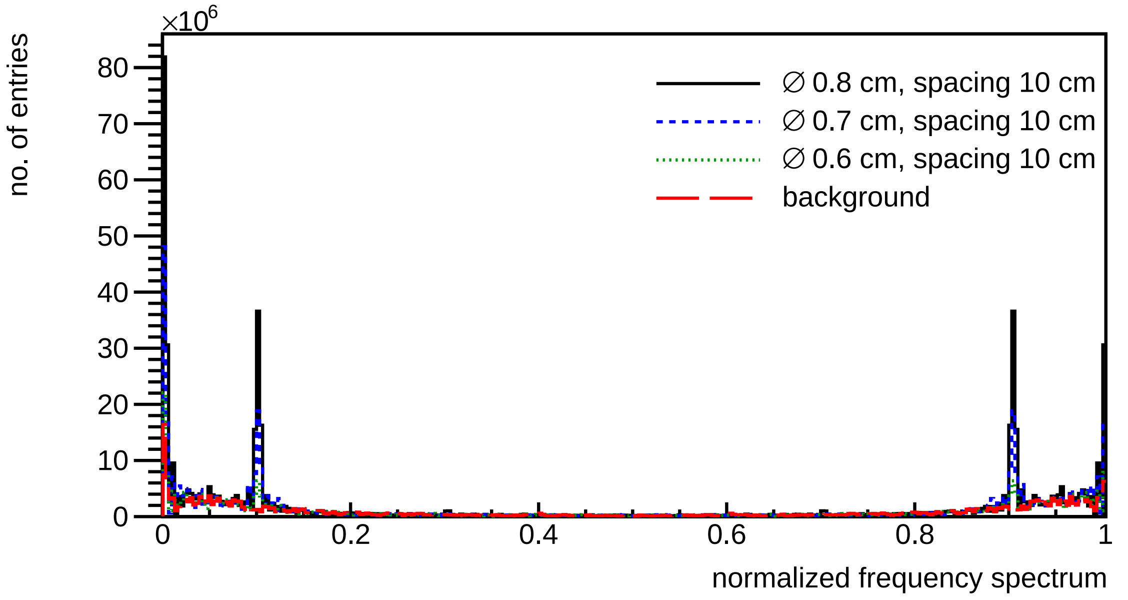

Figure 47: Normalized Fourier frequency spectra for a grid made of rebars with 6, 7 or 8 mm diameter and a spacing of 10 cm [77].

amplitude of (1.3±0.2)·10^6 the separation is less clear. The signal can be enhanced with taking more data.

Figure 49 shows the same spectra using the equivalent of two weeks of data. A zoomed version is shown in figure 50. The signal for the 6 mm diameter rod increased to (10.8±0.3)·10^6 after extending the data taking to two weeks equivalent. The background remained the same within errors at (2.3±0.5)·10^6. As expected, the extra data taking time results in a much clearer reparation between signal and background. Figure 51 shows the amplitude of the peak at 0.1 of the normalized frequency spectra for one and two weeks of data taking as a function of the rebar diameter. Undoubtedly, the rebars with the smallest diameter used in industry can be detected with MST when the spacing is 10 cm.

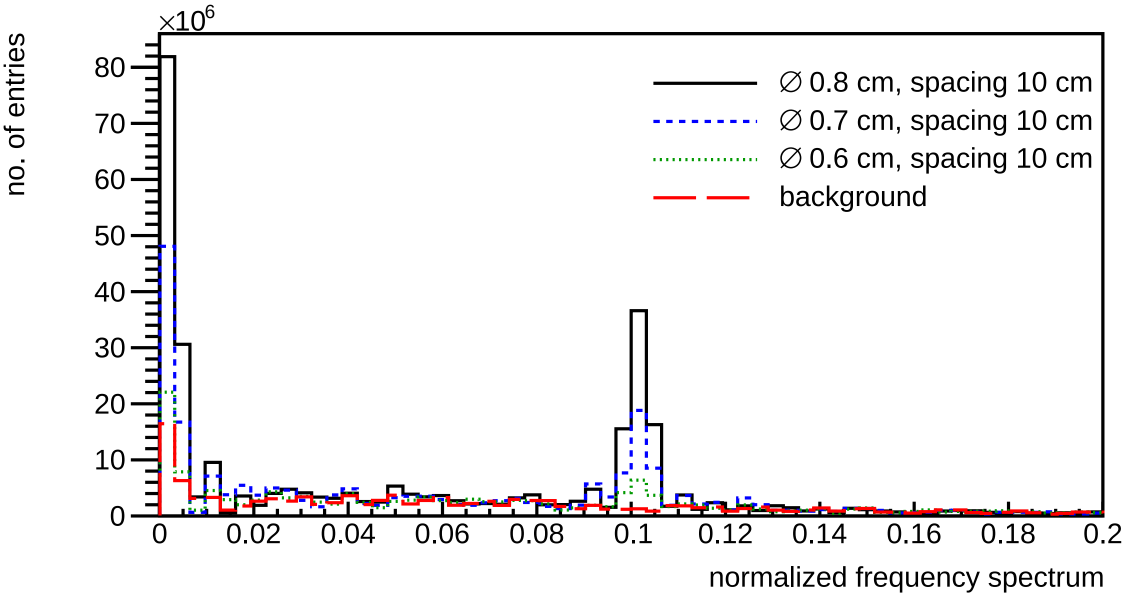

Figure 48: Zoomed version of the normalized Fourier frequency spectra for a grid made of rebars with 6, 7 or 8 mm diameter and a spacing of 10 cm [77].

As shown in section 6.5, the signal for larger spacings is lower. Therefore, the study was repeated with a spacing of 20 cm. When the bigger spacing is used, less metal is contained in the scanned area, thus the signal from the reinforcement is not as strong. This is shown in figure 52, where the normalized frequency spectra for a grid made of 6, 7 or 8 mm diameter rods and a 20 cm spacing after one week equivalent of data taking is shown. A zoomed version is shown in figure 53. Scenarios with 7 and 8 mm diameter rods are clearly distinguishable from the background, yielding an amplitude of the peak at 0.05 of (10.5±0.2)·10^6 for 7 mm diameter rod, (15.7±0.4)·10^6 for 8 mm diameter rod and (3.7±0.6)·10^6 for background. Unfortunately, the signal for the 6 mm diameter rod does not significantly exceed the background level with the amplitude of (4.8±0.7)·10^6. To increase the signal separation, two weeks equivalent of data taking were used and figure 54 shows the outcome of this study. A zoomed version of the plot is shown in figure 55. The signal for the 6 mm diameter rebar is clearly above background after two weeks equivalent

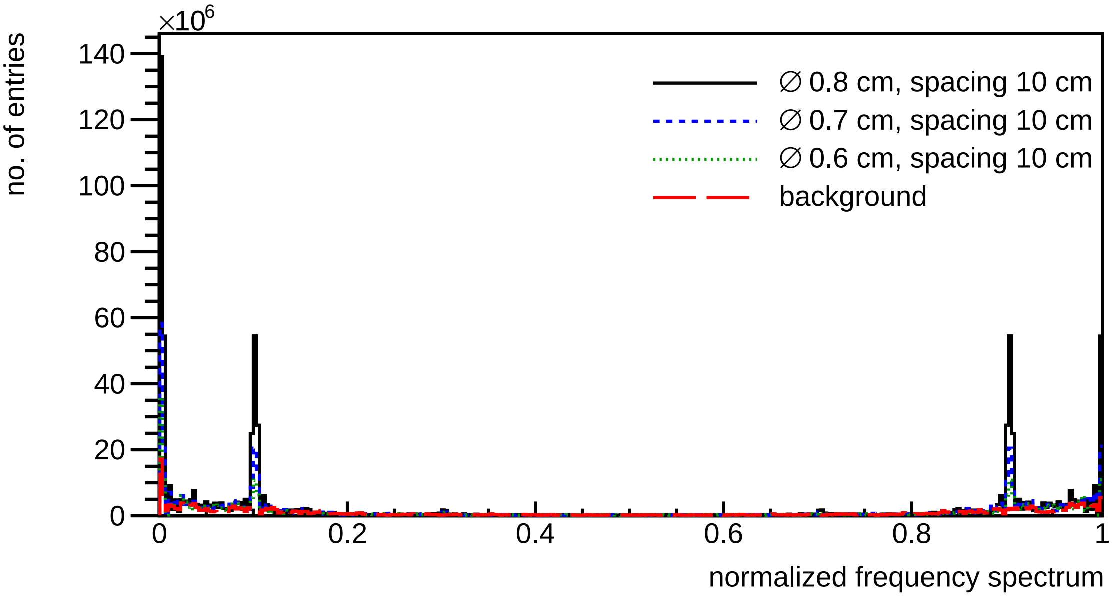

Figure 49: Normalized Fourier frequency spectra for a grid made of rebars with 6, 7 or 8 mm diameter and a spacing of 10 cm. Two weeks equivalent of data were used [77].

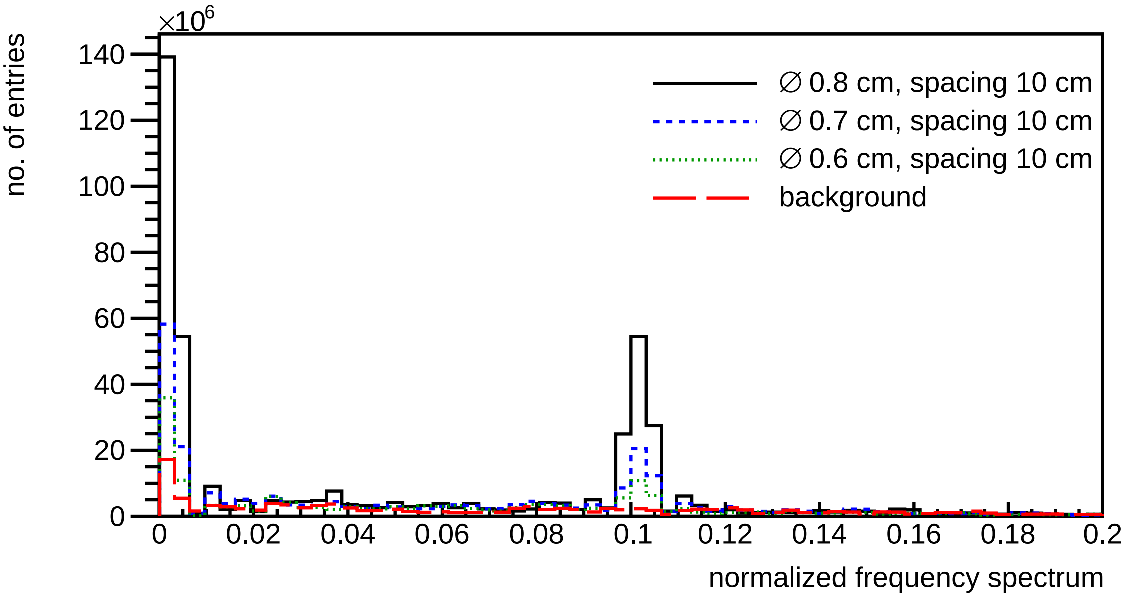

Figure 50: Zoomed version of the normalized Fourier frequency spectra for a grid made of rebars with 6, 7 or 8 mm diameter and a spacing of 10 cm.Two weeks equivalent of data were used [77].

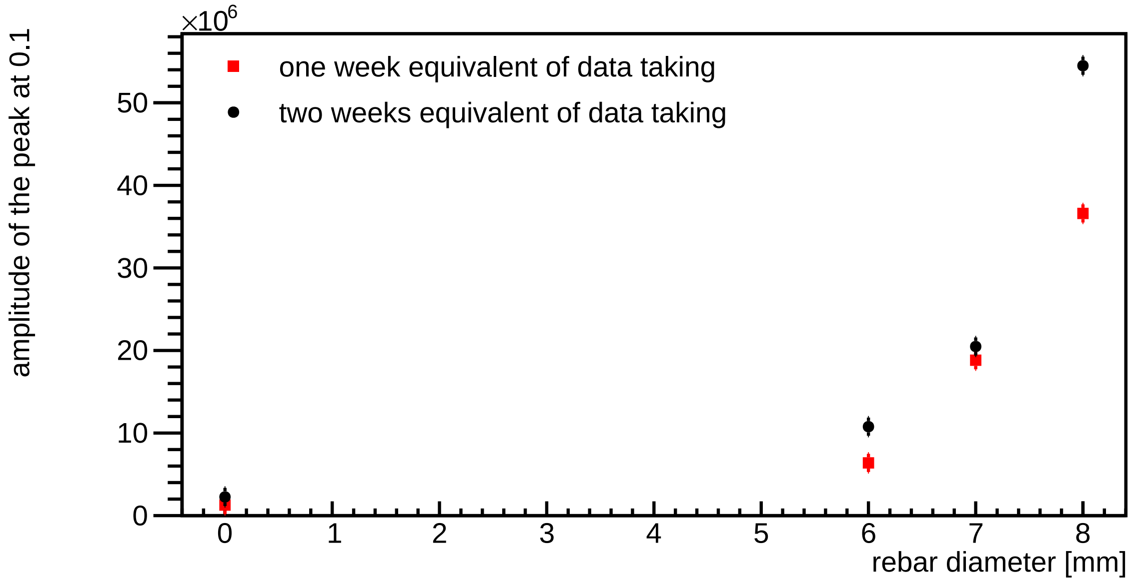

Figure 51: Amplitude of the peak at 0.1 of the normalized frequency spectra and a fixed spacing of 10 cm as a function of rebar diameter [77].

of data taking. The amplitude of the peak at 0.05 was (6.4±0.7)·10^6. The background remained the same within errors at (2.2±0.4)·10^6. Figure 56 shows the amplitude of the peak at 0.05 of the normalized frequency spectra for one and two weeks of data taking as a function of rebar diameter. Undoubtedly, the rebars with the smallest diameter used in industry can be detected with MST even when the spacing of 20 cm is used using the equivalent of two weeks of data.

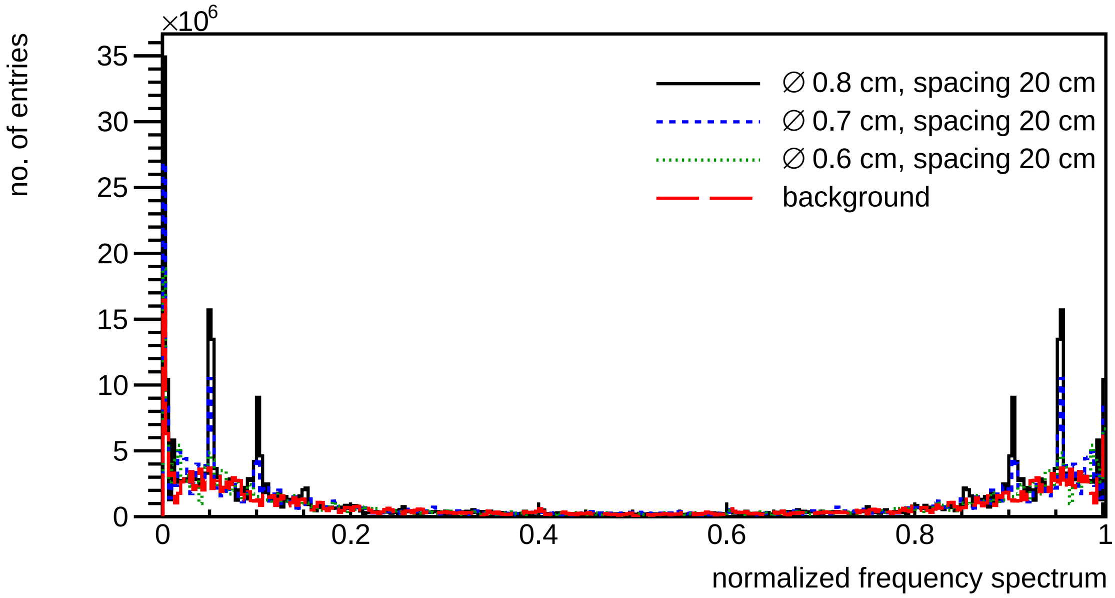

Figure 52: Normalized frequency spectra for rebars with 6, 7 or 8 mm diameter and spacing set to 20 cm. One week equivalent of data taking was used [77].

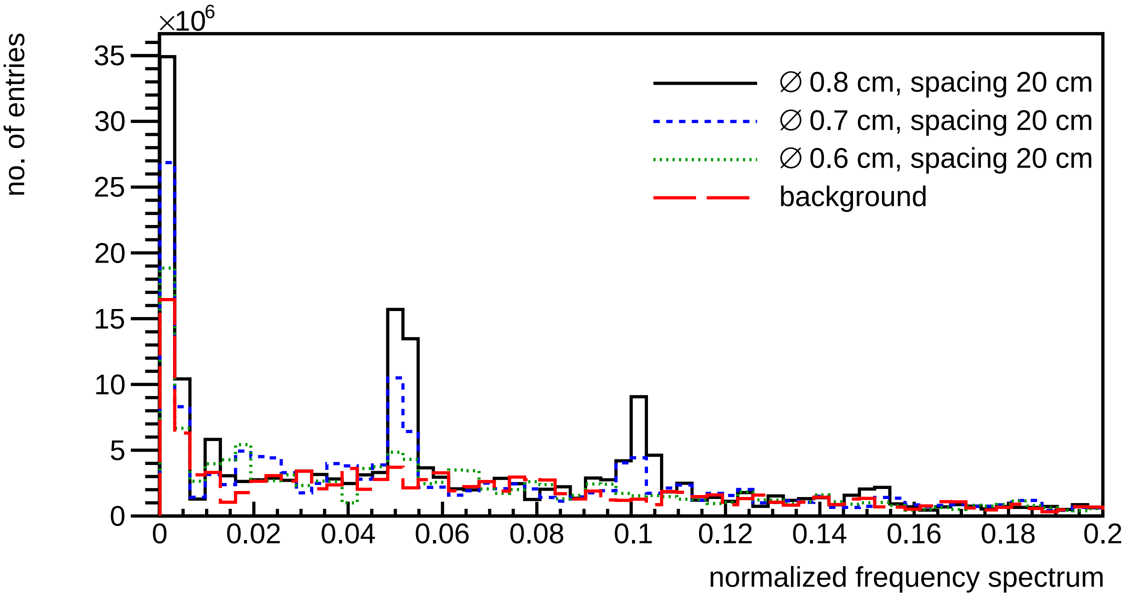

Figure 53: Zoomed version of the normalized frequency spectra for rebars with 6, 7 or 8 mm diameter and a fixed spacing of 20 cm. One week equivalent of data taking was used [77].

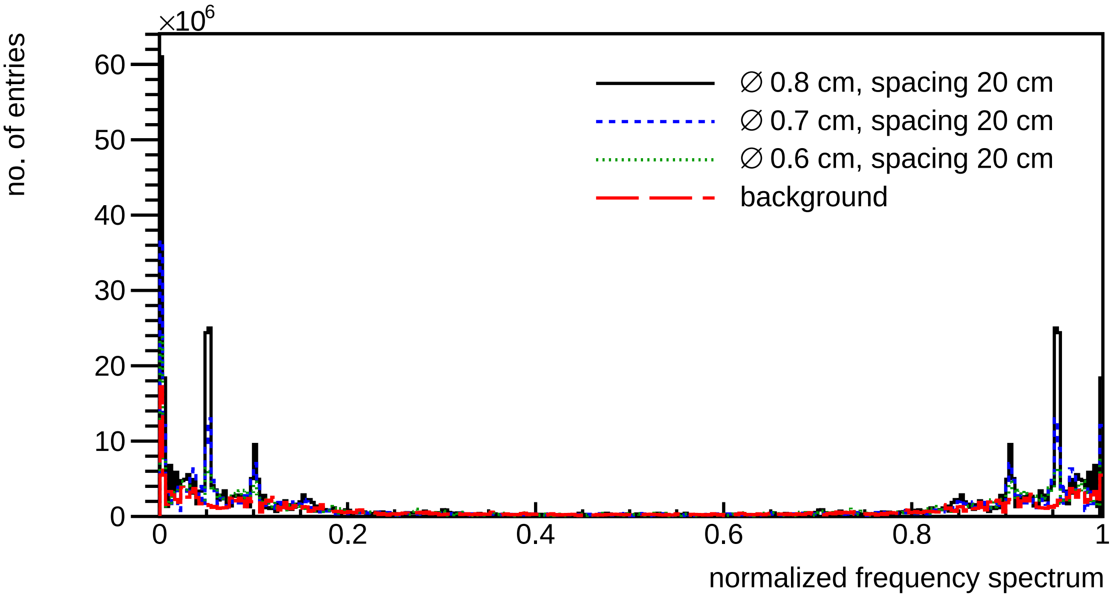

Figure 54: Normalized frequency spectra for rebars with 6, 7 or 8 mm diameter and a spacing of 20 cm. Two weeks equivalent of data taking were used [77].

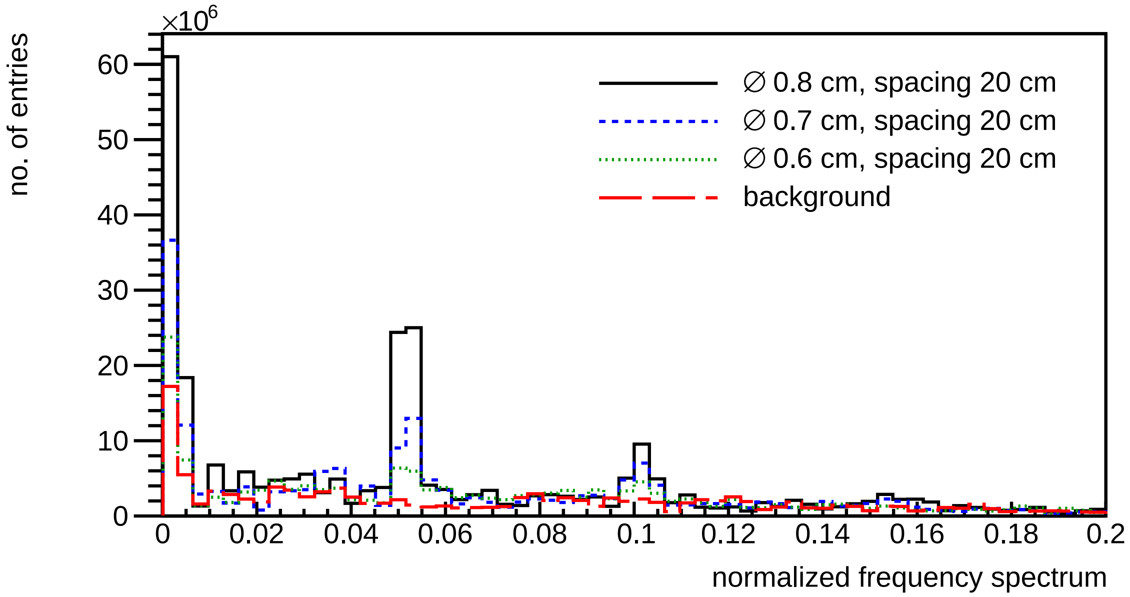

Figure 55: Zoomed version of the normalized frequency spectra for rebars of 6, 7 or 8 mm diameter and a spacing of 20 cm. Two weeks equivalent of data taking were used [77].

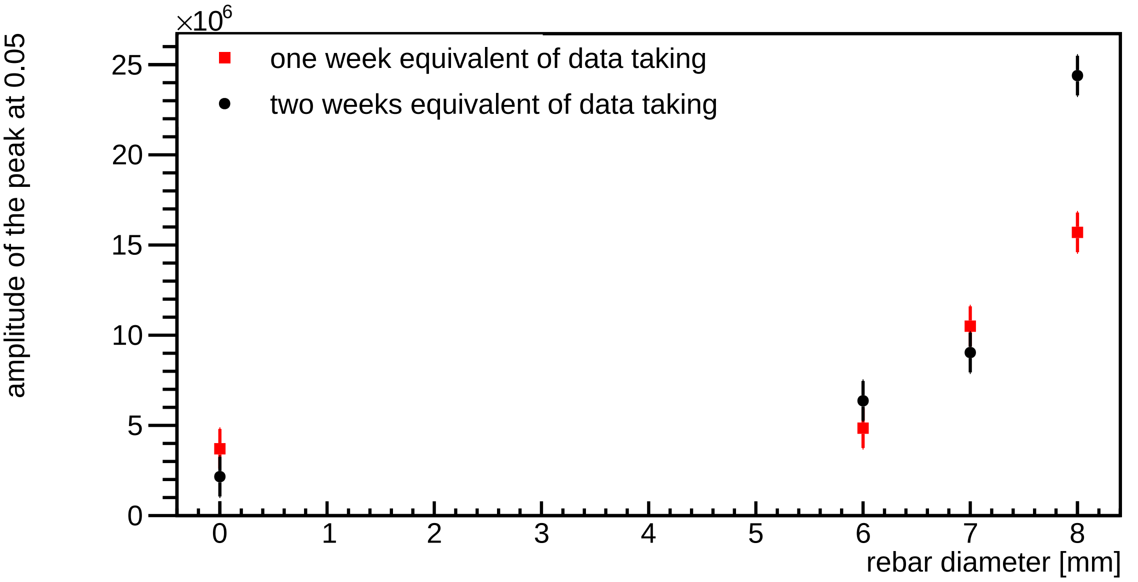

Figure 56: Amplitude of the peak at 0.05 of the normalized frequency spectra and a fixed spacing of 20 cm as a function of rebar diameter.

6.7 The effect of detector geometry and resolution on the performance of the method

Results presented so far were based on simulations of the detection system consisting of three detector layers above the scanned object and three below. The detectors were 2×2 m^2 and the simulated performance of the system was based on the system prototype built in Bristol [3] which has a position resolution of the muon hits of 450 µm. More information about the prototype system is given in a chapter 8. The performance of the algorithms described before relies on the angular resolution of the scattering. This is affected by the hit position resolution and the number of detector planes and the multiple scattering in the planes. Here the study of the effect of more detector layers and different position resolution on the system performance is presented.

6.7.1 Method performance as a function of detector resolution

The spatial resolution, R, determines the precision of the track fit and thus the angular resolution of the scattering. To understand the performance of a system with worse position resolution, the spatial resolution was increased to R=1 mm and R=1.5 mm while time of data taking was one week equivalent. A single layer of a rebar grid consisting of 8 mm diameter rebars were simulated with a spacing of 10 cm. The normalized frequency spectra are shown in figure 57. A zoomed version is shown in figure 58. With increasing spatial resolution the features of the 2D signal plots, see e.g. figure 36, are washed out and thus the amplitude of the peaks decreases. It is more clearly visible in figure 59 where the amplitude of the peak at 0.1 as a function of spatial resolution is shown. Thus when the hit position is less precise, the reinforcement grid is more difficult to be detected. However, the peak amplitude for both R=1 mm and R=1.5 mm are still significantly higher than a background signal, so the detection of the rebar grid is still possible even with a detector with a spatial resolution of 1.5 mm.

6.7.2 Method performance as a function of different number of detector layers

To improve the angular resolution, more detector layers can be used. Three detector layers were chosen as the default as this is the minimum to fit a track. The track fit is necessary to make sure that proper muon hits are used in the analysis, to reduce the background which can occur from hits due to environmental radiation and to reconstruct the scattering angle. By employing more detector layers, the precision on the reconstruction of the incoming and outgoing muon path will be improved if the scattering inside the detectors is not significant. On the other hand, more equipment leads to a cost increase, the angular acceptance will decrease and if the scattering inside the detectors is significant the angular resolution will not be improved.

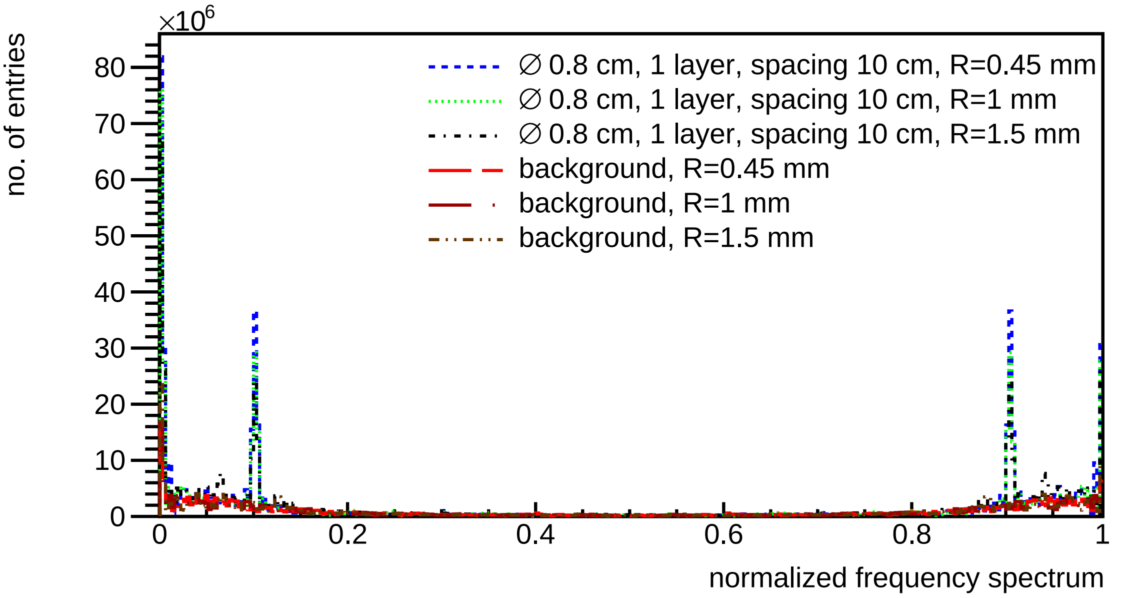

Figure 57: Normalized frequency spectra for grid made of 8 mm diameter rebars and spacing set to 10 cm, for the spatial resolution $R = 0.45$ mm, $R = 1$ mm or $R = 1.5$ mm [77].

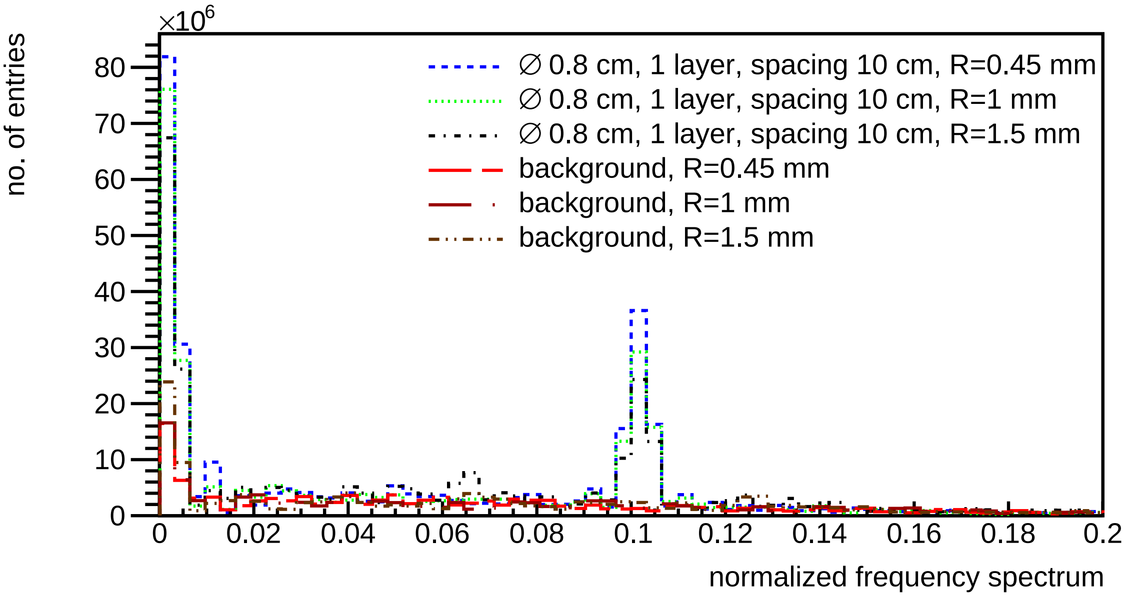

Figure 58: Zoomed version of the normalized frequency spectra for a grid made with 8 mm diameter rebars and a spacing of 10 cm, for a spatial resolution $R = 0.45$ mm, $R = 1$ mm or $R = 1.5$ mm [77].

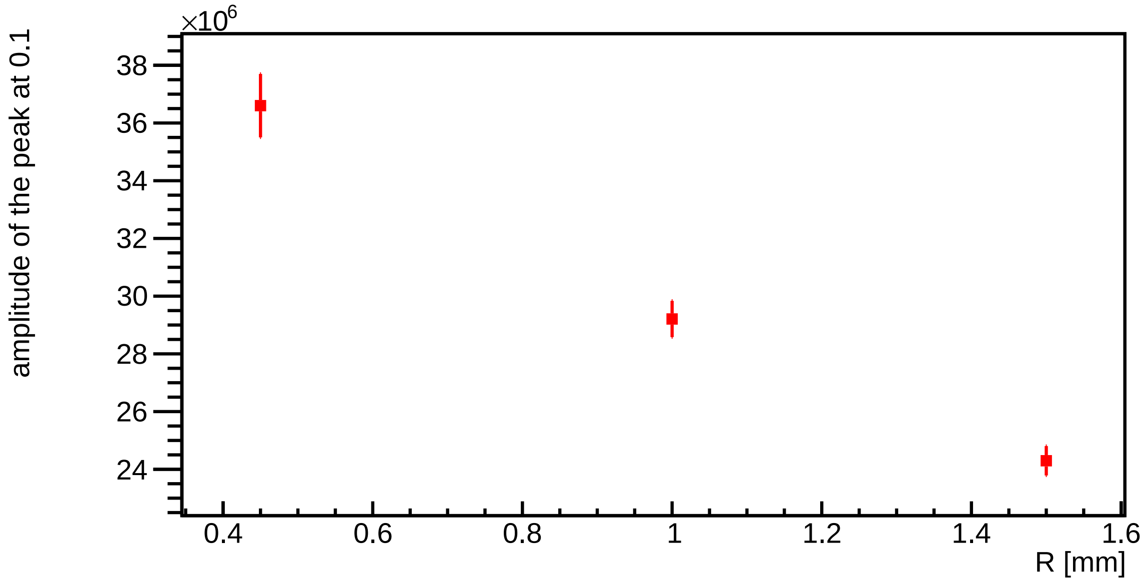

Figure 59: Amplitude of the peak at 0.1 of the normalized frequency spectra for a grid made with 8 mm diameter rebars and a spacing of 10 cm, for a spatial resolution $R = 0.45$ mm, $R = 1$ mm or $R = 1.5$ mm.

To study the effect of adding detector planes on the performance of the method, simulations with more detector layers were done using one week equivalent of data taking. The 8 mm thick rebars in a grid with 10 cm spacing were used in this test. Figure 60 shows normalized frequency spectrum (a zoomed version of this plot is shown in figure 61.) but using only tracks that resulted in a hit in each detector plane for a 3, a 4 and a 5 detector setup. The fraction of muons that fall in the acceptance of all planes is shown in figure 62. The number of planes means number of planes for the x and number of planes for the y direction up stream of the measurement volume and the same number below. Using tracks which hit all the detectors and keeping the same size of the detectors lead to lower detector acceptance. The peak in the Fourier spectra occurs in the same place for 3 and 4 layers. However, a 4 layer detector has almost three times lower peak amplitude. The amplitude for 3 detector layers is $(36.6\pm1.1)\cdot10^6$ and for 4 detector layers is $(13.1\pm0.5)\cdot10^6$. The result is worse for the 5 layer detection system. The amplitude for 5 detector layers is $(2.1\pm0.04)\cdot10^5$, where background had an amplitude of $(6.4\pm1.1)\cdot10^6$. Overall, the reduction of number of tracks is observed when using more detector layers and requiring hits in all of them and thus the amplitude also reduces. To compensate for this effect, one would need to use a larger detector but in real-life applications this solution might not the feasible.

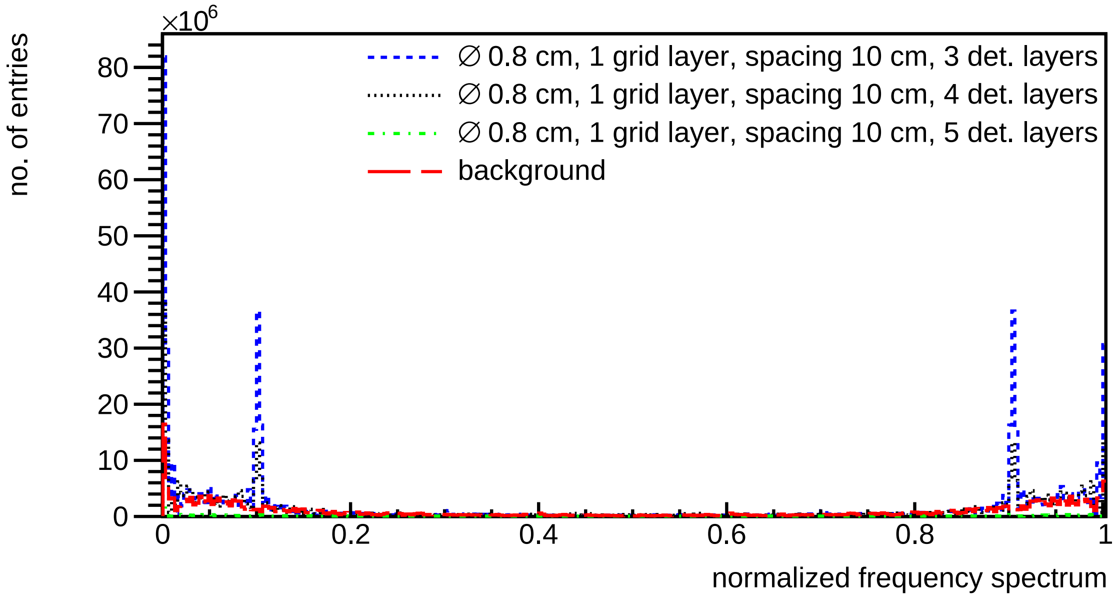

Figure 60: Normalized frequency spectra for a grid made with 8 mm diameter rebars and a spacing of 10 cm for different numbers of detector layers used for tracking with a spatial resolution per plane of 450 µm [77].

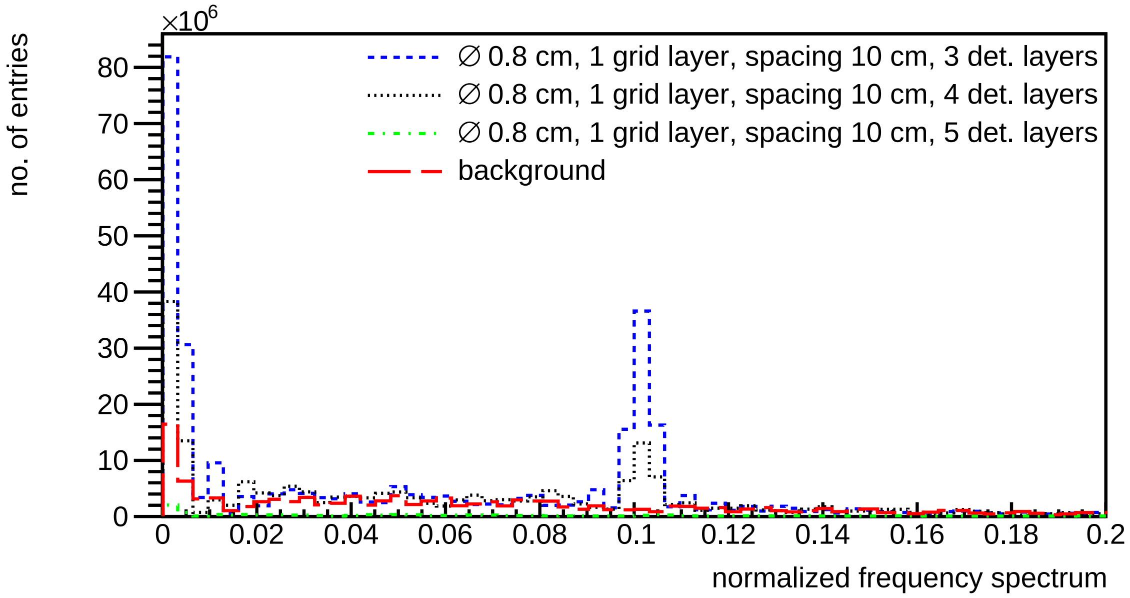

Figure 61: Zoomed version of the normalized frequency spectra for a grid made with 8 mm diameter rebars and a spacing of 10 cm for different numbers of detector layers used for tracking with a spatial resolution per plane of 450 µm [77].

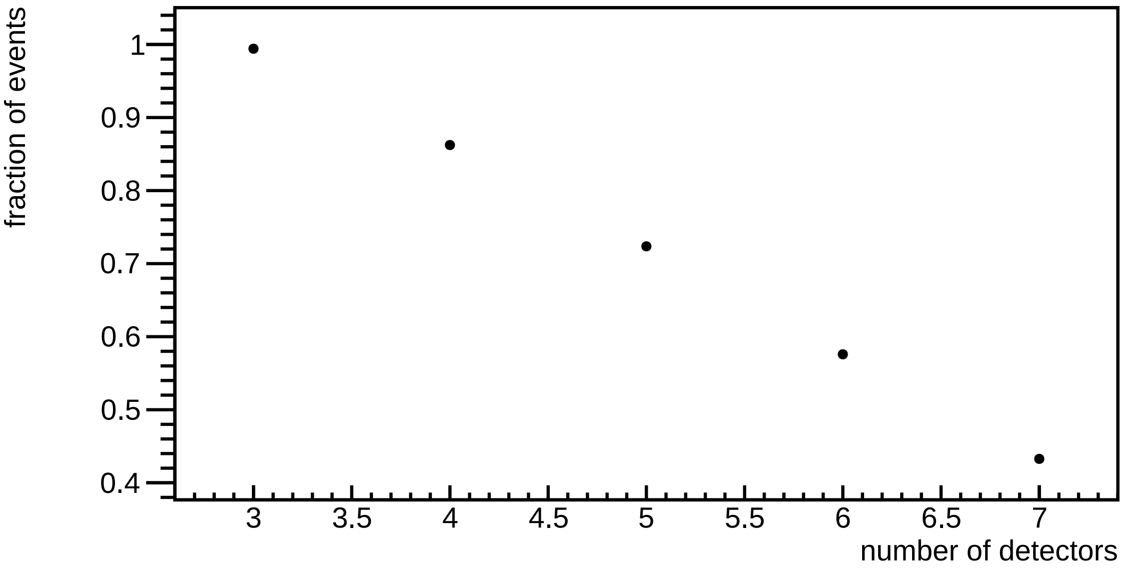

Figure 62: The fraction of muons that fall in the acceptance of the muon detection system when using 3, 4, 5, 6 or 7 detector layers.

6.8 Conclusions

Muon scattering tomography offers a solution for currently unmet needs of NDE in civil engineering. A method was presented to locate reinforcement placed in a vast concrete object. The reinforcement was simulated as a grid made of 2 m long rebars. Throughout the study, rebars with different diameters were used and the spacing was varied. The technique exploits the periodicity of the rebars in a reinforcement grid by using a modified auto-correlation method and analysing the Fourier-transformed signal. The presence of a periodic structure like a grid leads to peaks in the normalized Fourier frequency spectrum. The peaks carry information about the reinforcement mesh. Their amplitude is determined by the rebar diameters while peaks locations by the grid spacing. A grid made of rebars with a diameter of 7 mm and bigger and a spacing of 10 cm can be detected after one week equivalent of data taking. The signal for 6 mm diameter rod exceeds the background level also after a week of measurements but becomes stronger after two weeks equivalent of data taking. Longer data taking is required when the spacing is increased to 20 cm as it leads to a smaller amount of iron in the scanning area. It has been also shown that this method is suitable for the detection of the smallest rebars used in the industry using one or two weeks of data taking time for standard spacings of the grid.

7 The study of two layers of reinforcement grid in a concrete object

Often two layers of reinforcement grid are used inside the same floor. This leads to the question whether MST is able to detect both layers and determine their depths as well. This is studied in this chapter.

7.1 Simulation setup

A floor segment measuring 200 × 200 × 50 cm^3 was simulated. The number of muons used was one week equivalent. Inside the concrete block two layers of rebar grid were placed. The diameter of the rods was 8 mm and the mesh spacing was 10 cm. The first layer was placed about 7 cm into the concrete. The second grid was placed at various depths, D, exactly underneath the first layer. Depths of 0 cm, 10 cm, 20 cm, 30 cm and 40 cm were used. A schematic drawing of the setup is shown in figure 63 and images of the two layers of the reinforcement grid inside concrete block are shown in figure 64.

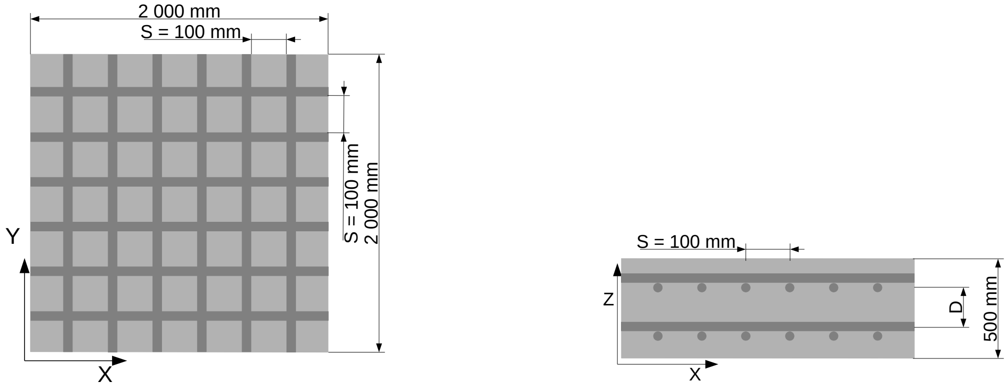

(a) Top (YX) view **(b)** Front (ZX) view

Figure 63: A sketch of the setup for the two layers scenario [80].

7.2 Development of method to localize second reinforcement grid

The auto-correlation and Fourier transform method were used, as discussed in section 6.3. However, this method will integrate the signal map also in the y-direction, while the additional layer should yield a higher signal at a certain depth. Therefore, the range of the auto-correlation calculations were changed in Y direction to a 5 cm sliding window combining 5 rows of voxels. This is illustrated in figure 65 by a red frame. After the auto-correlation was calculated for a given sliding window, the sliding window was shifted by one row in the Y direction until the whole image was scanned. The position of the sliding window will be referred as the depth of the sliding window.

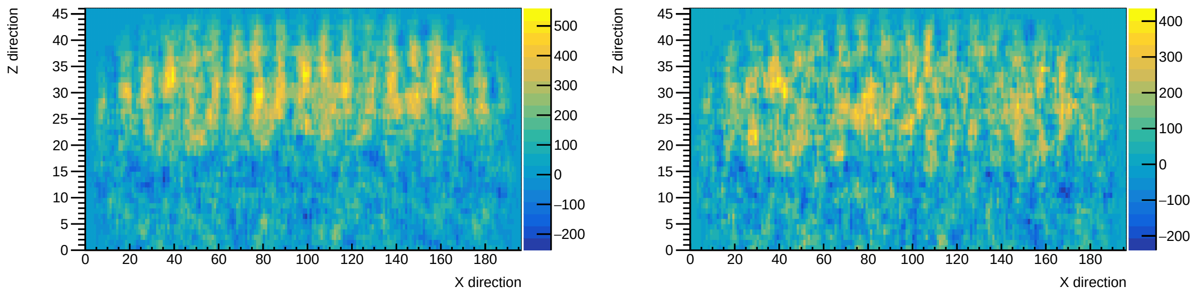

(a) The second grid was placed at D=10 cm.

(b) The second grid was placed at D=20 cm.

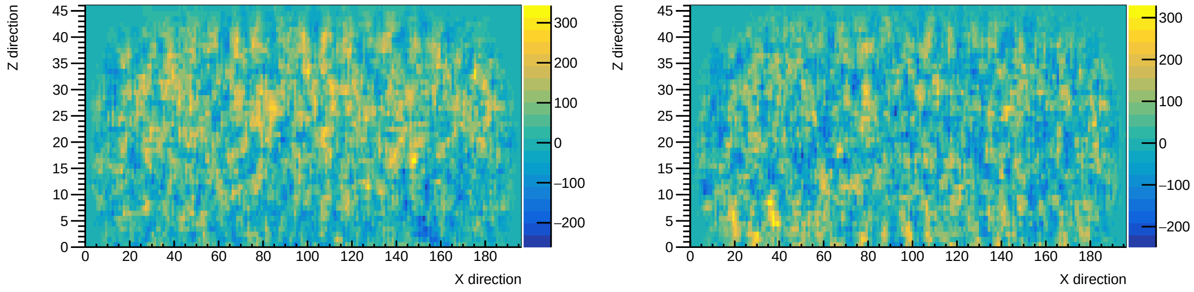

(c) The second grid was placed at D=30 cm.

(d) The second grid was placed at D=40 cm.

Figure 64: Images of the concrete block with two layers of the reinforcement grid, where the second grid is put at different depths.

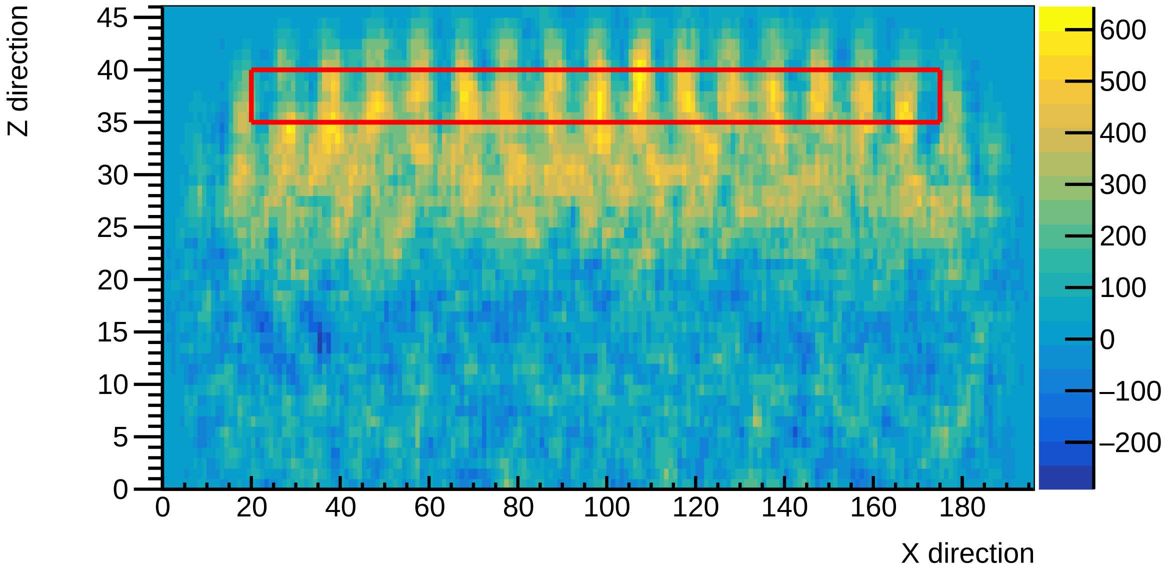

Figure 65: Signal map of the ZX projection of the geometry with a second layer at a depth of D=0 cm. The sliding window is also indicated [80].

7.3 Results of the adapted method

An example of the normalized frequency spectrum of a scenario with the separation between layers of D=20 cm and the sliding window window position in depth of 7 cm is shown in figure 66. The position of the sliding window was chosen in a way that it contains one of the grids. Hence, the auto-correlation yields a peak in the normalized Fourier spectrum at 0.1, which is in line with previous results. By moving the sliding window vertically, the position of the second grid can be found. This is shown in figure 67, where normalized frequency spectra are shown, for sliding windows at different depths. Figure 67 shows a large peak in the spectra at a depth of the sliding window at 8 and at 28 cm but not at other depths, which corresponds to the chosen geometry. Hence, the technique allows to extract the depth location of two rebar grids.

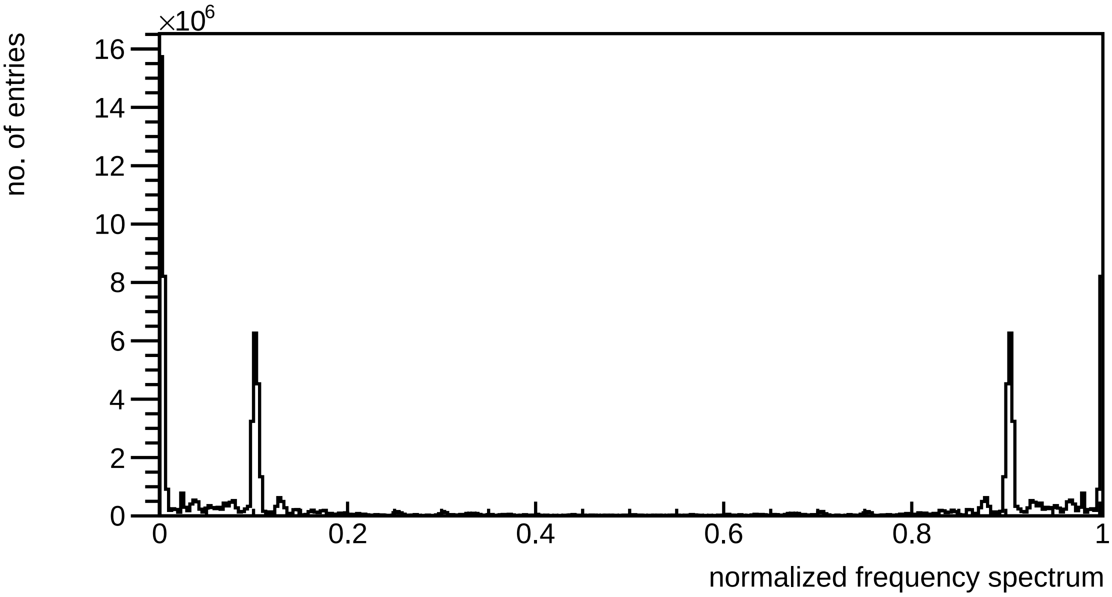

Figure 66: Normalized frequency spectrum of a scenario with two reinforcement layers with the distance between them of D=20 cm. The depth of the sliding window was 7 cm [80].

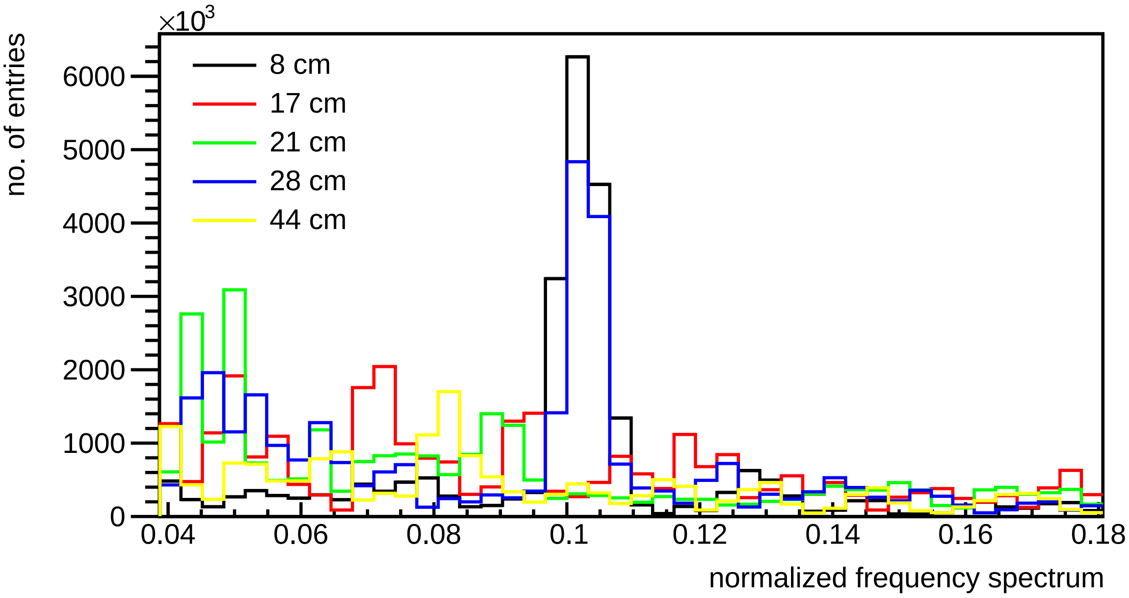

Figure 67: Normalized frequency spectra of a scenario with two reinforcement layers, where the distance between them was D=20 cm. The depth of the sliding window was varied to find the position of the second grid. The depths of the sliding window are given in the picture [80].

Figures 68 and 69 shows the amplitude of the peak at 0.1 in the normalized frequency spectra for a two layer grid system as a function of the position of the sliding window. The distance between grids was varied between D=0 and D=40 cm. To amplify the signal, the amplitude of the two bins around 0.1 were added together. Due to the Z-blurring effect, see section 5.2.4, the signal spots are extended in the Z direction. As a result the signals of the two grids merge into one if the grids are too close together. This occurs for a distance of D=0 cm and D=10 cm. When the distance between the grids is big enough, two maxima are observed in the plot. The second peak location corresponds to the location of the second rebar grid. This is shown in figure 70, where to location of the second peak (or the peak location for merged peaks) is plotted as a function of the D. The correspondence between the set and reconstructed depth is very good. Thus, the method works well.

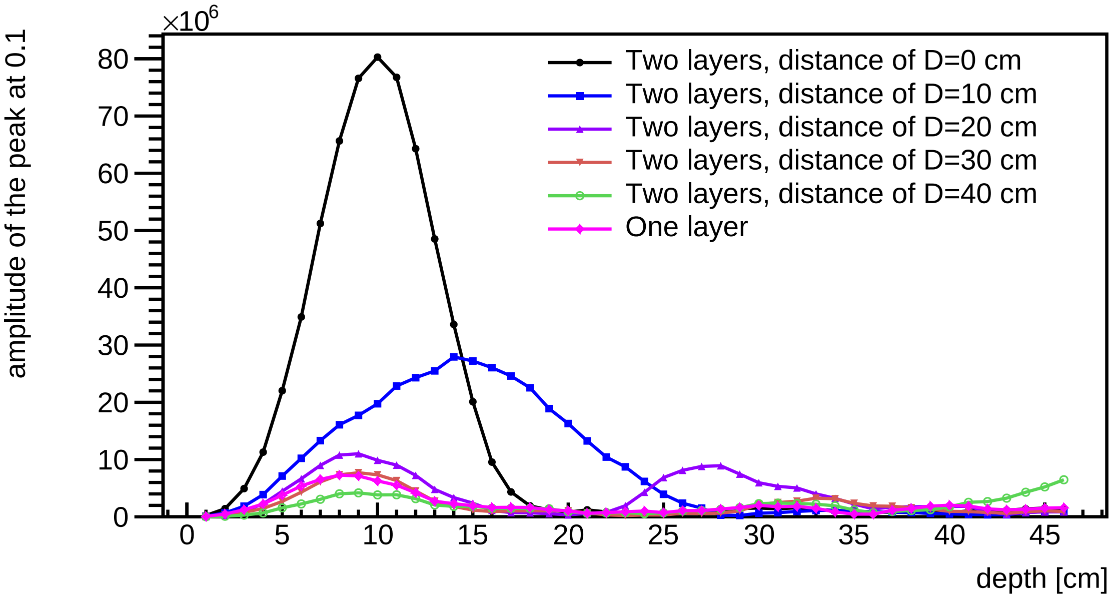

Figure 68: Amplitude of the peak at 0.1 in the normalized Fourier spectra as a function of sliding window depth for grid distances between D=0 and D=40 cm. The depth of the sliding window was varied to scan the entire block [80].

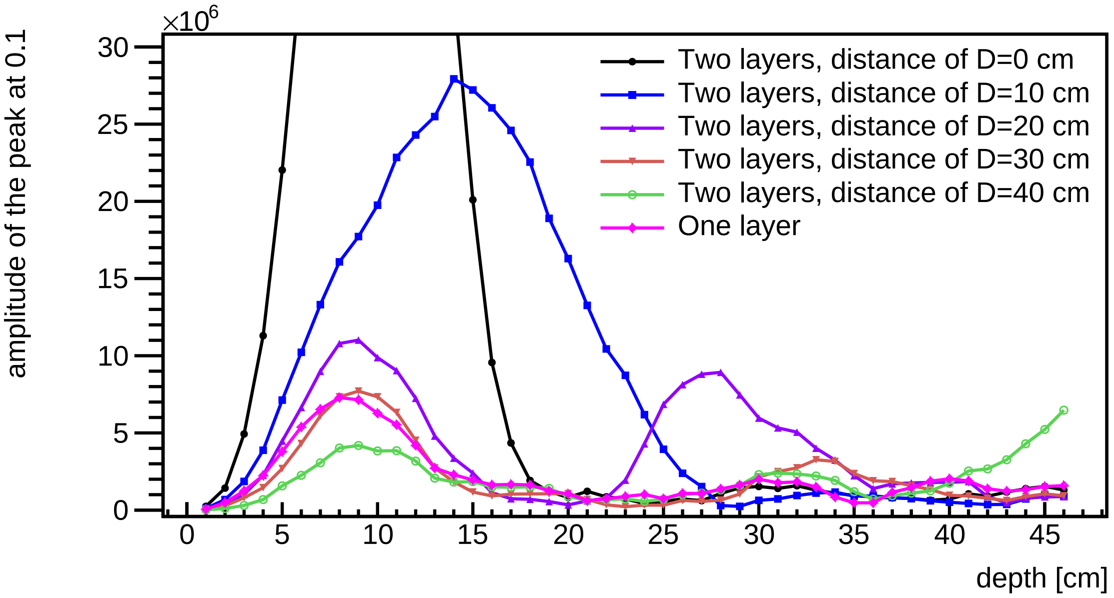

Figure 69: A zoomed version of an amplitude of the peak at 0.1 in the normalized Fourier spectra as a function of sliding window depth for grid distances between D=0 and D=40 cm. The depth of the sliding window was varied to scan the entire block [80].

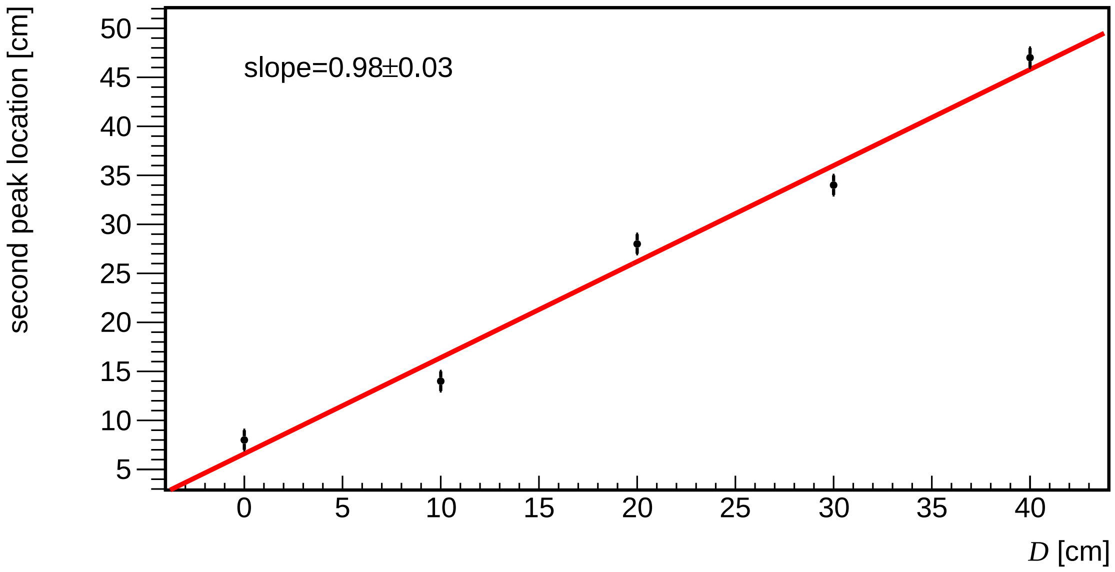

Figure 70: Reconstructed depth for the second rebar grid as a function of the distance between layers D. The line is a straight line fit [80].

7.4 Conclusions

A method is presented to locate reinforcement rebar meshes in a vast concrete structures. By using the autocorrelation method for thin strips, the depth of a second mesh can be reconstructed within a few cm precision. Further work can include the use of different mesh sizes and different diameter rebars.

8 Experimental studies

8.1 Introduction

This chapter presents the performance of a muon tracker developed with high resolution glass resistive plate chambers. It was built as a small scale prototype of a system for scanning shipping containers in search of lumps of special nuclear materials.

Strict rules for the use of greenhouse gases in scientific experiments have been established and previously used freon was not possible to employ in muon tracker. Therefore, there is a need to find a replacement. The performance of a muon tomography prototype system flushed with CO_2 is presented here. The detectors are discussed in section 8.2.1 the spacial resolution of the system in section 8.8 and track efficiency in section 8.10.

8.2 The muon tracker

The muon tomography prototype system comprises of twelve high-resolution glass resistive plate chambers - RPCs.

8.2.1 High-resolution resistive plate chambers

A resistive plate chamber essentially consists of a gas volume in a large electric field. The cosmic muons ionise the gas locally along their path. Liberated electrons and ions start moving inducing a current pulse on one or more of the pick up strips. Resistive plate chambers were used for this experiment because they have a very good detector efficiency above 95% [3], desired sub-millimetre spatial resolution and are relatively cheap. What is more, they are scalable so large area detectors can be build [76].

The RPCs used here measure 580 mm × 580 mm and are made of two sheets of float soda glass glued to a frame with a 500 mm × 500 mm window in the centre with a 2 mm gas gap. To provide mechanical support of the glass, narrow glass strips are placed inside. To obtain a surface resistivity of 500 k$\Omega/\square$ and to keep the electric field uniform inside the chambers, the outer surfaces of the glass are covered with conductive acrylic paint. A printed circuit board (PCB) carrying the pickup strips is fixed at the top of the chamber. It has 320 readout strips with a pitch of 1.5 mm which are read with MAROC3s, see section 8.3. The high voltage is insulated from the strip board with a sheet of 1 mm polyethylene terephthalate [3]. The choice for the high voltage value in gaseous detectors is a compromise between efficiency and position resolution. The higher the voltage, the more signal is generated in the gas. However, this signal is the result of secondary ionisation which does not necessarily take place in the direction of the original incoming particle. As such the signal might be higher and thus the efficiency is higher, but the charge cloud is much wider and thus the uncertainty on the hit precision is worse. These high voltages signal pulses are known as streamers [81]. An exploded sketch of a detector is shown in figure 71. Channels are connected to a power supply and operate on 4400 V or -4400 V resulting in a voltage drop of 8800 V over the detector.

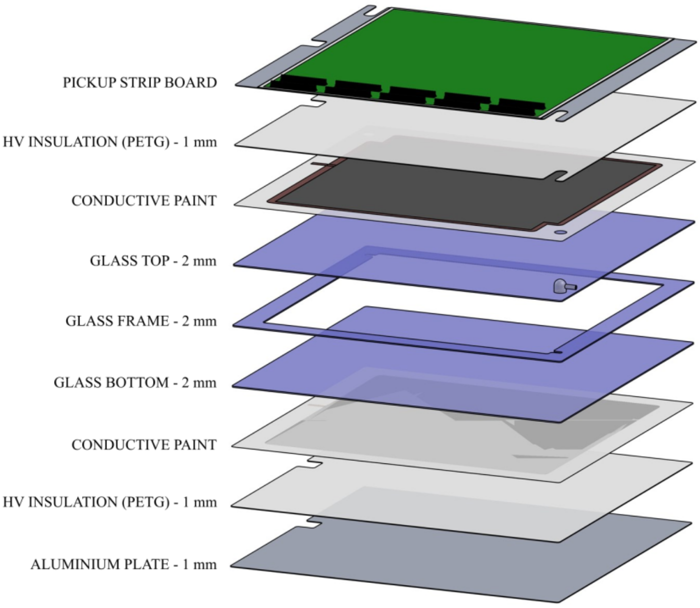

Figure 71: Exploded view of an RPC [3].

8.2.2 Gas selection

A mixture of Tetrafluoroethane R-134a and Iso-butane is typically used for RPCs detectors in main high energy physics experiments like the STAR experiment at RHIC (Relativistic Heavy Ion Collider) [82, 83], CMS [84, 85], ALICE [86] and ATLAS [87]. The Bristol system was also previously operating with a mixture of Tetrafluoroethane R-134a (95%) and Iso-butane (5%) and had a position resolution better than 500 µm and efficiency above 95% [3]. However, R-134a is considered a greenhouse gas with high impact on the environment and due to new legal regulations, the use of this mixture is not possible with current experiment. A literature review and market research to find alternative was done. Other, more environmentally friendly, gas mixtures give promising results [88, 89] with resistive plate chambers, however due to challenges with the gas supplier it was not feasible to purchase gas within the time scale acceptable for this research project.

Due to above mentioned challenges, it was decided that CO_2 will be used, which is a cheap and readily available option. One of the aims of this research was to measure and optimise the performance of the RPC system when operated with CO_2.

8.2.3 Mechanical structure

The RPCs are placed in metal cassettes and installed in a metal cabinet to ensure stability and provide an alignment reference. One cassette hosts two RPCs where one collects spatial data in the X direction, the other in the Y direction. Using the vertical positions of the detectors in the cassettes, a 3D coordinate for a muon hit is reconstructed. One RPC was 6 mm thick. The spacing between the X and Y planes was 25 mm and the spacing between the pairs was 62-65 mm. There was 554 mm of empty space for the object being scanned [3]. The interior of the cassette is shown in figure 72, which shows two RPCs and two readout boards, where one is upside down. The layers are rotated by 90 degrees with respect to each other. The cassettes are daisy chained and flushed with CO_2 at a rate of 25 ml/min. The pressure in the detectors is about 500 Pa above the atmospheric pressure.The metal cabinet with mounted cassettes is shown in figure 73a, while the naming convention of the cassettes and detectors used is in figure 73b.

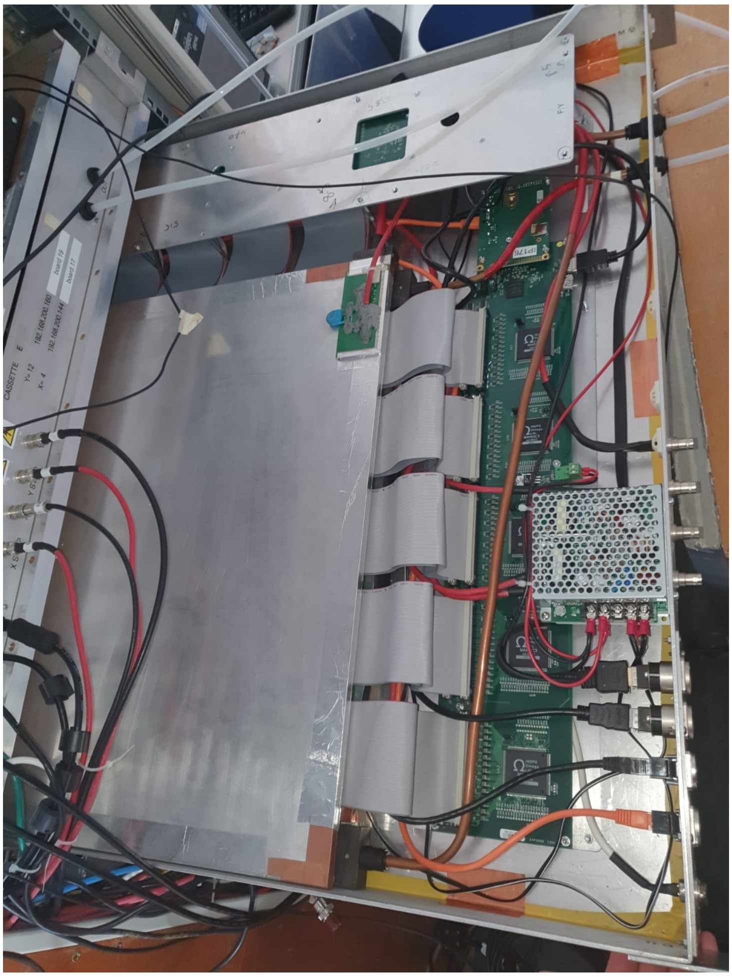

Figure 72: Interior of one cassette.

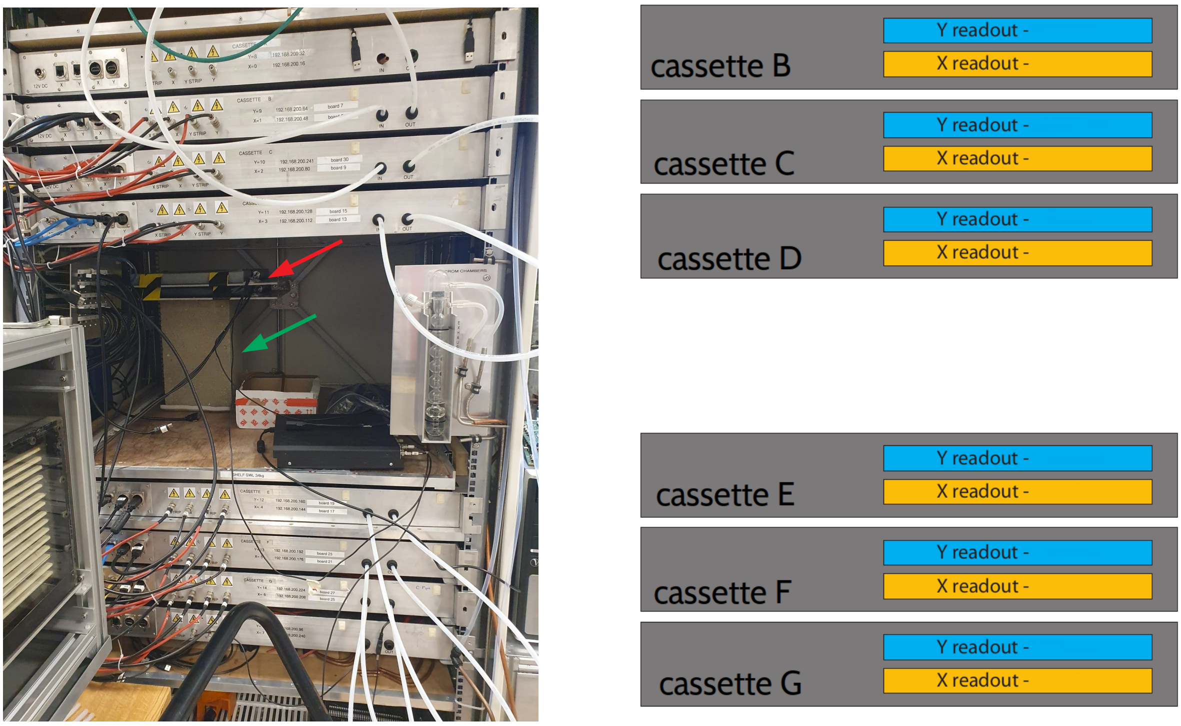

(a) **(b)**

Figure 73: The metal cabinet showing eight cassettes, four either side of the gap. In current analysis six of them are used. Inside the detector a concrete object with an unknown volume (green arrow) is place for the scan. On the concrete block the scintillators detectors (red arrow), which are part of the trigger system, are placed (a) and naming convention used in this study (b) [3].

8.3 MAROC3

The signals from the pickup strips are read out using MAROC3 chips [90]. MAROC, stands for Multi-Anode ReadOut Chip, is a 64-channel designed to read out fast negative current pulses. The MAROC3 houses preamplifiers, shapers and ADCs. The strips are AC connected to the MAROC3 input channels. The signals are continuously shaped. When a trigger is received, the signal is sampled and digitised using the in-built ADC. To read out the 320 channels, five MAROC3s are placed on a custom made readout PCB. Their readout is controlled using a field-programmable gate array (FPGA). All the front end boards in the system work with a synchronous 32 MHz clock. The MAROC3 chip generates 64 twelve-bits digital samples. The FPGA gathers the readout of each MAROC3 and stores them together with a timestamp and a trigger number in a local buffer. The buffer is read by a PC. To communicate between the FPGA and PC the IP-bus protocol [91] is used. The data acquisition software is written in LabView [92]. For the data presented in this study all the readout boards shared the same configuration parameters: the MAROC3 inputs were configured to have unitary gain and a shaping time of 110 ns. An external trigger was used, which was produced by the coincidence of the signals from two 500 mm × 500 mm scintillators placed one the tested sample, see figure 73a. When a coincidence signal is produced a readout cycle is initiated.

8.4 Data format

For each RPC, the data is represented as 359 binary words: 39 words for the header and 320 for raw ADC data for all the strips for one trigger. The header contains the IP address related to the readout board, the trigger number related to the event and the timestamps. The data structure is shown in figure 74. The data is analysed offline to find the muon hits and 3D muon tracks. An example of raw ADC data for a single RPC from an event without a muon hit as a function of a strip number is shown in figure 75. Before the hit finder analysis can be applied a few offline calculations and corrections must be performed on the data.

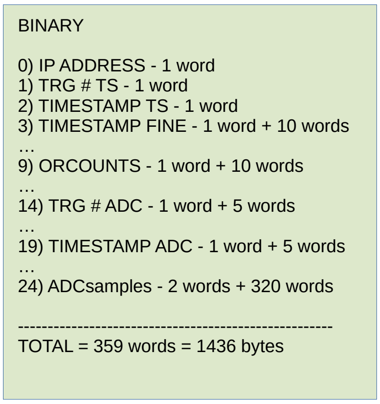
BINARY

0) IP ADDRESS - 1 word
1) TRG # TS - 1 word
2) TIMESTAMP TS - 1 word
3) TIMESTAMP FINE - 1 word + 10 words
...
9) ORCOUNTS - 1 word + 10 words
...
14) TRG # ADC - 1 word + 5 words
...
19) TIMESTAMP ADC - 1 word + 5 words
...
24) ADCsamples - 2 words + 320 words

TOTAL = 359 words = 1436 bytes

Figure 74: Data format for the RPC data.

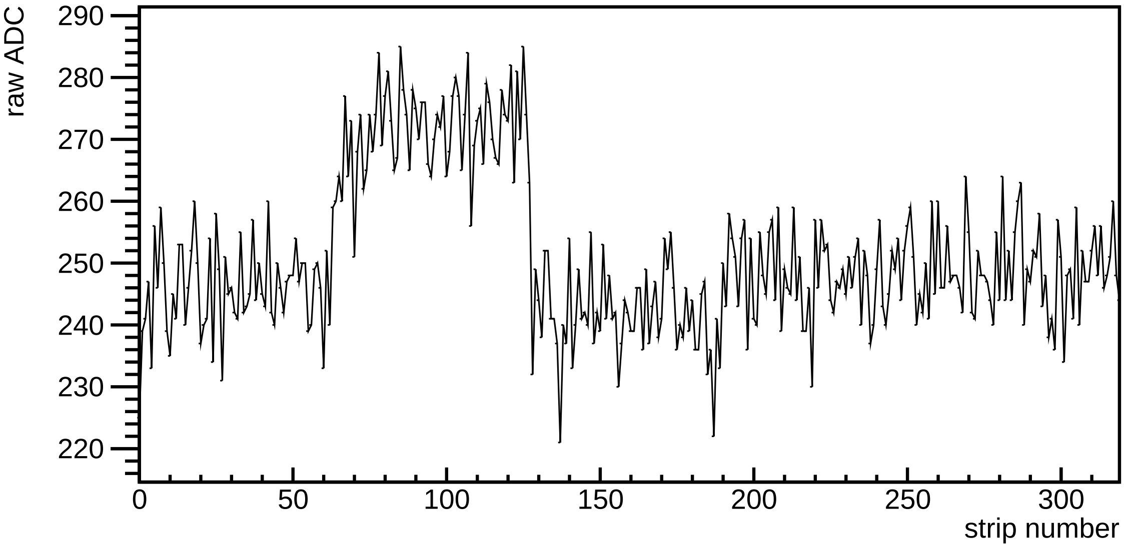

Figure 75: Raw ADC data as a function of strip number for an event without hit for one RPC.

8.5 Pedestal and noise calculation

To reconstruct the hit positions, first the induced signal on each strip needs to be reconstructed. The measured raw signal s_{raw} in a strip i consists of the actual signal, $q_{signal}(i)$, which is proportional to the charge induced by the ionising particle, the pedestal, $ped(i)$, and noise. The noise can be split into a random noise, $n_{random}(i)$, and a common mode noise component, n_{common}.

$$s_{raw}(i) = q_{signal}(i) + ped(i) + n_{random}(i) + n_{common} \tag{13}$$

In order calculate the deposited charge $q_{signal}(i)$, the pedestal, and common mode noise must be estimated and subtracted.

8.5.1 Preparing raw data for pedestal calculation

Figure 75 shows a standard event without a hit and any anomalies. However, in few events anomalies are found and these events need to be removed from the analysis or corrected. Possible anomalies are too noisy events or defective events, where a defective event is an event which contains a high ADC signal which does not come from a muon hit, but from electronic noise for example. Figure 76 shows a number of overlaying raw ADC data events for one board. Some events have much higher ADC values either due to muon hits or defective events. These kind of events must be identified and excluded from pedestal and noise calculations. A zoomed version of figure 76 is shown in figure 77 which shows that for the majority of the events pedestal fluctuates around 250 ADC. Thus, raw events with five strips with ADC values higher than 300 were excluded from pedestal and noise calculations.

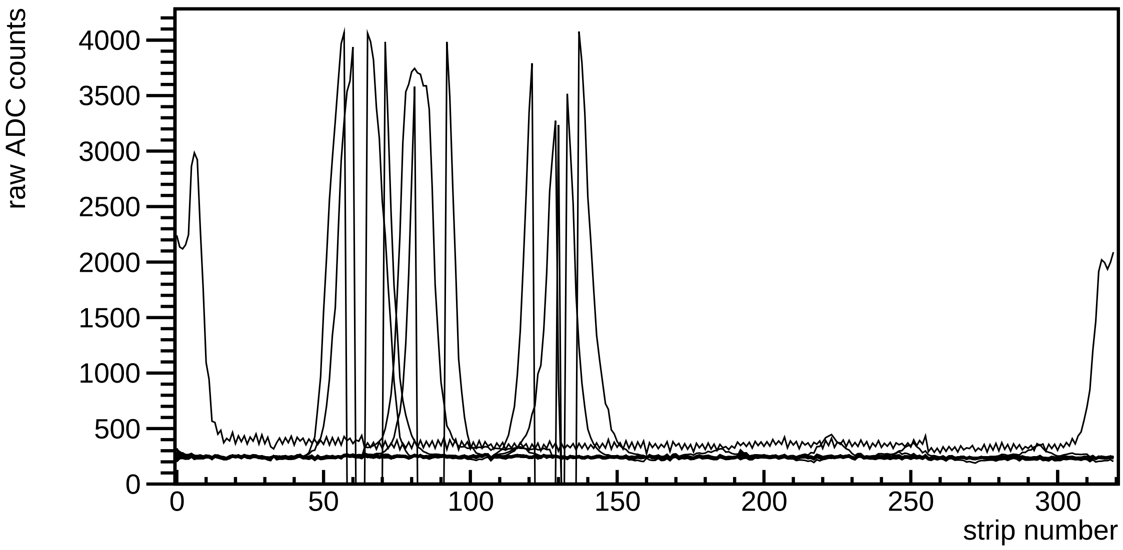

Figure 76: Overlay of several raw ADC data events as a function of strip number for one board.

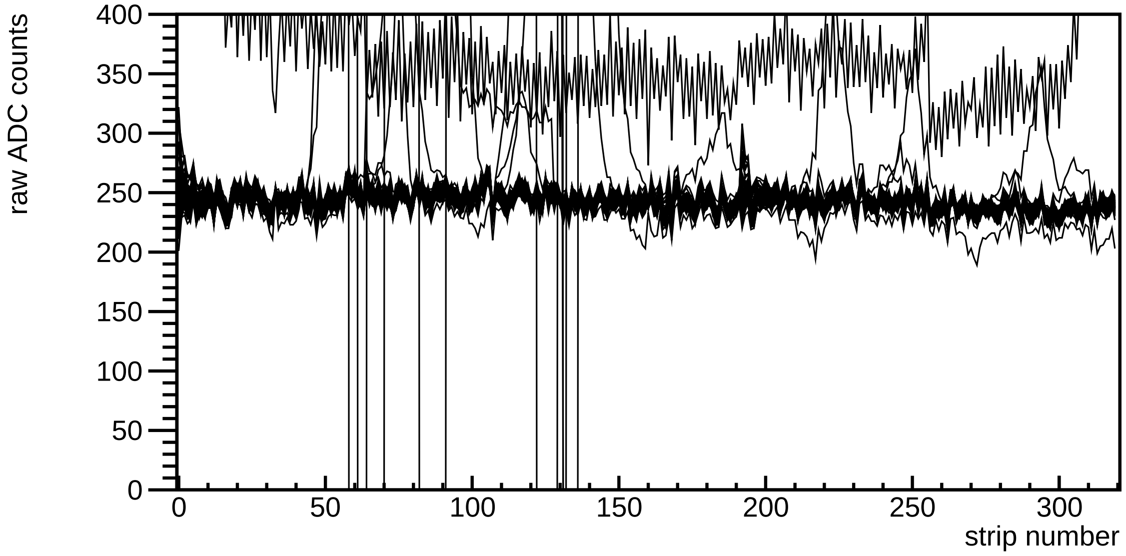

Figure 77: Zoomed version of the overlay of several raw ADC data events as a function of strip number for one board.

8.5.2 Pedestal and noise calculation

The pedestal and noise are calculated using data without hits and any anomalies. To calculate the pedestal equation 13 is used. The pedestal is computed for every data file separately to allow small drifts. To extract an initial estimate of the pedestal, the raw signal for strip i in all n events in a run is averaged. Hence,

$$\frac{1}{n}\sum_{j=0}^{n} s_{raw}(i,j) = \frac{1}{n}\sum_{j=0}^{n} q_{signal}(i,j) + \frac{1}{n}\sum_{j=0}^{n} ped(i) + \frac{1}{n}\sum_{j=0}^{n} n_{random}(i,j) + \frac{1}{n}\sum_{j=0}^{n} n_{common}(j) \quad (14)$$

Since events that do not show a hit are selected, then $q_{signal}(i,j)=0$. The noise is split into a common mode and a random noise. The random noise is Gaussian distributed around 0. Hence, when taking the arithmetic average of the raw signal for those events, the average random noise is zero. This reduces equation 14 to:

$$\frac{1}{n}\sum_{j=0}^{n} s_{raw}(i,j) = \frac{1}{n}\sum_{j=0}^{n} ped(i) + \frac{1}{n}\sum_{j=0}^{n} n_{common}(j) \quad (15)$$

The average common mode will be a constant for all channels of the MAROC3 chip and thus can be absorbed in the pedestal without losing generality. The offset will be corrected for in each event with a common mode correction.

The random noise, $\sigma(i)$ is defined for every strip as the standard deviation of the raw signal distribution after common mode correction. An initial random noise, $\sigma_I(i)$, is estimated including common mode.

To improve the pedestal estimate by eliminating further outliers, for example from small signal hits, the pedestal is recalculated only accepting events where the signal is not too far away from the initial estimate. This window is chosen as closer than ± $3\sigma_I(i)$ from the mean. The pedestal of one of the boards is shown in figure 78. Pedestals and initial noise values for all boards are shown in figures 79 and 80. Pedestal values are around 250 ADC, where the noise is around 3 ADC for most of the strips. This still includes the common mode. At the end of an RPC and at the edge of each MAROC the noise can be higher. Once the pedestal is calculated it is subtracted from raw ADC values, see figure 81.

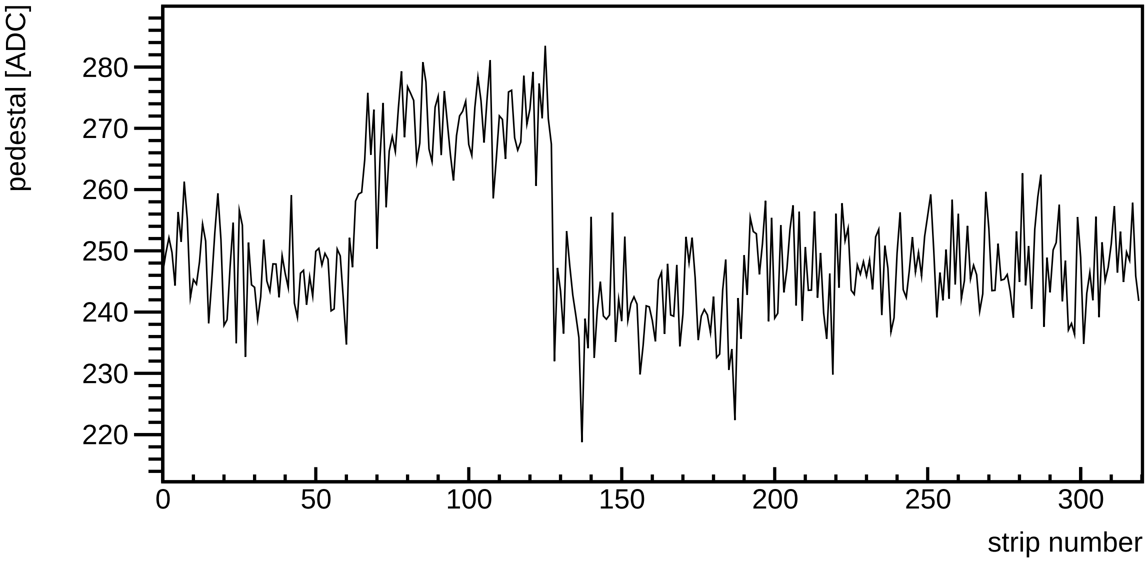

Figure 78: Pedestal as a function of strip number for board BY.

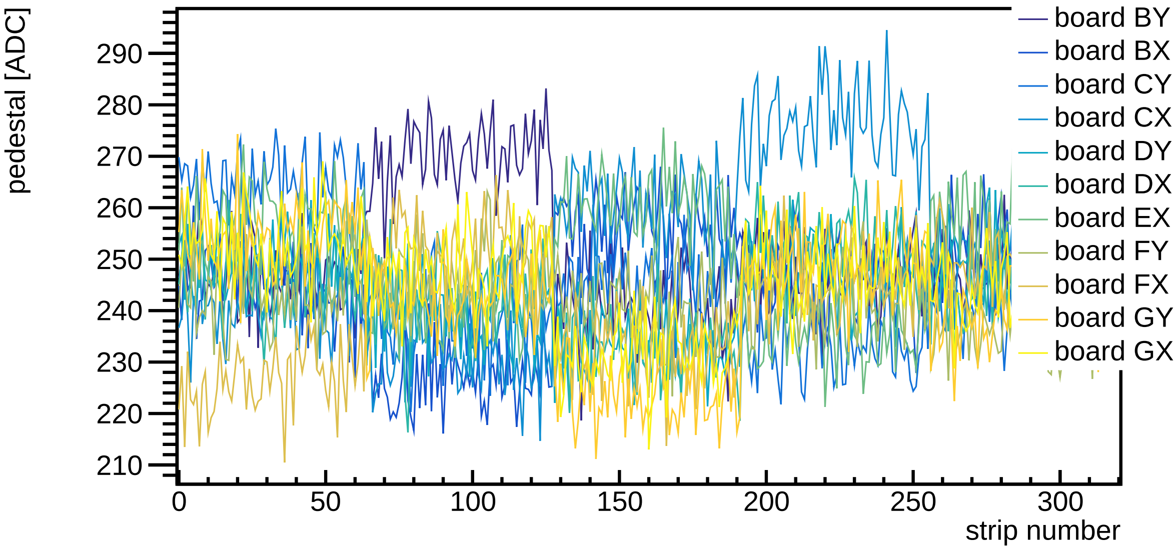

Figure 79: Pedestal as a function of strip number for all boards.

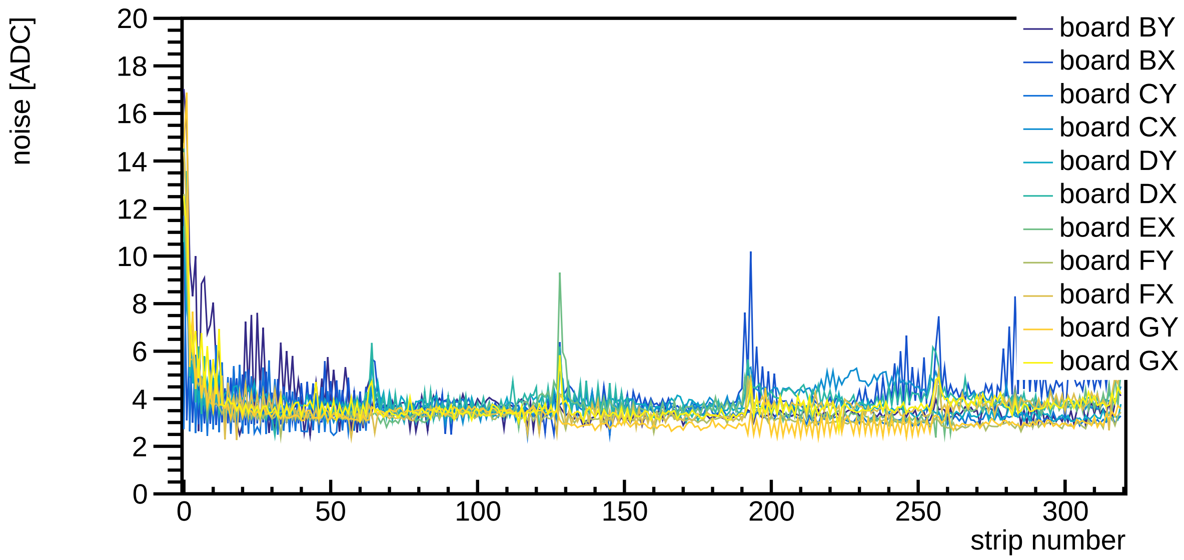

Figure 80: Noise as a function of strip number for all boards.

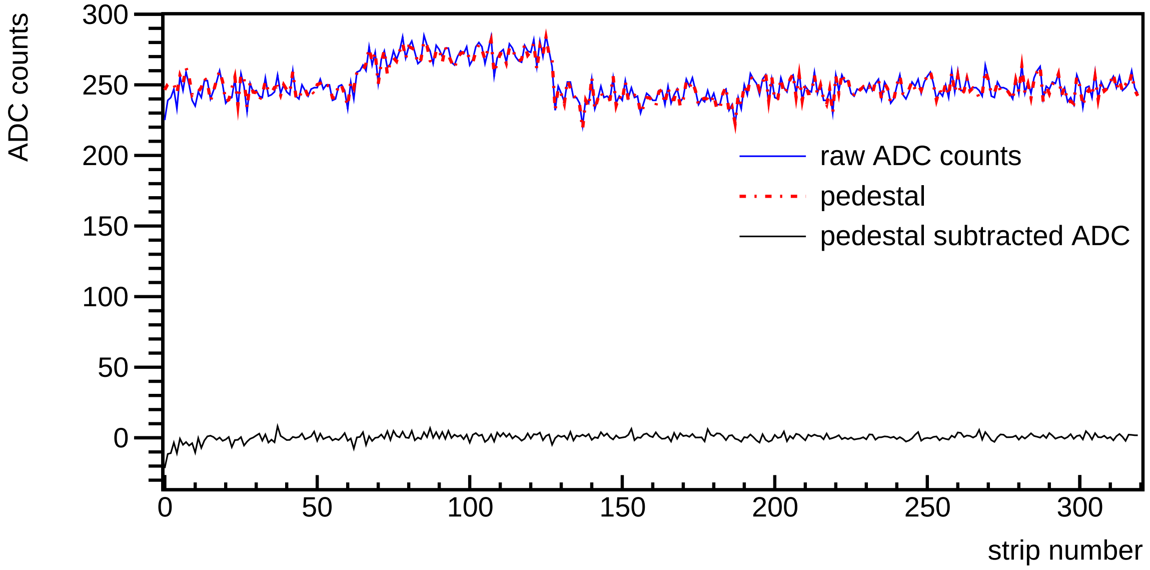

Figure 81: Raw ADC counts, pedestal and pedestal subtracted signal as a function of strip number.

8.5.3 Common mode noise correction

Common mode is a correlated noise between strips. To investigate whether common mode is significant for detectors used, correlations between strips were studied. Figure 82 shows three typical correlation plots for three different strips for board BY.

Raw ADC data for strip 175, 140 and 182 versus raw ADC data for strip 170 were plotted, where all strips belong to one MAROC3. If there is no correlation, a 2-dimensional Gaussian distributions with the standard deviations equal to the individual strip noise are

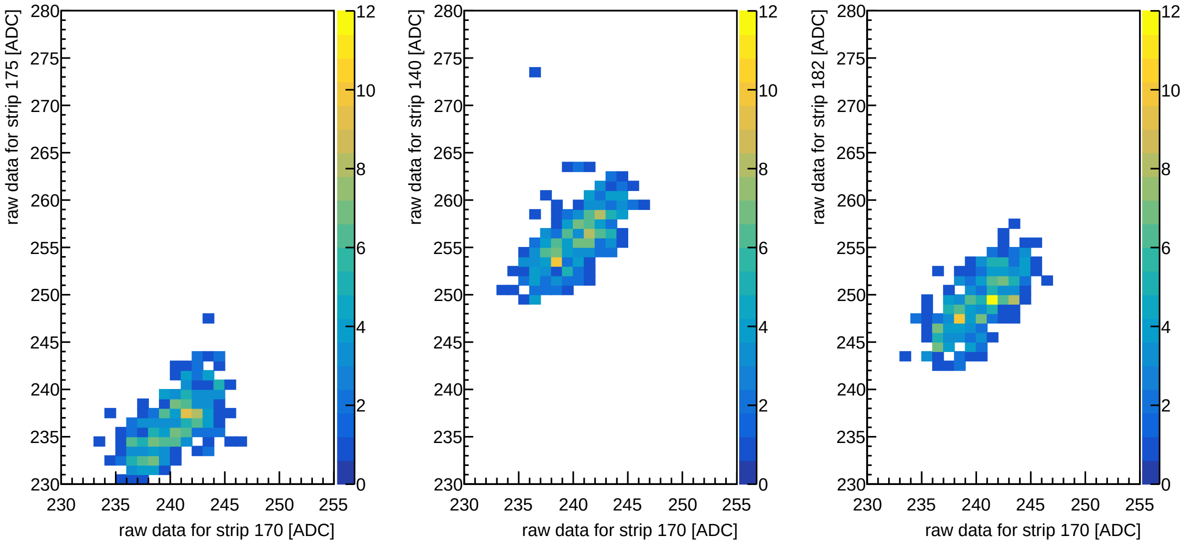

Figure 82: Three examples of strip signal correlations. Linear correlation indicates that there is a significant common mode.

expected. The result in figure 82 strongly suggests that the common mode is an event by event offset for each MAROC3, as the signals of the strips display a linear correlation.

To improve the random noise estimation, common mode must be estimated and subtracted. Therefore, the common mode is calculated for each MAROC3 as the average signal over all strips in an event excluding strips with hits. The common mode distribution for board DX is shown in figure 83. There is no expected shape of the common mode distribution. For board DX it oscillates around 0. The small peak at 0 follows from the fact that it is not always possible to calculate common mode for a given MAROC3 because in some rare events all of the strips were marked as containing hit. In these situations common mode is set to 0. An event after pedestal and common mode correction is shown in figure 84.

8.5.4 Improved random noise estimate

After the pedestal and a common mode correction are applied, the estimate of the random noise is improved by repeating the calculation from section 8.5.2 now including the common mode correction. An example of the random noise before and after common mode correction is shown in figure 85. The average noise is lower by about 1.5 ADC, see figure 86, where the difference between noise before and after common mode correction is shown. Noise as a function of a strip number after common mode correction for all detectors is shown in figure 87.

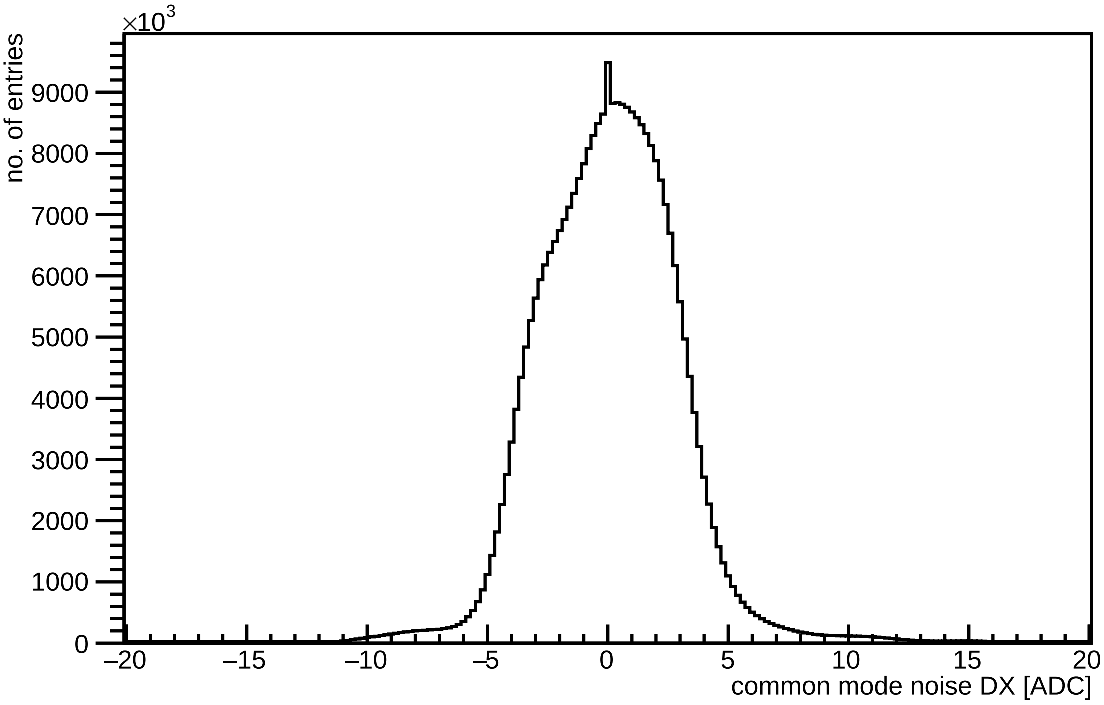

Figure 83: Distribution of the common mode noise for board DX.

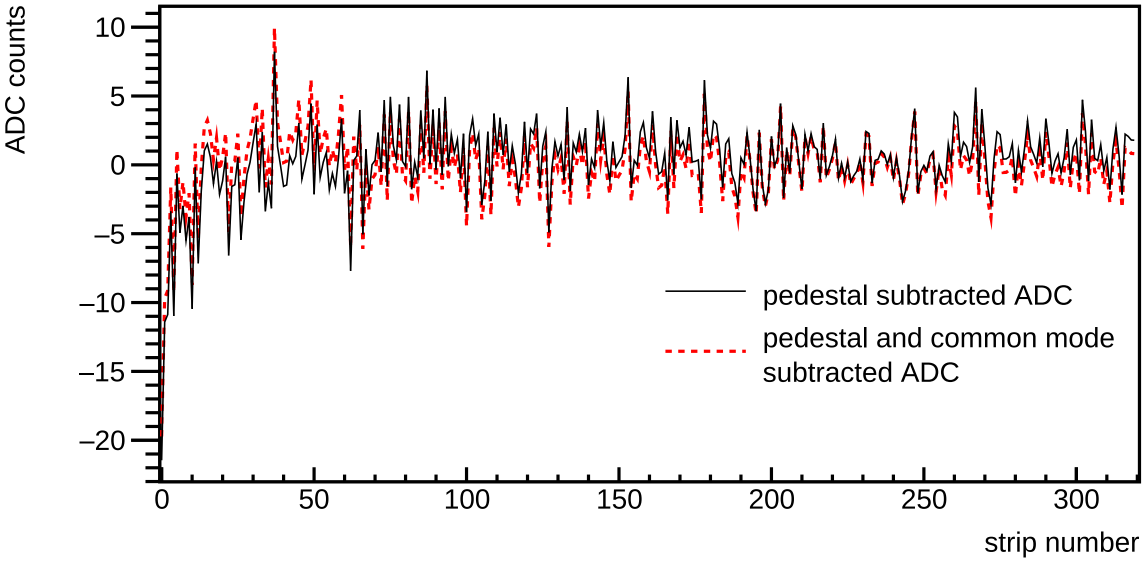

Figure 84: Strip signals as a function of strip number after pedestal subtraction and pedestal subtraction and common mode noise correction.

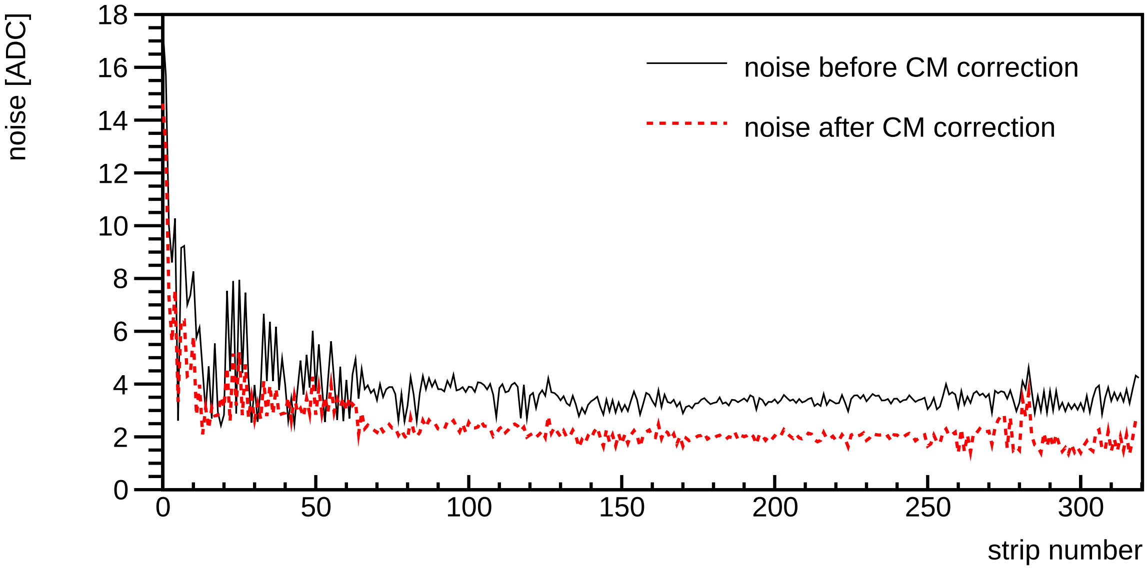

Figure 85: Noise as a function of strip number for board BY before and after common mode (CM) correction.

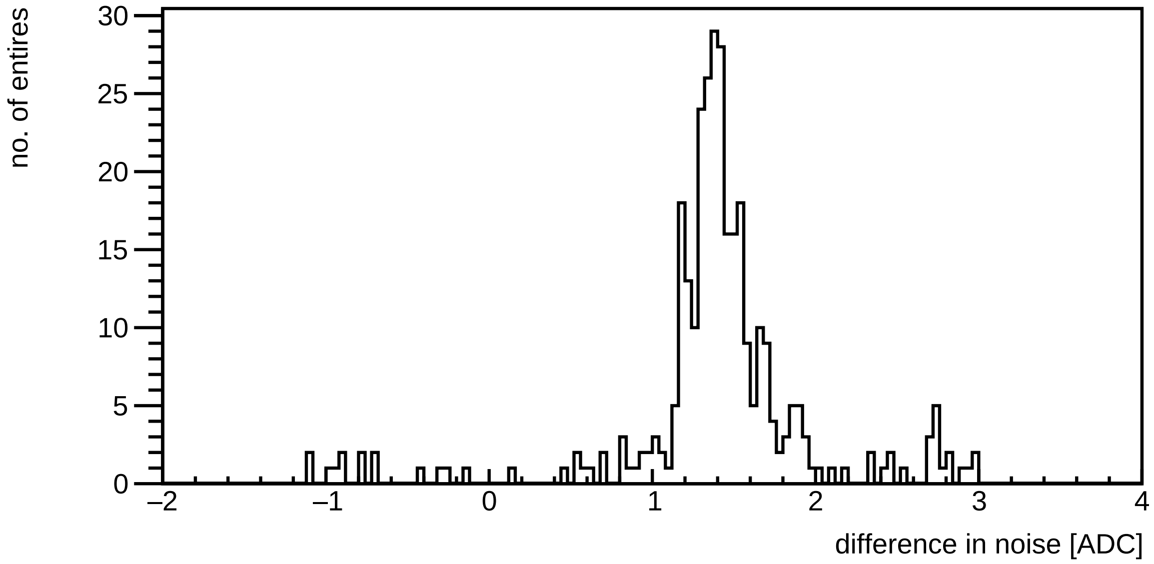

Figure 86: A distribution of a difference in noise before and after common mode correction for board BY.

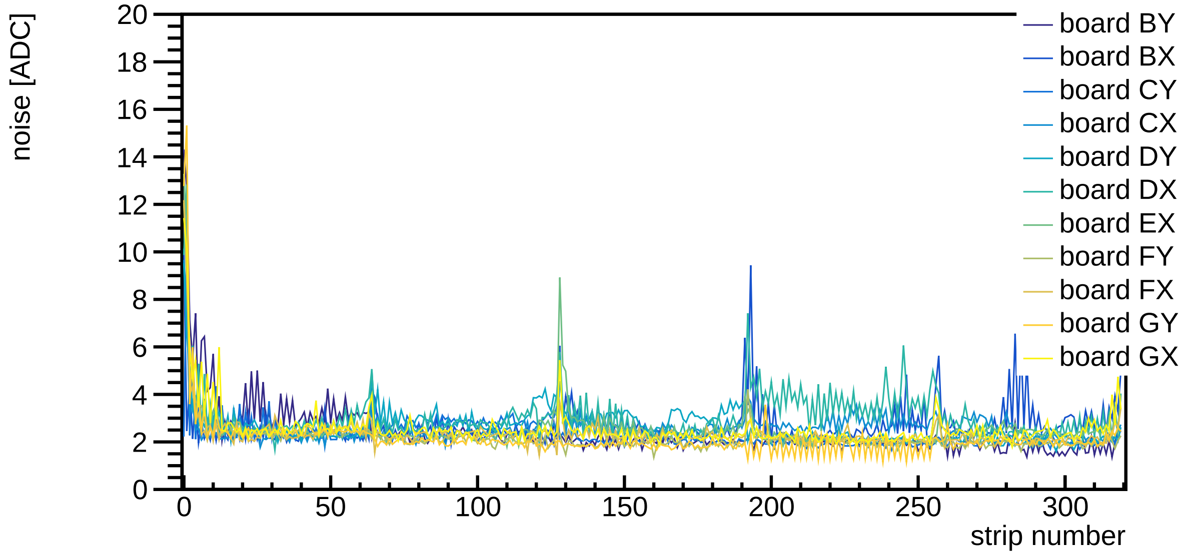

Figure 87: Noise as a function of strip number for all boards after common mode correction.

8.6 Hit finding

After pedestal and common mode correction, hits can be looked for. Firstly a hit cluster is found. The hit cluster is a set of strips which signals most likely originate from a charged particle. To start with, a seed strip is searched for: the seed strip is a strip with a signal-to-noise ratio (s/n) larger than 5. Next, neighbouring strips are included in the cluster, going outwards, as long as their s/n is larger than $2\sigma(i)$. The last strips meeting that condition are referred to as edge strips. A sketch of a cluster of a hit is shown in figure 88. Next, the hit position is calculated using mean of the Gaussian fit to data in strips in a cluster. An example of a raw event that contains a hit is shown in figure 89a. The same event after pedestal and common mode correction is shown in figure 89b.

8.6.1 Hit characteristics

Examples for hit position on board DX are shown in figure 90. Hits are not evenly distributed along the detector boards due to limited acceptance of the scintillators. Since they are smaller than the detectors, the trigger area is clearly visible as triangular-in-shape distribution. The chambers need mechanical support inside to keep them in place, thus there are narrow strips of glass put inside. Where these are, there is no gas and thus no signal. This results in seven areas with no hits.

Typical hit sizes are shown in figure 91. Most of the strips are no more than 40 strips wide and the most probable value is 14. Seed signal distribution is shown in figure 92 and signal to noise of the hit seed is shown in figure 93. The most probable value for the seed signal is 16 ADC. The plot also shows that there are many seeds with a very large signal.

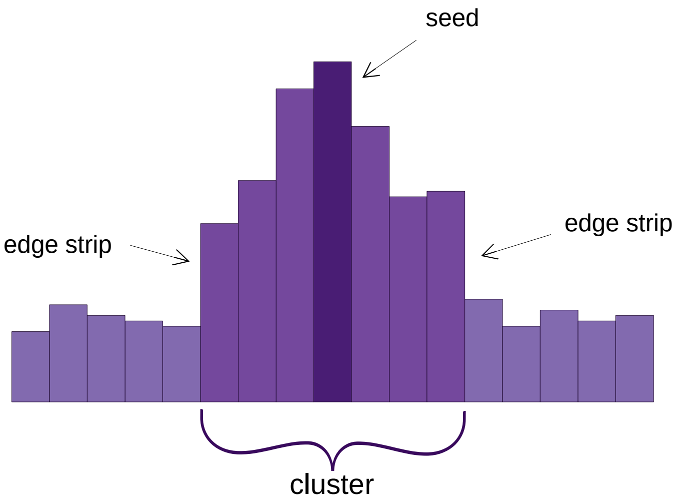

Figure 88: A sketch of a hit cluster.

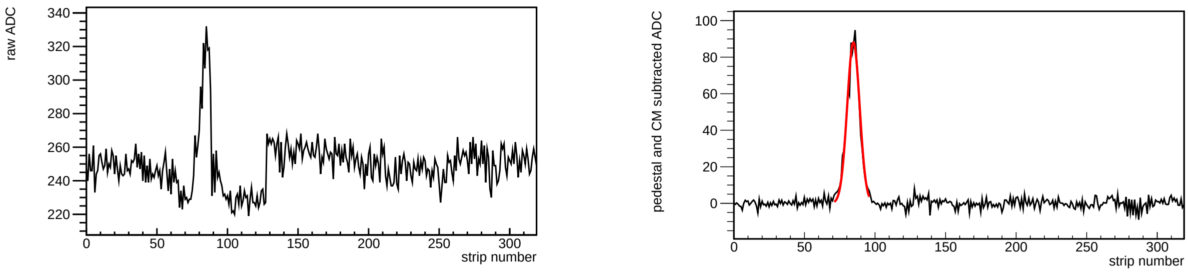

(a) **(b)**

Figure 89: An event that includes a hit before pedestal and common mode correction (left) and the same event after pedestal and common mode correction with a Gaussian fit to the strips with a hit (right).

This is due to streamers where much more charge is liberated, see chapter 8.2.1. The most probable value of the signal to noise is 5. Figure 94 shows total hit signal. For most of the hits it does not exceed 500 ADC.

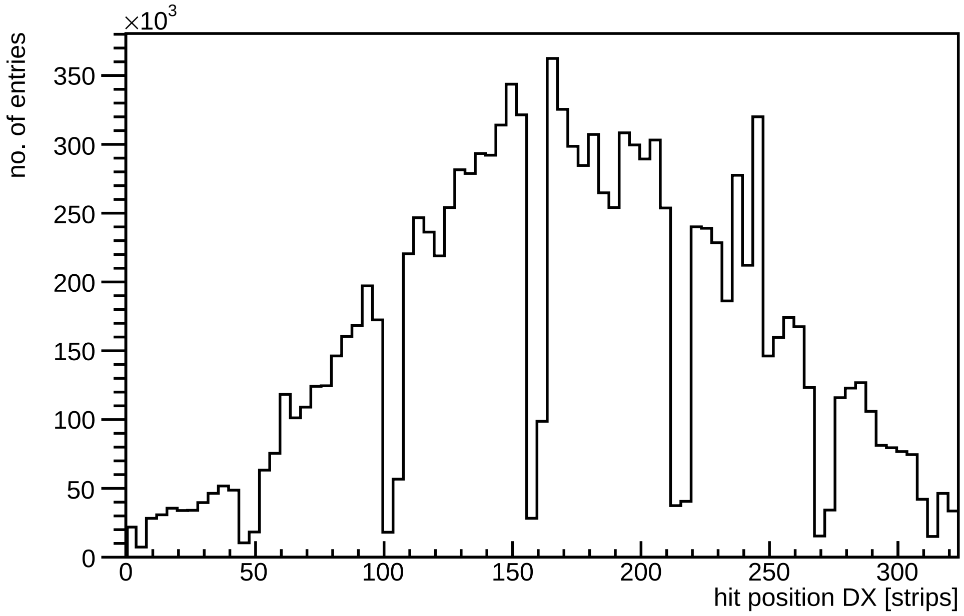

Figure 90: A distribution of hit position in board DX. An acceptance effect of the scintillator detectors if visible here. Since they are smaller than gas detectors and were placed on the top of them, there is an excess of the hits registered in the centre of gas detectors compared to its sides.

8.6.2 Dead strips within a cluster

A complication in the cluster finding is that some strips are dead or do not respond correctly. With the cluster finding algorithm as described above, two clusters are found instead of the one. An example of such behaviour is shown in figure 95a. To overcome this challenge additional checks are performed. Firstly, it is checked if the strip $i + 2$, which is two strips away from the original edge strip i, has a signal larger than $3\sigma(i)$. This higher neighbouring strip signal cut was required to enhance the probability that it is not a statistical fluctuation. If the condition is met, it means that there is a dead strip. The signal of the dead strip is calculated as the average of the strip on the left and strip on the right of the dead strip. An example of a hit with a dead channel is shown in figure 95a, while figure 95b presents the hit after the correction.

8.6.3 Inverted hit correction

In very few events, an inverted hit occurs. The reason is unknown, but hits like this can still be used in the analysis. Two events with inverted hits are shown in figure 96a. To find hits like this an inverted cluster with negative ADC values is looked for. When sufficiently low signal values (lower than -5$\sigma(i)$ for a seed and lower than -4$\sigma(i)$ for neighbouring

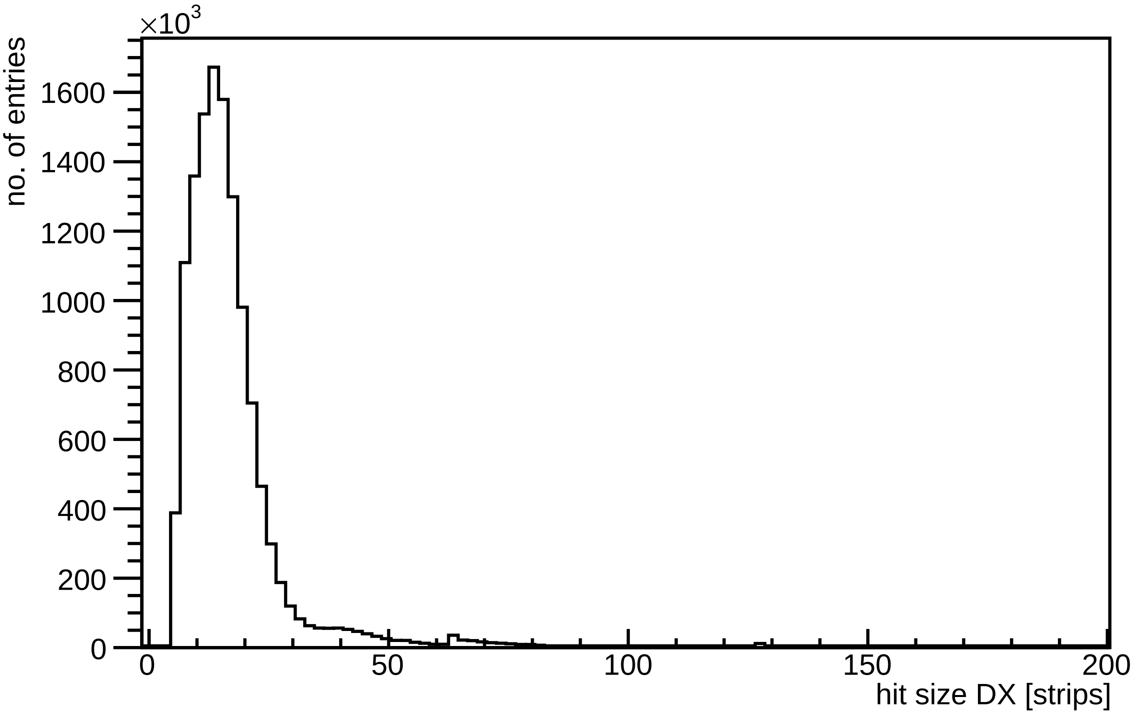

Figure 91: A distribution of the hit size in board DX.

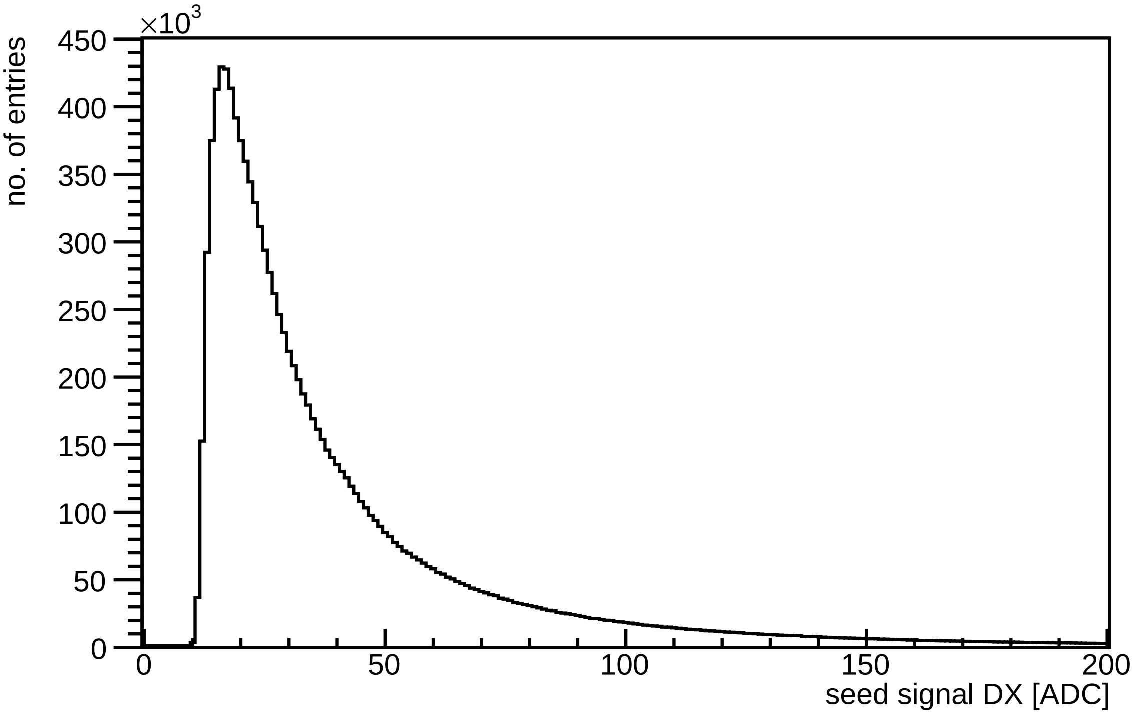

Figure 92: A distribution of the seed signal in board DX.

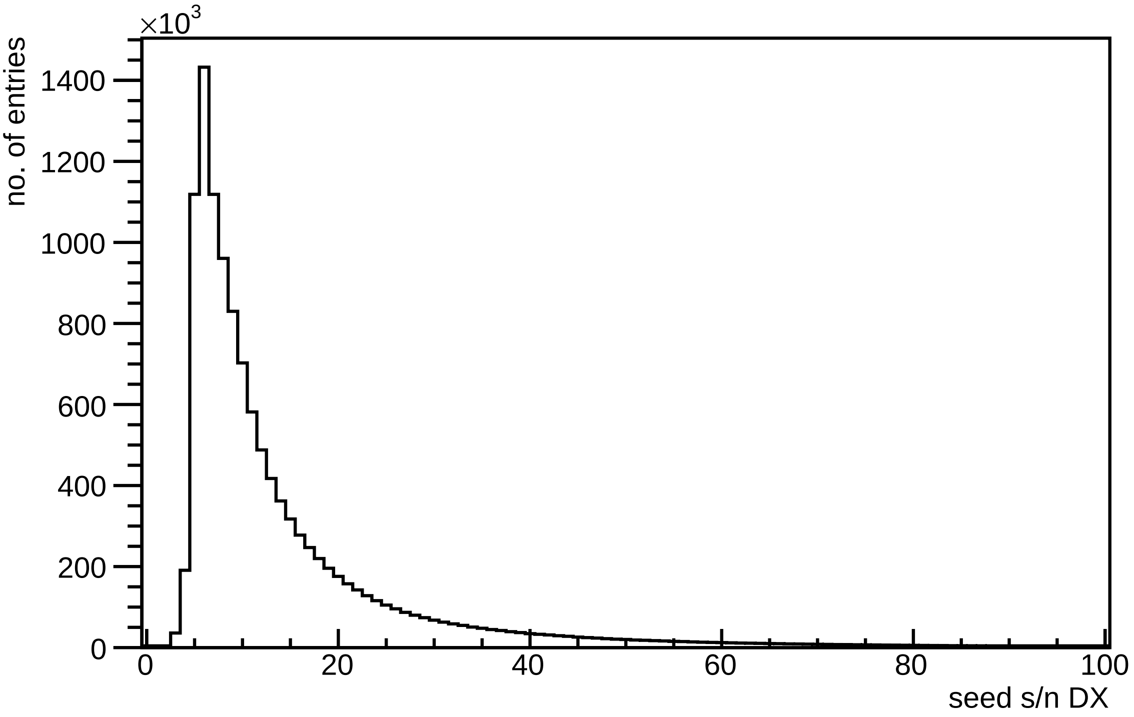

Figure 93: A distribution of the seed signal-to-noise ratio s/n in board DX.

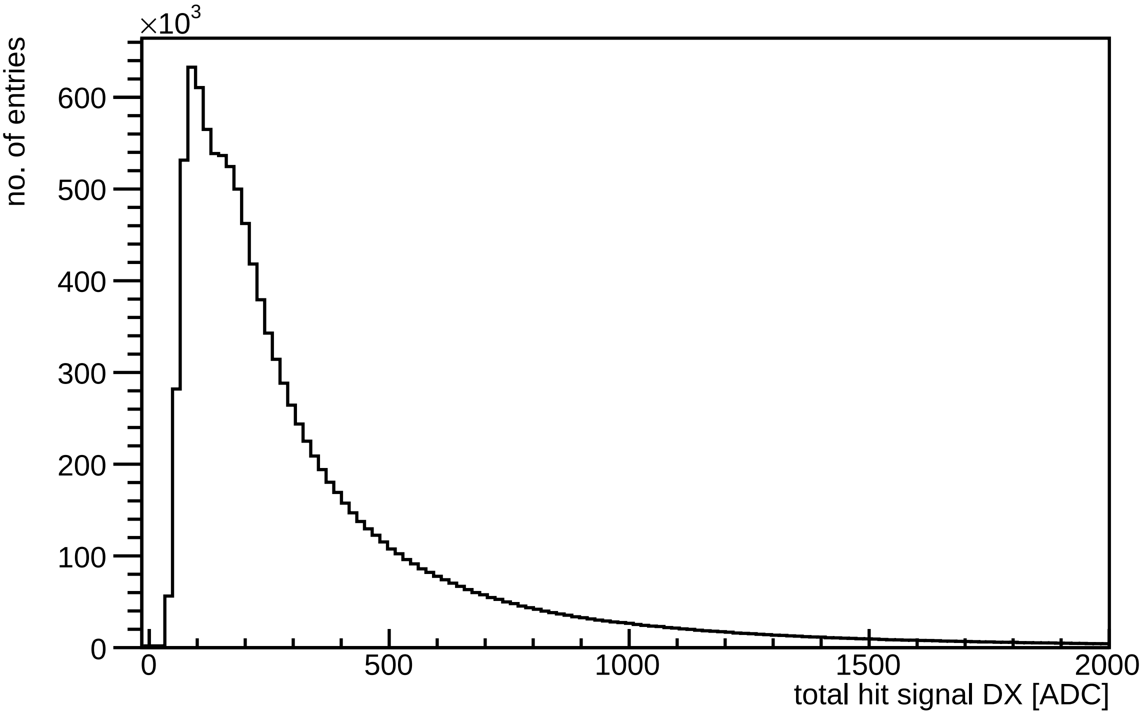

Figure 94: A distribution of the total hit signal in board DX.

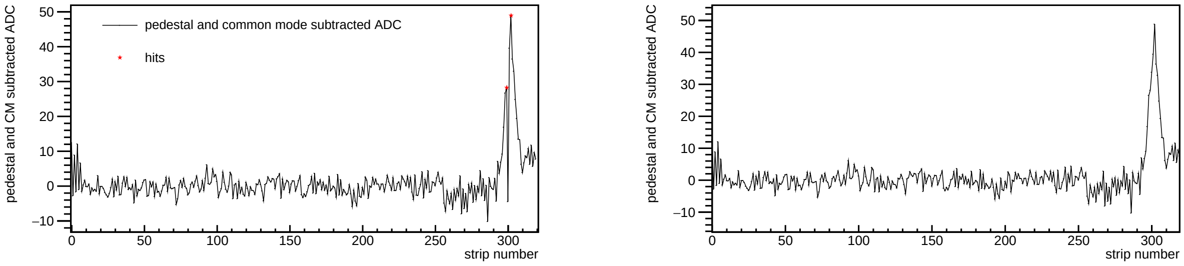

(a)

(b)

Figure 95: An example of a hit with a dead strip in the middle (left) and the hit after identifying and correction the signal dead strip (right).

strips) are detected, the inverted cluster is found. If it is found, the entire event is inverted and used for further analysis. The events after inversion are shown in figure 96b.

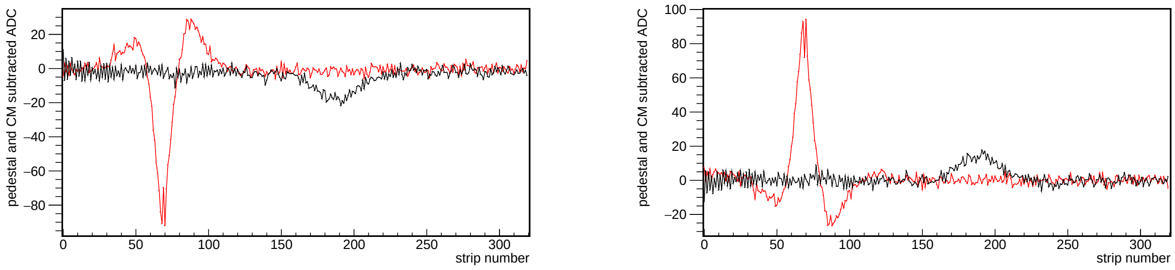

(a)

(b)

Figure 96: An example of an inverted hit (left) and the event after inverting the ADC data (right).

8.7 Track reconstruction

To find muon tracks, hits in different detector layers must be linked to each other based on their timestamp, see chapter 8.7.1. Once multiple muon hits are found in the same event, the next step is to reconstruct muon tracks. Muon tracks are reconstructed together with the scattering vertex which is then used in metric method (see chapter 3.4.3) and to create an image of the tested sample, see chapter 5.2.4.

8.7.1 Track candidates and timestamp matching

For hits occurring on different boards coming from the same muon, the timestamp (TS) value must be the same (or very close). The timestamps are encoded in the int-32 format, starting from a random value. The raw timestamp for all boards as a function of event number is shown in figure 97. As can be seen all boards display the same pattern but the starting time for each board is random. After subtracting the first value, all boards behave the same as can be seen in figure 98. One can spot that when raw TS reaches the maximum value of $2^{32} = 4294967296$, it resets itself. A correction was applied to have a monotonic dependence of the TS on event number by adding n*4294967296, where

n represents which drop it is. The result is shown in figure 99. Now hits occurring on different boards coming from the same muon, can be identified by comparing the TS value. When events which the same timestamps were identified, number of hits for every event was checked. If in one of the directions (ZX or ZY) three or more hits were find, a track candidate in that direction was created.

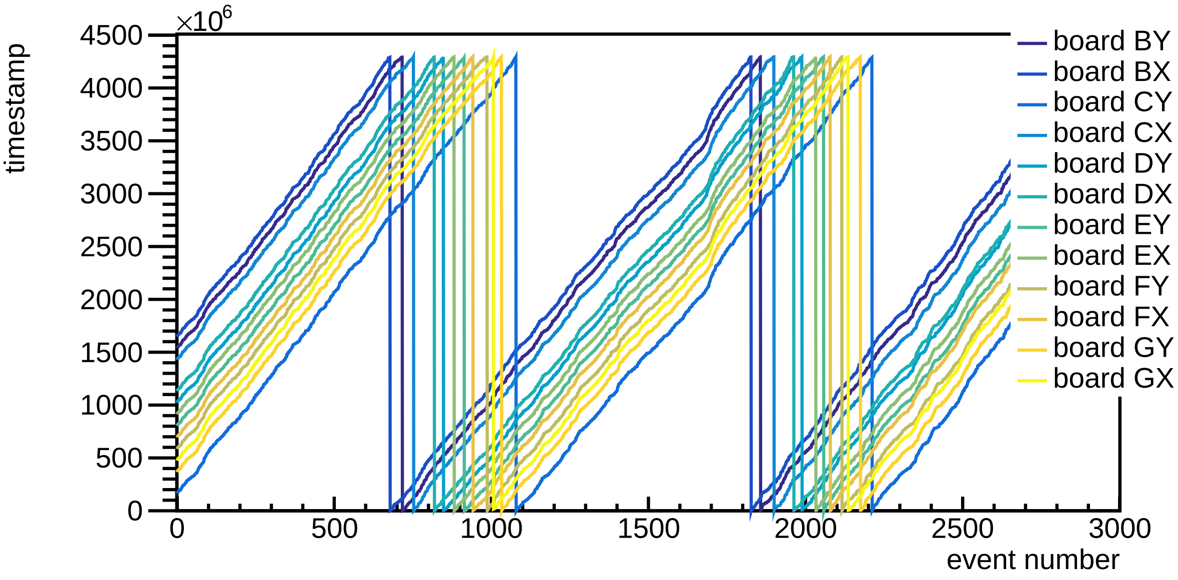

Figure 97: Raw timestamp values for all boards as a function of event number.

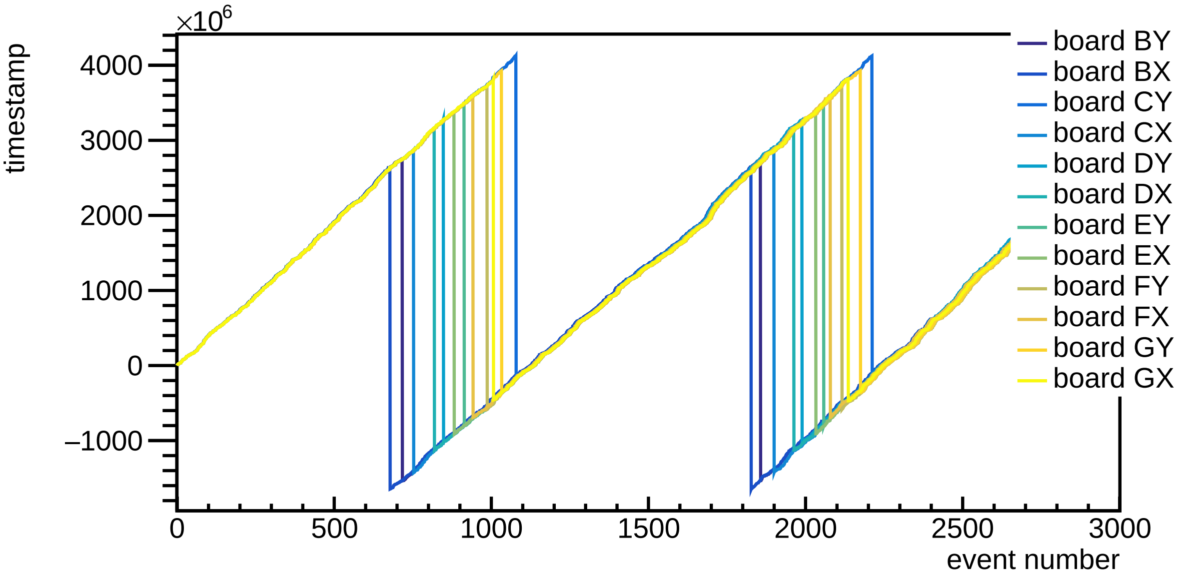

Figure 98: Corrected timestamp values for all boards after initial shift as a function of event number.

8.7.2 Sanity check on track candidates

Once track candidates were found, sanity checks were performed. The timestamps values between ZX and ZY track candidates were not matched at this stage of analysis. Plot 100

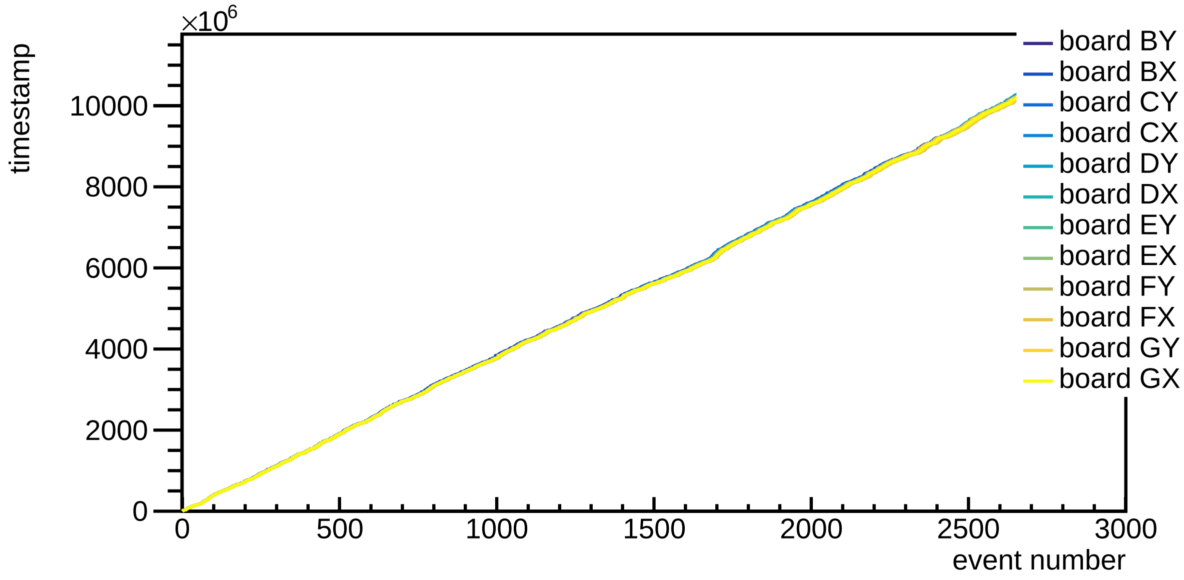

Figure 99: Final timestamp as a function of event number for all boards.

shows the number of hits per track in ZX and ZY. Very few tracks have hits in all of the layers and there were more tracks created in the ZX plane. Track candidates were fit with a straight line. Figure 101 shows the comparison of the χ^2 of the track fit in the ZX and the ZY direction. The tracks in ZX tend to have a higher χ^2 value. Please note that as the uncertainties on the hit positions are not known, the χ^2 is not properly normalised. As an uncertainty in the χ^2 formula a constants was used. Figure 102 shows track slopes in ZX and ZY plane. As the detector acceptance is limited and muons mostly come in vertically from above plane, the slopes of the tracks are small and centred around 0, as expected.

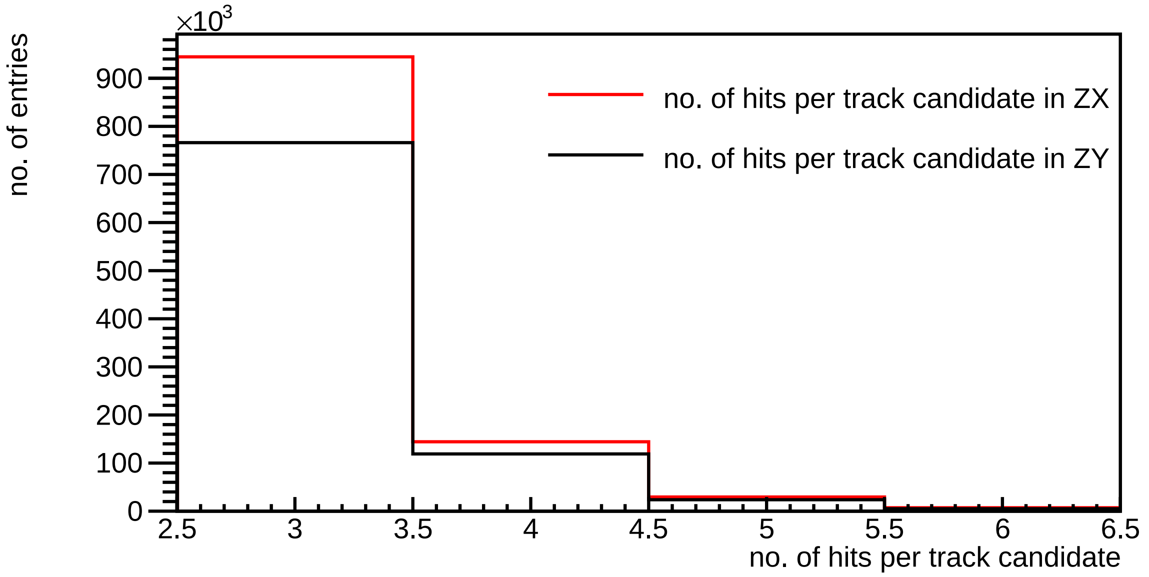

Figure 100: A histogram of the number of hits on the track candidates in ZX and ZY projection.

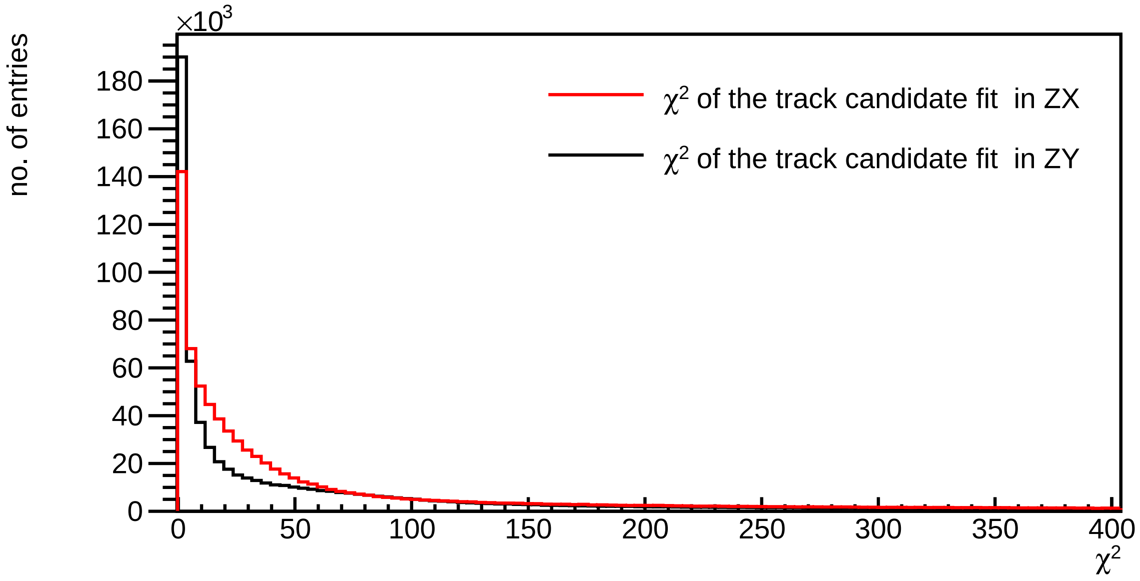

Figure 101: The χ^2 of the track candidate fit in ZX and ZY direction.

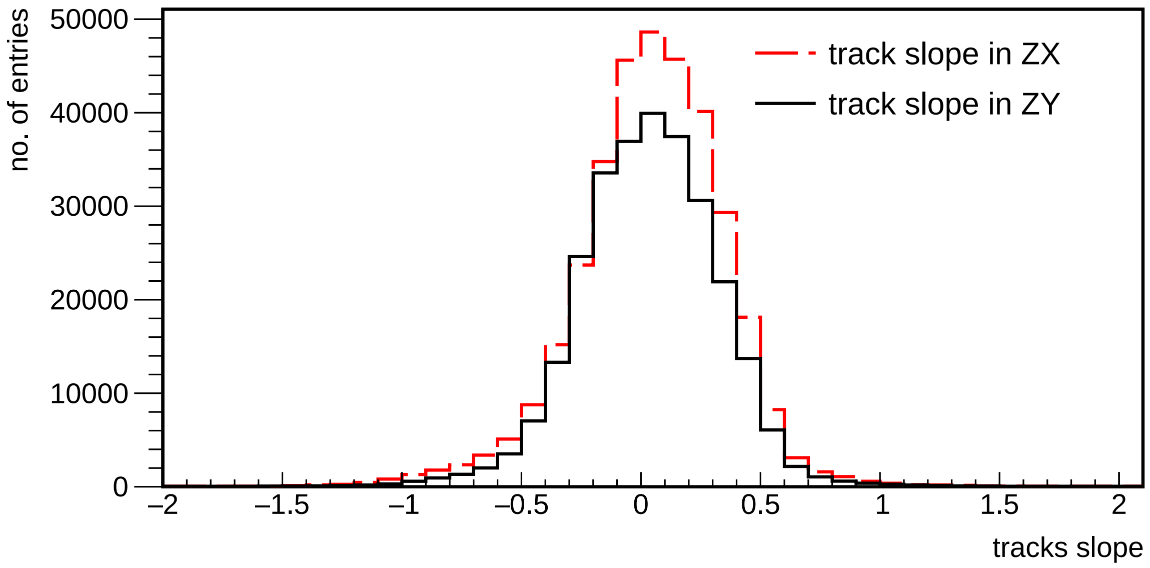

Figure 102: Track slopes in the ZX and the ZY plane.

8.7.3 Event display

To aid and cross check track finding an event display was developed. An event display is a multigraph which shows the detectors responses for one trigger for a single timestamp. The event display contains plots of the pedestal and common mode corrected signals as a function of detector strips converted to mm for all detectors in ZX and ZY projection. An offset is added to the baseline of the corrected signal, such that the Z axis reflects the real position of the detectors in the muon detection system. The X axis show the detector strip positions in mm. Four dashed, vertical lines show the boundaries between five MAROC3s. An example of the event display with seven muon hits and a track fitted in ZX projection is shown in figure 103. When a detector layer contained more than one hit for a given timestamp the hit that gave lower χ^2 was chosen to create a track.

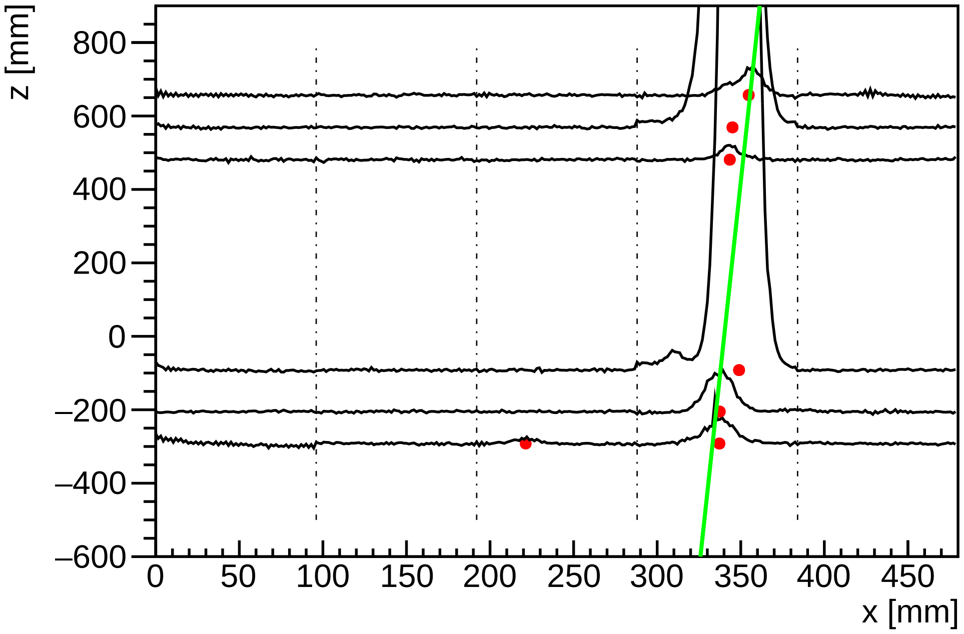

Figure 103: An event display in ZX projection. Seven muon hits and a straight line fit are visible. If multiple muon hits occur on one detector, the one which results in lower χ^2 of the track fit is chosen.

8.7.4 Track finding

The event display is used to visualize the data. However, the actual track finding is divided into two parts. Firstly, straight line fits are done separately through each set of hits: x/y and upper/lower planes, to check that these indeed are hits from the same muon. Next, to extract the scattering angle, a combined fit is performed. In the combined fit, the 3D track is forced to be two straight lines in 3D space meeting in a vertex. The result yields the vertex location, track slopes, scattering angle and the χ^2. Not all the reconstructed tracks are allowed in the further analysis. For both steps, tracks must have a χ^2 below

5000 to be included in further analysis. There is a compromise between statistics and the efficiency. This cut allows to eliminate the tracks that resulted from hits by more than one muon or complicated noise events. If the vertex is reconstructed outside of the volume of interest (the scanned sample), it is also rejected from further analysis. Due to geometric acceptance and imperfect efficiency, many events have less hits than the ideal 12 hits. To boost the statistics, it was chosen to also accept events with at least two hits in ZX/ZY and upper/lower planes for further analysis.

8.8 Residual and spatial resolution

Muon tracks are reconstructed on the assumption that the muons travel through the top detectors on a straight line, scatter in the scanned volume and then exit on a straight line. A muon can produce a hit in each detector which results in a cluster of strips carrying signal. The signals are used to reconstruct the position where the muon traversed the detector, see section 8.6. The spatial resolution is a measure for how well the positions are reconstructed.

8.8.1 Residual

Residual are calculated separately for every detector board. A residual for a detector plane is defined as a difference between the reconstructed hit position and the hit position obtained from a track fit to all hit positions except the hit position on the board under study. The residual is due to three factors: imperfect reconstruction of the position where the muon traversed the detector, precision on the predicted track position and multiple scattering between the last plane above the detector under test. The uncertainty on the predicted track position and the multiple scattering distribution can in principle be measured by studying the resolution when varying the incoming particle energy and/or using a Geant4 simulation using the exact detector geometry, see e.g. [93]. Here the muon energy is unknown and since an upper limit to the resolution is sufficient, the uncertainty on the reconstructed position is limited by placing a tight χ^2 cut on the incoming track fit. The lower the χ^2 the more narrow the residual distribution becomes as the uncertainty on the predicted position is reduced. This is shown in figure 104.

8.9 Spatial resolution

Spatial resolution is defined as the standard deviation of a Gaussian fit to the residual distribution. The spatial resolution for every board is listed in table 4 and ranges between 10 and 17 mm when operating with CO_2. This is much higher than the published resolution better than 500 µm obtained with mixture of Tetrafluoroethane R-134a (95%) and Iso-butane (5%). The main reason for the worse resolution is that the efficiency for

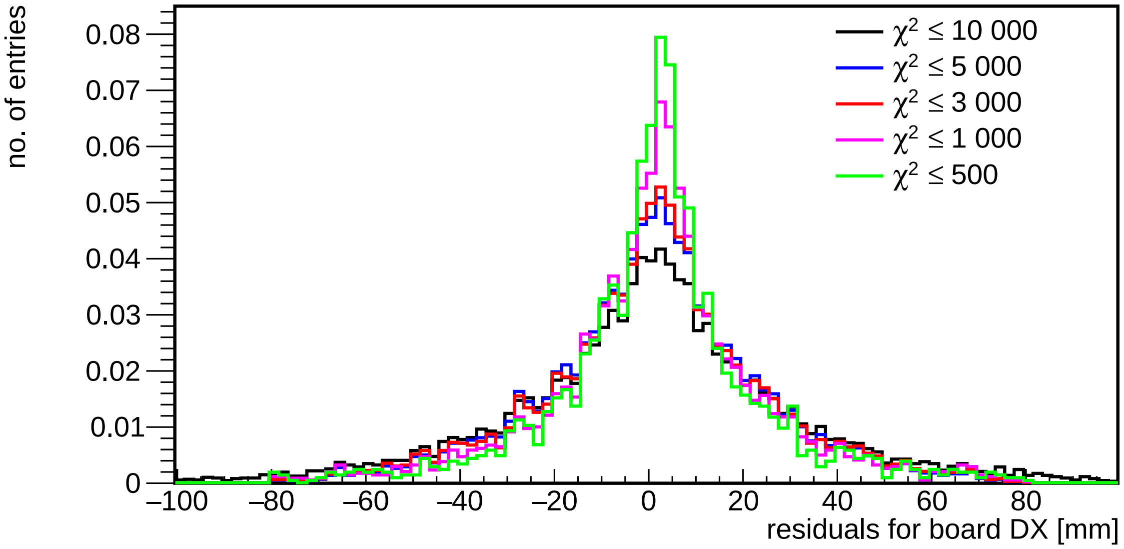

Figure 104: Residuals for board DX for different χ^2 thresholds.

the RPCs operating with CO_2 is much lower than when operating with Tetrafluoroethane R-134a and Iso-butane mixture. This was partly recovered by operating on a much higher voltage. The higher voltage leads to more streamers which have much worse position resolution than signals obtained in avalanche mode. Boards CY and DY and CX have the best spatial resolution below 15 mm, while boards GY and GX have the worst yielding almost 22 mm.

board number	spatial resolution [mm]
0 - BY	16.23 ± 0.43
1 - BX	15.50 ± 0.36
2 - CY	14.19 ± 0.40
3 - CX	14.93 ± 0.38
4 - DY	14.86 ± 0.37
5 - DX	15.50 ± 0.34
6 - EY	20.09 ± 0.57
7 - EX	19.03 ± 0.43
8 - FY	18.99 ± 0.50
9 - FX	17.97 ± 0.37
10 - GY	21.70 ± 0.64
11 - GX	21.75 ± 0.55

Table 4: Spatial resolution for every board.

8.10 Efficiency

When a track points at a location in a detector, there is a probability that a hit is found around that location. This is the efficiency of the detector. To calculate efficiency of a detector, a total number of tracks T_i is reconstructed without looking at the detector under test. There is a number of hits found h_i and a number of missed hits m_i and:

$$T_i = h_i + m_i \tag{16}$$

then the efficiency ε_{b_i} for detector b_i is given by:

$$\varepsilon_{b_i} = \frac{h_i}{T_i} = 1 - \frac{m_i}{T_i} \tag{17}$$

and the uncertainty in the efficiency $\sigma_{\varepsilon_{b_i}}$ is given by:

$$\sigma_{\varepsilon_{b_i}} = \sqrt{\frac{\varepsilon_{b_i}(1 - \varepsilon_{b_i})}{T_i}} \tag{18}$$

To established if a particle passed through a given detector layer, a track fit is done through the remaining detector layers. The hit is found when the extrapolated track points at a strip which is included in a hit cluster on a given board. For this calculations tracks with 5 and 6 hits were used.

The efficiency for every detector boards is shown in table 5. Boards DX and DY have the best efficiencies around 70%, while boards BY, BX and GY have the worst efficiencies which are lower than 50%. Remaining boards are characterized with efficiencies between 50% and nearly 67%.

board number	efficiency ε_{b_i} %
0 - BY	47.03 ± 0.48
1 - BX	49.51 ± 0.41
2 - CY	62.91 ± 0.54
3 - CX	66.22 ± 0.45
4 - DY	69.00 ± 0.54
5 - DX	72.40 ± 0.45
6 - EY	58.05 ± 0.53
7 - EX	65.09 ± 0.45
8 - FY	60.33 ± 0.53
9 - FX	56.13 ± 0.44
10 - GY	47.34 ± 0.48
11 - GX	52.83 ± 0.43

Table 5: Efficiency for every board.

The low detector efficiency results in a low track efficiency. The track efficiency is given by the product of the detector efficiencies:

$$\varepsilon_{T_{zy}} = \varepsilon_{b_0}\varepsilon_{b_2}\varepsilon_{b_4}\varepsilon_{b_6}\varepsilon_{b_8}\varepsilon_{b_{10}} \tag{19}$$

$$\varepsilon_{T_{zx}} = \varepsilon_{b_1}\varepsilon_{b_3}\varepsilon_{b_5}\varepsilon_{b_7}\varepsilon_{b_9}\varepsilon_{b_{11}} \tag{20}$$

and the uncertainty was calculated using propagation of uncertainty method. The track efficiency in the ZY plane is $\varepsilon_{T_{zy}}$=3.38±0.08% and in the ZX plane $\varepsilon_{T_{zy}}$=4.58±0.08%.

8.11 Imaging of the concrete object

Muon scattering tomography is used to scan unknown volumes. Many successful applications have been reported, see chapter 3.4. The Bristol discriminator algorithm, see chapter 3.4.3, uses the concept of clusteredness of high angle scattering vertices - thus higher-Z materials can be distinguished from lower-Z objects. This method was applied on the muon data gathered with the muon tracker. Figure 105 shows the results. The scanned object was divided into 50 × 50 × 50 mm^3 voxels and for every voxel mean of the discriminator distribution was calculated. To investigate local changes, several cross-sections were created along the Z axis, creating a 2D distribution of discriminator value - the image. The imaging process used here is different form the one presented in chapter 5.2.4 because of a lack of the reference background scenario. However, due to use of CO$_2$ and thus low track efficiency, it was not possible to achieve a clear image of the unknown concrete object. The N parameter, see chapter 3.4.3, was set to 3. This value is too low to work with a representative sample of tracks scattered in a given voxel. The chosen voxel size was relatively big and did not allow to produce images with the desired resolution. These variables have been set at these values due to insufficient number of reconstructed tracks. A higher value of the N parameter and the use of smaller voxels would result with no data in many voxels.

After the image of the concrete block was done, the industry partner shared the contents of the sample. Various pieces have been arranged throughout the entire volume of the 200 × 330 mm^2 concrete block. Among them, at the top of the block, two halves of a mesh made of rods with a diameter of 10 mm and the square gap in the middle of 50 × 50 mm^2 were placed horizontally. On the side, another mesh was placed vertically. It was made of rods with diameters of 12 and 16 mm with the square gap in the middle of 100 × 100 mm^2. Next, in the centre of the block, there was a cube of low density concrete (celcon block), which was approximately 50 × 50 mm^2. At the bottom, a corroded 50 × 50 mm^2 angle with a thickness of 6 mm was inserted.

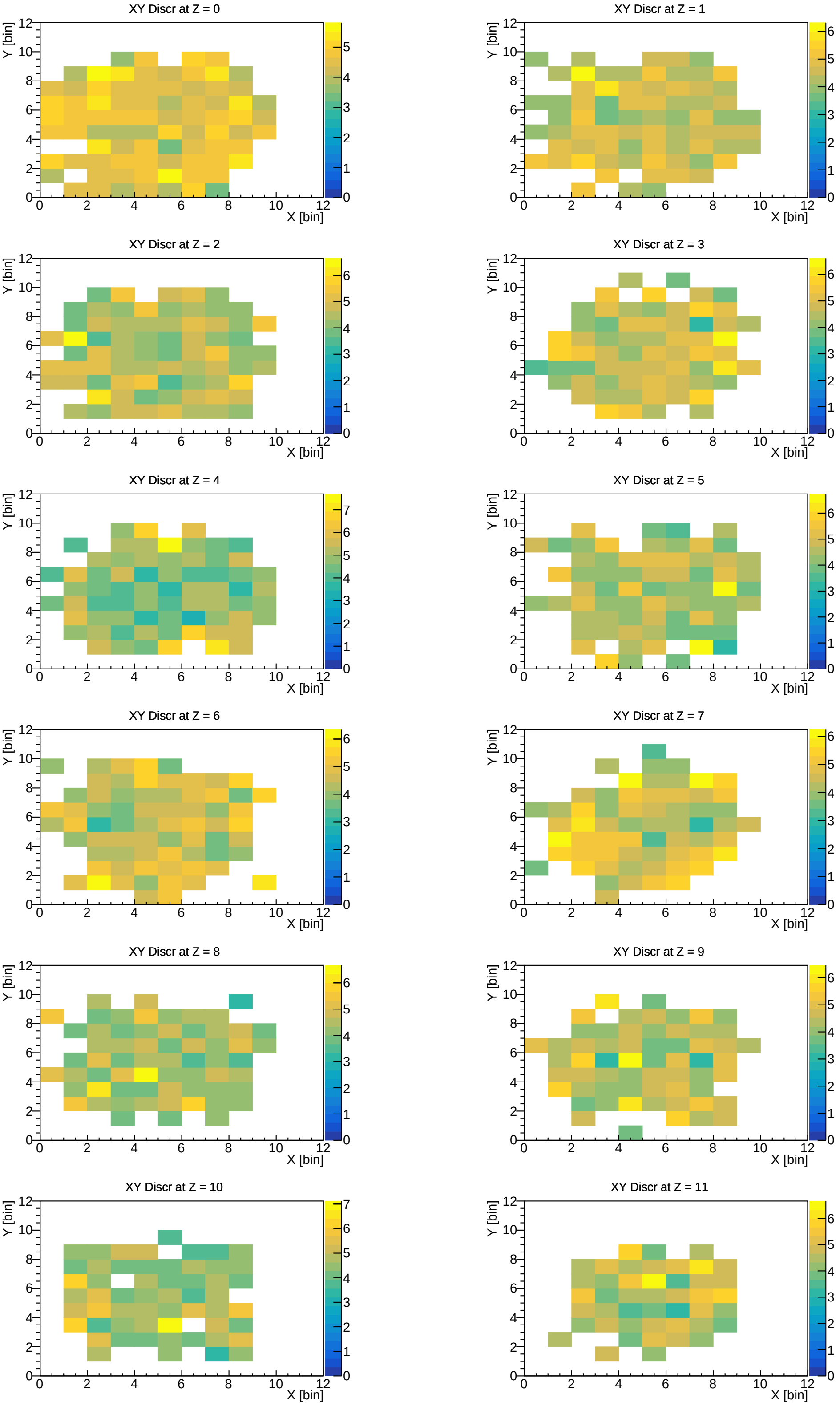

Figure 105: Images of a concrete block with and unknown content. Multiple images along the horizontal plane were created to detect local variations.

8.12 Conclusions

A muon detector was build using high resolution glass resistive plate chambers. Due to new legal regulation it was no longer possible to use a mixture of a Tetrafluoroethane R-134a (95%) and Iso-butane (5%). The resistive plate chambers were operated with CO_2 instead. The DAQ and offline analysis software were significantly improved by the author. However, with CO_2, the spatial resolution increased from 450 µm to between 14 and 22 mm. The detector efficiency for a single RPC layer was found to be between 47.03 ± 0.48% and 72.40 ± 0.45%. This results in a low track efficiency, where the track efficiency in the ZY plane yielded 3.38 ± 0.08% and in the ZX plane 4.58 ± 0.08%. Imaging of a concrete block with internal structure was attempted. With the insufficient number of muon tracks the quality of the image is not satisfactory. Nevertheless, the system is ready to operate well with a new gas. Despite the unsatisfactory results, this work is of high importance for the community. There is an ongoing challenge to many research projects to adjust to new legal requirement, thus there is a real need to find replacements of gases which give satisfactory position resolution and efficiency. Many groups around the world are working on testing new environmentally friendly gas mixtures. When they become available, the performance of this system will be tested again.

9 Scattering tomography for proton radiotherapy

Proton radiotherapy is a form of radiotherapy for cancer treatment, where a beam of protons is targeted at a tumour. By ionisation in the cancerous tissue, DNA is damaged in the cancerous cells, leading to cell death. Radiotherapy is most commonly administered using X-rays. This has the disadvantage that the beam traverses the whole body and deposits energy along the path of the beam and therefore does damage to all tissues; including healthy tissue. To optimise the dose to the tumour and minimize the dose to the healthy tissue, the beam is moved around the patient. Proton therapy has the key advantage that the protons deposit most of their energy over a short range, the so-called Bragg peak, thus a high radiation dose can target the tumour very precisely, while the healthy tissues around it are not damaged much. However, the rapidly changing dose deposition makes proton radiotherapy highly sensitive to differences of the Bragg peak range. The location of the Bragg peak depends on the energy of the incoming proton and amount of the traversed tissue and the type of it. The comparison between X-ray and proton therapy is shown in figure 106. Determining the exact location of the tumour is therefore essential for effective therapy. However, the location of the tumour varies over time. This can be due to many factors like losing weight, surgeries, upswelling and organ movement. Thus, the amount of tissue the proton beam traverses before reaching the tumour is likely to change. It makes radiotherapy planning challenging. A solution to this is to have a 3D map of the relative stopping power (RSP) for each patient just before applying the therapeutic dose. This guarantees that the energy is delivered precisely in the tumour since it reduces the uncertainty, leading to a reduction of the dose deposited to healthy tissues around the tumour and more effective therapy. The RSP is the ratio of the proton stopping power of the actual tissue traversed normalised to the stopping power of water. The stopping power is defined as the mean energy loss per unit path length.

There are a few ways of producing 3D relative stopping power maps for the proton radiotherapy planning process. Currently, the most commonly used technique is a computed tomography (CT) scan, where CT numbers are converted into tissue stopping power ratios relative to water. They are used to compute the beam range and the energy deposited in the patient body. However, the crucial role in minimizing errors in dose delivery is the precise conversion from CT numbers to stopping power ratios because the conversion procedure increases uncertainties of the proton range. This is because CT scans measure densities and not stopping powers. The combined uncertainty in proton range estimation coming from CT calibrations was reported to be 2.7–3.5% + 1.0–1.2 mm [94]. The 3.5% + 1 mm uncertainty range results in a potential unintentional overrun of 8 mm for a 20 cm range field in soft tissue, which is significant [95].

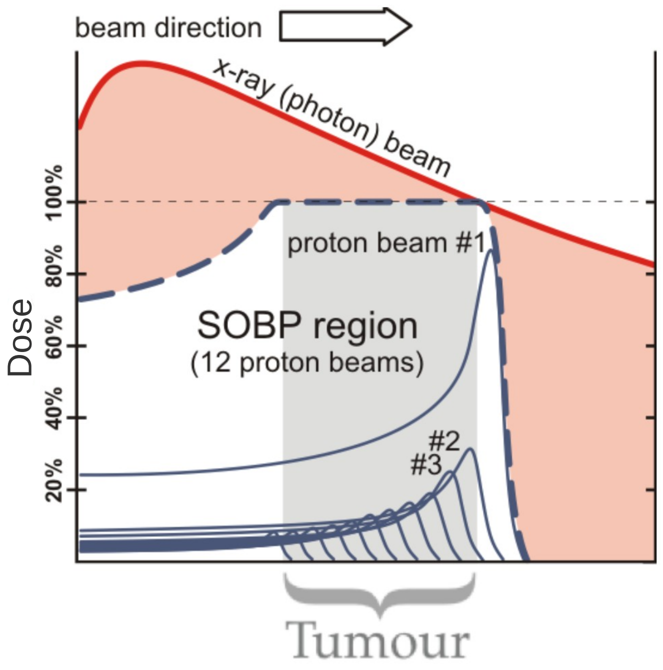

Figure 106: Energy deposition as a function of the depth in the body for an X-ray beam, a single proton beam and a Spread Out Bragg Peak (SOBP) combining proton beams with twelve different energies [96]. The spread out technique is used to target the whole volume of the tumour.

Several groups worldwide are working on the development of proton Computed Tomography (pCT) imaging systems with the aim of reducing range uncertainty in treatment planning to $<1\%$ [97, 98, 99] and developing a novel device which can be used to reconstruct 3D images using high energetic proton beams [100]. Proton CT requires a higher energy beam such that the protons exit the patient. By comparing the incoming and outgoing proton energy, the energy loss in different directions can be measured and thus the energy loss and thus stopping power is known.

The method presented in the previous chapters is sensitive to the stopping power. Therefore, it is interesting to study whether the technique can be used to determine a map of the RSP using a very small radiation dose. This is important as the protons will add to the total dose received but will not be of therapeutic value and thus be detrimental to the patient.

9.1 Simulation setup

To check the potential of scattering tomography with protons number of simulations were performed. The simulations first cover differentiation between soft tissue, bone, air and uranium. Next the same methods are applied on a more complex geometry involving human phantom to distinguish soft tissue from bone.

9.1.1 Basic material description

When using the metric method presented in the chapter 3.4.3, one is sensitive to the differences in radiation length between the different types of tissue. Radiation lengths for relevant materials are listed in table 2. To check the performance of the method to distinguishing basic materials an initial test was done. The geometry consisted of a $9 \times 6 \times 9$ cm^3 box filled with soft tissue. Inside that box, there were four $2 \times 2 \times 2$ cm^3 cubes placed filled with soft tissue, bone, air and uranium for contrast. The scattering angle distributions for the four different materials placed in the master box are shown in figure 107. The average scattering angle in air is the smallest. The scattering for soft tissue is larger than in air but lower than for bone. The highest scattering is observed for uranium, as expected.

Next, the metric value (chapter 3.4.3) was calculated for simulation data and a two dimensional histogram of that value (metric image) was created using 2 mm voxels, see figure 108. Uranium, bone and air are clearly distinguishable from the background soft tissue. Moreover, the results are consistent with those shown earlier in the thesis. The highest metric value was achieved for the air cube, while the lowest for uranium.

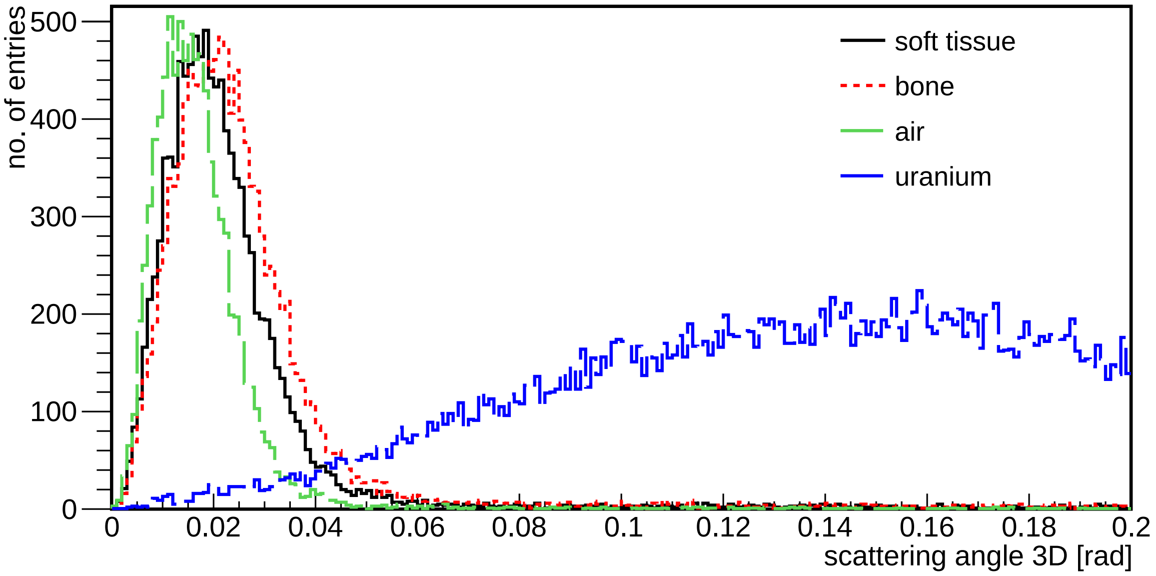

Figure 107: Scattering angle distributions for the four different materials using proton scattering techniques.

9.1.2 Distinguishing between tissues in the human phantom

Since the discrimination of the basic materials has shown potential for the method, a human phantom shown in figure 109 was used next. A model of a human phantom was taken from the Geant4 Human Phantom advanced example [101, 102] and was modified to be integrated with the software used for the MST study. The phantom has a more complex inner structure because more materials are put next to each other and thus is

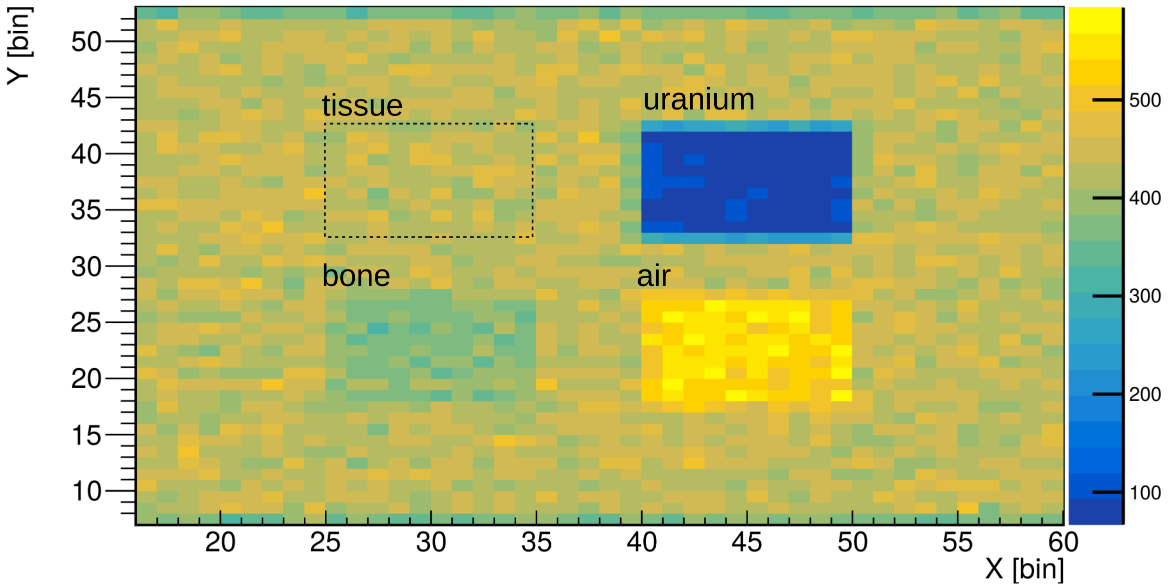

Figure 108: Metric image of the box with four cubes filled with different materials obtained with proton scattering tomography.

more difficult to be imaged. In the simulations a male phantom was used lying down on a treatment bed (the bed is not included in the study). On both sides of the phantom, four silicon detectors were placed. The detector measured 80 cm × 80 cm × 100 µm and was based on the Lassena MAPS [103], which has a 50 µm pitch. A position resolution of $50/\sqrt{12}$ µm was used. The object was scanned with a beam of protons coming from above of the top most detector. The beam was modelled as a 90×90 mm^2 plane and 8281000 protons were fired every scan with a kinetic energy of 230 MeV. This value was chosen as a compromise; the higher the proton energy, the less the scattering and thus the lower the contrast between the tissues, while on the other hand the transmission is higher for higher beam energies and less dose is deposited in the patient. At this energy more than 90% of protons passed through the phantom and were registered by the bottom detectors. This energy is available in the typical proton therapy centres where protons are accelerated to therapeutic energies ranging from 70 to 250 MeV [104]. This resulted in a deposited dose of the order of 10^{-5} Gy. This is a negligible dose used for imaging. All cancers are treated with very individual dosages but conventional radiotherapy dosages for head and neck cancer treatment are typically daily fractions of 1.8–2.0 Gy resulting in total doses of 66–70 Gy over 6 or 7 weeks of treatment [105]. Hence, the dose added during the imaging process is not significant and the imaging process is safe for the patient.

Part of a chest was scanned covering an area of 90×90 mm^2 which included ribs, soft tissue around it and lungs. Ribs were elliptical in shape, with the width of 14 mm and thickness of 5 mm. To check the method, ribs were modelled as organs made from uranium, bone and soft tissue. The metric value was calculated metric images created. The results are shown in figure 110, 111, 112. To make reading the figures easier, red boxes have been added to the plots. They indicate where the ribs are located. Ribs modelled as uranium, are clearly distinguishable by eye from the soft tissue around them. For the ribs modelled as bone, the difference between bone and soft tissue is not clearly visible by eye. To enhance the signal from bones, an image with the ribs made from soft tissue (background, figure 112) was subtracted from the bone one. Result can be seen in figure 113. By eye it is still difficult to say where the ribs are, however some hint of signal can be seen. To further enhance the signal from bones, the integral along the Y axis was calculated and plotted versus the X position in the phantom, see figure 114. Areas with the bones are characterized by negative signal values, whereas soft tissue gives positive signal values. Hence, when taking the integral of the data, the position of the ribs can be found.

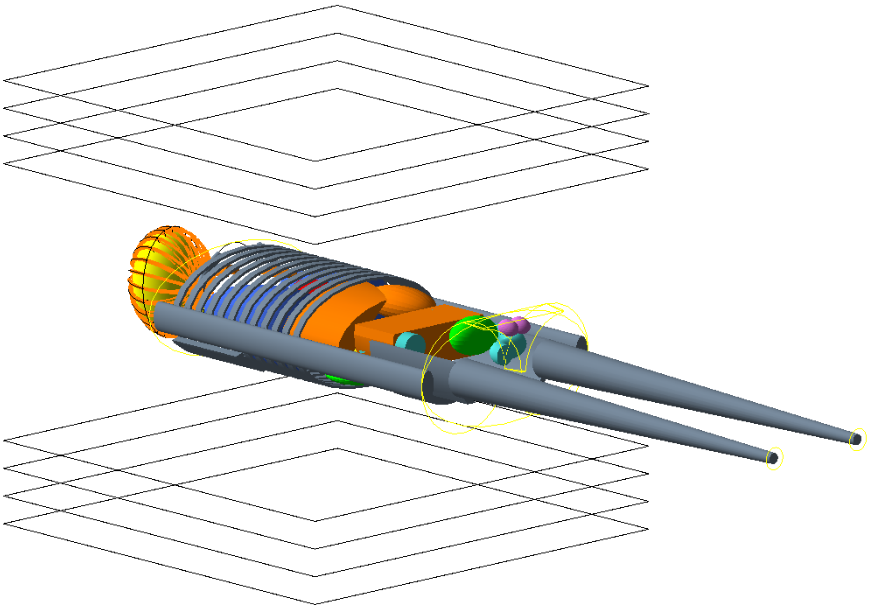

Figure 109: Sketch of the human phantom used in the simulation study [101, 102].

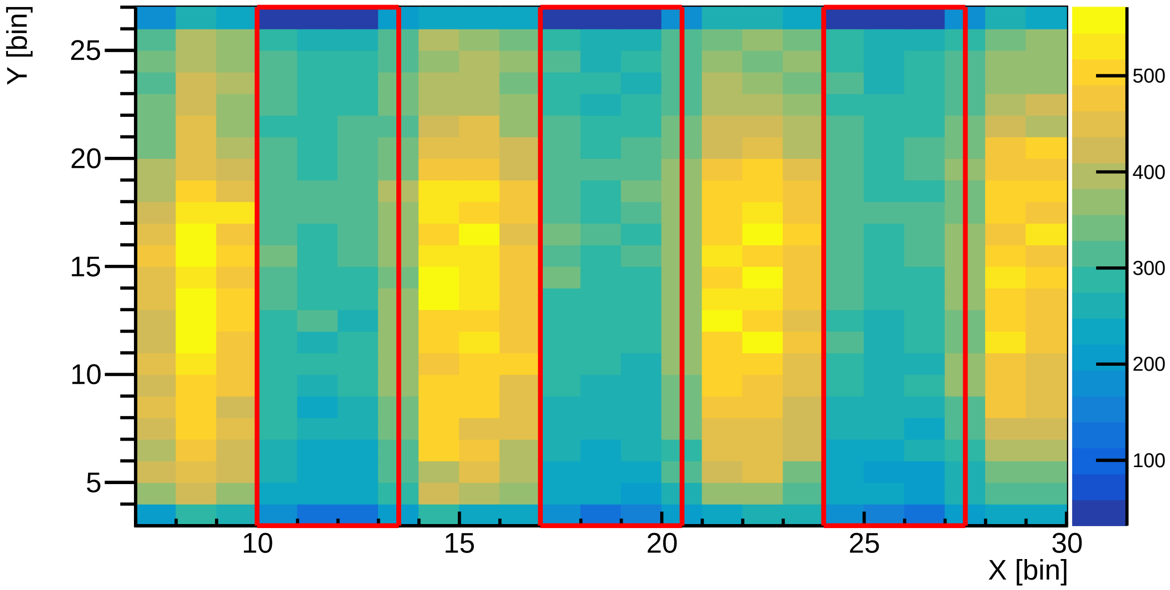

Figure 110: A metric image of the phantom with ribs made from uranium. Red frames show where to ribs are.

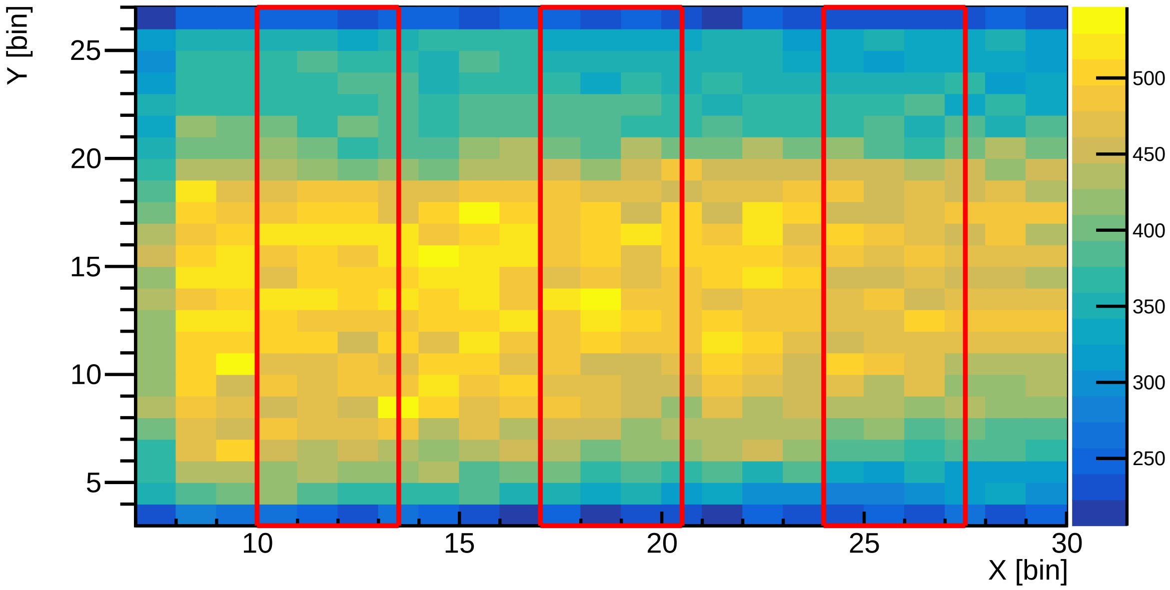

Figure 111: A metric image of the phantom with ribs made from bone. Red frames show where to ribs are. Ribs are surrounded by soft tissue.

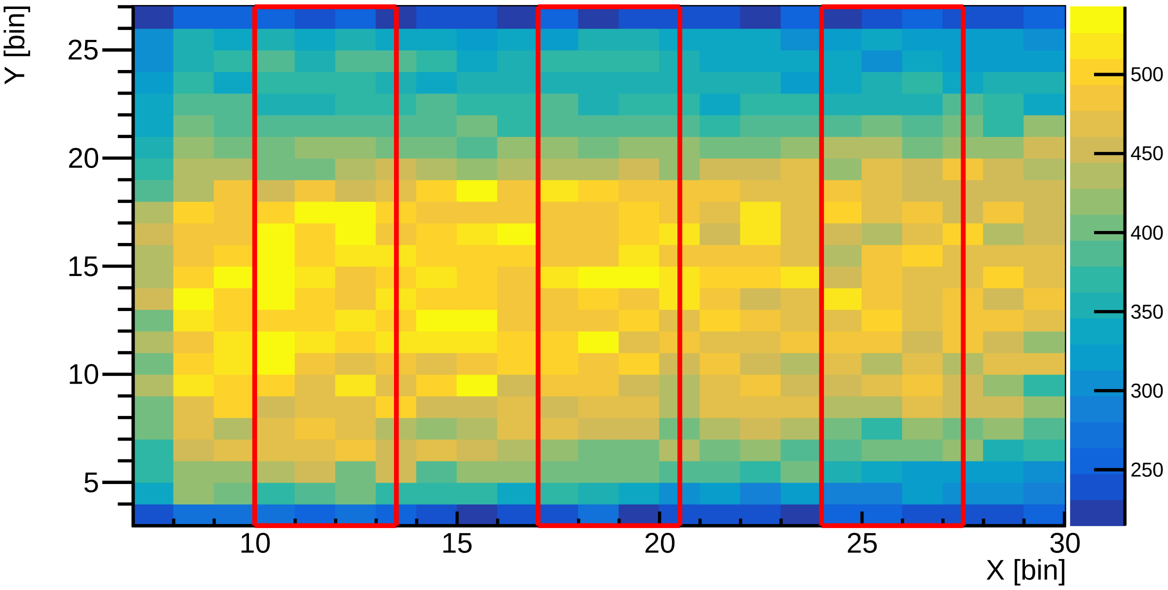

Figure 112: A metric image of the phantom with ribs made from soft tissue. Red frames show where to ribs are. Ribs are surrounded by soft tissue.

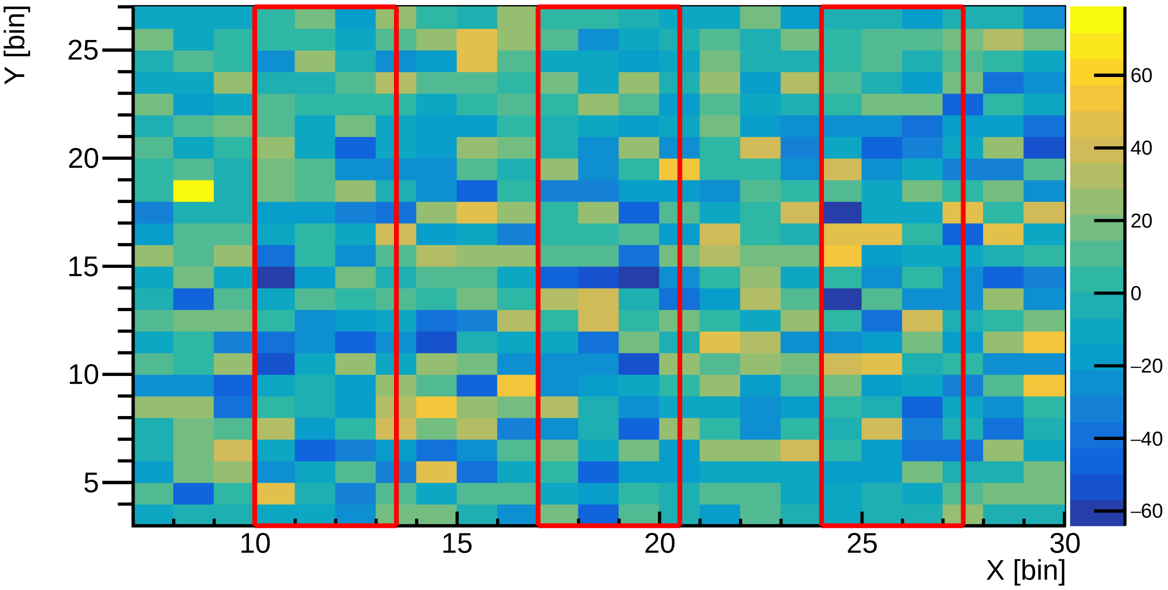

Figure 113: Background subtracted metric image for ribs made from bone. There is a hint of areas with the dark blue signal, which shows the location of the ribs. Red frame shows where to ribs are.

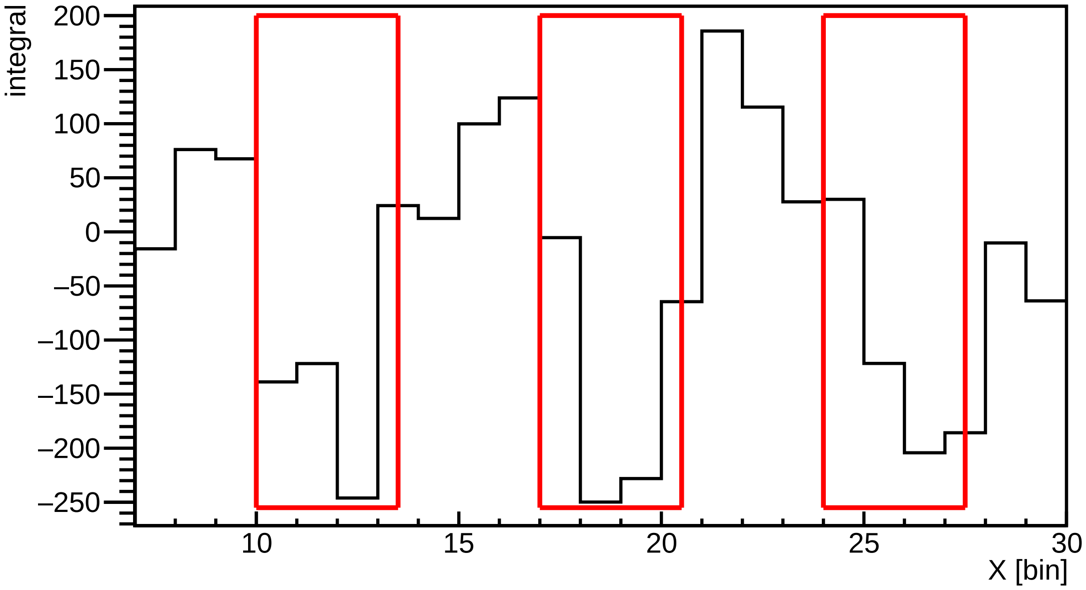

Figure 114: An integral along Y axis combing all signal values. Red frame shows where to ribs are.

9.2 Conclusion

This short work presented here shows promising potential for using scattering tomography methods on protons for medical proton CTs. A proof-of-principle study showed that it is possible to distinguish soft tissue from bone, air and uranium. When applied to the phantom geometry, the method found the positions of ribs. This is a good start but further development is needed to study the suitability of the method, including simulations of a cancerous tissues. Further studies are required to optimize an algorithm to find the lowest possible dose, which still provides sufficient image quality and to calculate reconstructed position resolution. Finally an conversion is needed to translate the tomographic image into a RSP map.

10 Future development of the methods

The main topic of this thesis was to develop muon tomography to locate rebars in thick concrete objects. The methods presented here demonstrate clearly that the technique can be used for this application. To take this technique further, it is essential to investigate to which extent the method can reveal information about the (corrosion) state of the rebars. As iron oxide has a different density than normal steel, the method is fundamentally sensitive to the degree of oxidation. Another further step would be experimental verification of the method. To achieve this an existing muon tomography system was refurbished and updated. Unfortunately, at this moment in time, there were no environmentally friendly gases available with good performance. Many groups around the world are investigating new mixtures. When these become available, experimental verification can be done.

Moreover, the rapid advancement of Machine Learning and Artificial Intelligence opens new possibilities for improving data analysis, reconstruction accuracy, and automation, which will undoubtedly enhance the usefulness and expand the range of applications of muon tomography in the near future.

The muon tomography techniques are directly sensitive to the stopping power of the material traversed. In this thesis a proof of principle study was presented where the analysis method was used to image a patient for proton radiotherapy. It was shown that the method has a potential, but more work is required to improve the imaging. Nevertheless, the method clearly has merit and can potentially make live images of the patient that can be used to adapt the treatment on the fly while minimizing the non-therapeutic dose to the patient.

Muon tomography is a very exciting and fast developing technology that slowly but surely is being accepted and taken up in the NDE community.

11 Summary

In this dissertation, the challenge of non-destructive evaluation (NDE) of thick concrete structures using muon scattering tomography was discussed. Current non-destructive evaluation approaches (presented in chapter 2) address a subset of inspection challenges, but there are still certain situations where inspection tools are lacking. Inspecting larger constructions like bridges or buildings with multiple layers of reinforcement is an ongoing challenge. Civil and structural engineering require a non-invasive solution to know the position, type and quality of reinforcement in concrete objects at great depths, while current technologies only provide solutions at restricted depths. Muon scattering tomography can help with these challenges. This is the primary focus of this thesis.

Muon scattering tomography is a non-invasive and non-destructive method that uses highly penetrating, secondary cosmic rays – muons – for imaging of large and dense objects. While traversing layers of matter, muons undergo scatterings, which modifies their trajectories. Measuring the muon tracks before and after passage through an object of interest allows for its inspection and 3D imaging. Such a study can be performed without the additional radiation, as cosmic muons are ubiquitous with the flux at sea level of about 10 000 $m^{-2}min^{-1}$.

Using Monte Carlo simulations, the author showed that muon scattering tomography is an appropriate tool to address the gap in the non-destructive evaluation testing and ensure safe inspection of big, reinforced concrete structures. The first attempt to develop a new NDE method, described in chapter 5.1, allowed to detect and measure rebars in concrete objects. Rebars with a minimum diameter of 33.7±7.3 mm and a length of 100 cm were detected. For the rebar volumes above 2 500 cm^3, their volume was reconstructed with a resolution of 5.4±0.3%. The result was independent of the rebar's location. The imaging technique was further developed. It allows seeing the interior of the reinforced concrete blocks and differentiating between one and two layers of rebar grid. When using the imaging approach, a hint of a signal of 20 mm diameter rod can be seen. It was also proven that two reinforcement bars are detected as two objects when placed at least 6 cm apart, but the separation starts to be visible from a distance of 4 cm.

The approach was further improved to lower the detection threshold. This was presented in chapter 6. To do so, the fact that the reinforcing grid forms a periodic structure was used. The signal from the reinforcement was enhanced with a modified auto-correlation technique and then Fourier-transformed. Peaks in the normalised Fourier frequency spectrum indicate that a repeating structure, such as a grid, is present. The amplitudes of the peaks are proportional to the rebar sizes, whereas the positions of the peaks are determined by the grid spacing. After one week of data collection, a grid composed of rebars with diameters greater than or equal to 7 mm and spacing of 10 cm can be observed. The signal for a

6 mm diameter rod exceeds the background level after a week of measurements, but it grows stronger after two weeks of data collection. When the spacing increases to 20 cm, longer data collection is required since there is less iron in the scanned region.

A further development of the approach was shown in chapter 7. This includes a method to detect and locate a second layer of reinforcing mesh. It was proven that the method works up to a few centimetres of accuracy which is more than enough for non-destructive civil structure evaluation.

The next chapter of the thesis demonstrates the use of the method in practice. It also addresses the challenge of finding an alternative gas to use with resistive plate chambers. A Tetrafluoroethane and Iso-butane mixture, which is considered to be a greenhouse gas, is no longer possible to use due to changes to the law. A high resolution glass resistive plate chamber system existed but was always operated with environmentally unfriendly gases. The system was refurbished, updated and improved to study the performance while operating with CO_2. A concrete block with unknown content was scanned for a period of time. The entire process from data collection to image reconstruction of the scanned object has been discussed in detail. When compared to the former gas mixture, the spatial resolution increased from 450 µm to between 14 and 22 mm when using CO_2. The detector efficiency was determined to be between 47.03 ± 0.48% and 72.40 ± 0.45% per detector plane. This results in an insufficient track efficiency, with the track efficiency in the ZY plane yielding 3.38 ± 0.08% and the track efficiency in the ZX plane yielding 4.58 ± 0.08%. Images of the cross-sections of the scanned volume were prepared. Due to low efficiency of the detector working with CO_2, imaging of the scanned object was not satisfactory. Despite that performance, this is an important piece of work as there is an urgent need to find environmentally friendly gases which give sufficient position resolution and efficiency. When these become available, the system performance with the new gas can be tested. This would allow for experimental verification of the newly developed methods for rebars location.

The research described in chapter 9 demonstrates the promise of employing scattering tomography methods with protons for medical proton computed tomography. A proof-of-concept study has shown that soft tissue can be distinguished from bone, air and uranium using proton scattering tomography. When applied to a complex phantom geometry, ribs were distinguished from surrounding tissue. To perform one scan, a dose of the order of 10^{-5} Gy was deposited. This is negligible for such an application. Further research is needed to determine the full potential of the method, including simulations of cancerous tissues. More research is needed to optimise an algorithm to determine the lowest feasible delivered dosage while maintaining adequate picture quality and to translate the tomographic image into a RSP map, but these early results are highly encouraging.

List of Figures

1 Rebar imaging capabilities of the most common techniques. 20
2 Ground penetrating radar testing. 22
3 An infrared image of a bridge wall. 23
4 An example of a shower of secondary cosmic rays. 27
5 Muon intensity versus muon momentum for different zenith angles, θ. . . . 28
6 Contributions to the energy loss of muons in standard rock due to bremsstrahlung, production of pairs and photonuclear interactions. 30
7 Energy loss for positive muons in copper as a function of $\beta\gamma$. 30
8 Illustration of multiple Coulomb scattering in the context of muon scattering tomography. 32
9 Schematic sketch of a muon radiography approach for a volcano's summit. 33
10 Muon scattering tomography principle. 33
11 PoCA imaging reconstruction algorithm. 35
12 An example of the distribution of the ln(weighted metric) for single voxels containing different materials. 37
13 The discriminator distribution for a concrete-filled object, a concrete-filled object with rebar inside and concrete-filled object with gas void inside. . . 37
14 Schematic drawing of the detector setup used in the laboratory. 41
15 A simulation with a concrete block and two layers of iron rebar grid. 41
16 Sketch of the geometry with a rebar inside a variable size concrete cuboid. 44
17 Sketch of the geometry with the rebar inside a fixed size concrete cuboid. . 44
18 A single layer of rods in a concrete block. 45
19 A single layer of a grid in a concrete block. 45
20 A two grid layer scenario in a concrete block. 45
21 Signal as a function of the rebar volume for a variable size concrete block. 47
22 Signal for a rebar in a fixed size concrete block as a function of the rebar volume. 48
23 Reconstructed rebar volume as a function of the simulated (true) rebar volume. 49
24 Relative uncertainty of the reconstructed volume as a function of the actual reinforcement volume. 50
25 The definition of the sliding window in ZY projection. 51
26 Images of a concrete only geometry and images of the concrete block with a 50 mm diameter rebar. 52
27 Signal distribution for a central region of a concrete only scenario and rebar with a diameter of 20, 30, and 50 mm. 53

28 Signal excess fraction as a function of rebar diameter and rebar diameters ranging between 0 and 70 mm. 53
29 Images of a concrete block with a rod of 20 mm diameter (left) and rod of 30 mm diameter (right). 54
30 An iron rod with a diameter of 30 mm placed in 4 different locations of the concrete object. 54
31 Images of two rods placed in different distances in respect to each other. . 55
32 Reinforcement imaging: concrete only sample (left) and one layer of 30 mm diameter parallel rebars with a spacing of 15 cm (right). 56
33 Distribution of the signal from a central region in ZX projection of the concrete-only case and a case with parallel rods. 57
34 Reinforcement imaging: single (left) and double (right) 30 mm diameter rebar grid with a spacing of 15 cm. 57
35 A single layer of a grid. 60
36 Reinforcement imaging before (left) and after background removal (right) for a standalone reinforcement grid of 15 mm diameter rebars. 60
37 Result of the auto-correlation approach for the example case. 62
38 Scheme of the column shift Δ_k, where b_{ij} is a bin number. 62
39 Result of the auto-correlation approach with additional shifts. 63
40 Result of the auto-correlation approach after triangular background subtraction. 63
41 A Fourier frequency spectrum for the example with 1.5 cm diameter bars and a 15 cm spacing. 64
42 Fourier frequency spectra for different rebar diameters with a fixed spacing of 15 cm 65
43 Zoomed version of the Fourier frequency spectra for different rebar diameters with a fixed spacing of 15 cm. 65
44 The amplitude of the peak at the frequency of 0.07 as a function of the bar diameter, where the spacing was fixed at 15 cm. 66
45 Fourier frequency spectra for different rebar spacings with a fixed rebar diameter of 8 mm. 66
46 A zoomed version of the Fourier frequency spectra for different rebar spacings with a fixed rebar diameter of 8 mm. 67
47 Normalized Fourier frequency spectra for a grid made of rebars with 6, 7 or 8 mm diameter and a spacing of 10 cm. 67
48 Zoomed version of the normalized Fourier frequency spectra for a grid made of rebars with 6, 7 or 8 mm diameter and a spacing of 10 cm. 68

49 Normalized Fourier frequency spectra for a grid made of rebars with 6, 7 or 8 mm diameter and a spacing of 10 cm. Two weeks equivalent of data were used. 69

50 Zoomed version of the normalized Fourier frequency spectra for a grid made of rebars with 6, 7 or 8 mm diameter and a spacing of 10 cm.Two weeks equivalent of data were used. 69

51 Amplitude of the peak at 0.1 of the normalized frequency spectra and a fixed spacing of 10 cm as a function of rebar diameter. 70

52 Normalized frequency spectra for rebars with 6, 7 or 8 mm diameter and spacing set to 20 cm. One week equivalent of data taking was used. 70

53 Zoomed version of the normalized frequency spectra for rebars with 6, 7 or 8 mm diameter and a fixed spacing of 20 cm. One week equivalent of data taking was. 71

54 Normalized frequency spectra for rebars with 6, 7 or 8 mm diameter and a spacing of 20 cm. Two weeks equivalent of data taking were used. 71

55 Zoomed version of the normalized frequency spectra for rebars of 6, 7 or 8 mm diameter and a spacing of 20 cm. Two weeks equivalent of data taking were used. 72

56 Amplitude of the peak at 0.05 of the normalized frequency spectra and a fixed spacing of 20 cm as a function of rebar diameter. 72

57 Normalized frequency spectra for grid made of 8 mm diameter rebars and spacing set to 10 cm, for the spatial resolution $R = 0.45$ mm, $R = 1$ mm or $R = 1.5$ mm. 74

58 Zoomed version of the normalized frequency spectra for a grid made with 8 mm diameter rebars and a spacing of 10 cm, for a spatial resolution $R = 0.45$ mm, $R = 1$ mm or $R = 1.5$ mm. 74

59 Amplitude of the peak at 0.1 of the normalized frequency spectra for a grid made with 8 mm diameter rebars and a spacing of 10 cm, for a spatial resolution $R = 0.45$ mm, $R = 1$ mm or $R = 1.5$ mm. 75

60 Normalized frequency spectra for a grid made with 8 mm diameter rebars and a spacing of 10 cm for different numbers of detector layers used for tracking with a spatial resolution per plane of 450 µm. 76

61 Zoomed version of the normalized frequency spectra for a grid made with 8 mm diameter rebars and a spacing of 10 cm for different numbers of detector layers used for tracking with a spatial resolution per plane of 450 µm. 76

62 The fraction of muons that fall in the acceptance of the muon detection system when using 3, 4, 5, 6 or 7 detector layers. 77

63 A sketch of the setup for the two layers scenario. 79

64 Images of the concrete block with two layers of the reinforcement grid, where the second grid is put at different depths. 80

65 Signal map of the ZX projection of the geometry with a second layer at a depth of D=0 cm. 80

66 Normalized frequency spectrum of a scenario with two reinforcement layers with the distance between them of D=20 cm. The depth of the sliding window was 7 cm. 81

67 Normalized frequency spectra of a scenario with two reinforcement layers, where the distance between them was D=20 cm. 81

68 Amplitude of the peak at 0.1 in the normalized Fourier spectra as a function of sliding window depth for grid distances between D=0 and D=40 cm. . . 82

69 A zoomed version of an amplitude of the peak at 0.1 in the normalized Fourier spectra as a function of sliding window depth for grid distances between D=0 and D=40 cm. 83

70 Reconstructed depth for the second rebar grid as a function of the distance between layers D. 83

71 Exploded view of an RPC. 86

72 Interior of one cassette. 87

73 The muon detection system. 88

74 Data format for the RPC data. 89

75 Raw ADC data as a function of strip number for an event without hit for one RPC. 89

76 Overlay of several raw ADC data events as a function of strip number for one board. 90

77 Zoomed version of the overlay of several raw ADC data events as a function of strip number for one board. 91

78 Pedestal as a function of strip number for board BY. 92

79 Pedestal as a function of strip number for all boards. 92

80 Noise as a function of strip number for all boards. 93

81 Raw ADC counts, pedestal and pedestal subtracted signal as a function of strip number. 93

82 Three examples of strip signal correlations. Linear correlation indicates that there is a significant common mode. 94

83 Distribution of the common mode noise for board DX. 95

84 Strip signals as a function of strip number after pedestal subtraction and pedestal subtraction and common mode noise correction. 95

85 Noise as a function of strip number for board BY before and after common mode (CM) correction. 96

86 A distribution of a difference in noise before and after common mode correction for board BY. 96
87 Noise as a function of strip number for all boards after common mode correction. 97
88 A sketch of a hit cluster. 98
89 An event that includes a hit before pedestal and common mode correction (left) and the same event after pedestal and common mode correction with a Gaussian fit to the strips with a hit (right). 98
90 A distribution of hit position in board DX. 99
91 A distribution of the hit size in board DX. 100
92 A distribution of the seed signal in board DX. 100
93 A distribution of the seed signal-to-noise ratio s/n in board DX. 101
94 A distribution of the total hit signal in board DX. 101
95 An example of a hit with a dead strip in the middle (left) and the hit after identifying and correction the signal dead strip (right). 102
96 An example of an inverted hit (left) and the event after inverting the ADC data (right). 102
97 Raw timestamp values for all boards as a function of event number. 103
98 Corrected timestamp values for all boards after initial shift as a function of event number. 103
99 Final timestamp as a function of event number for all boards. 104
100 A histogram of the number of hits on the track candidates in ZX and ZY projection. 104
101 The χ^2 of the track candidate fit in ZX and ZY direction. 105
102 Track slopes in the ZX and the ZY plane. 105
103 An event display in ZX projection. 106
104 Residuals for board DX for different χ^2 thresholds. 108
105 Images of a concrete block with and unknown content. 111
106 Energy deposition as a function of the depth in the body for an X-ray beam, a single proton beam and a Spread Out Bragg Peak (SOBP) combining proton beams with twelve different energies. 114
107 Scattering angle distributions for the four different materials using proton scattering techniques. 115
108 Metric image of the box with four cubes filled with different materials obtained with proton scattering tomography. 116
109 Sketch of the human phantom used in the simulation study. 117
110 A metric image of the phantom with ribs made from uranium. 118
111 A metric image of the phantom with ribs made from bone. 118
112 A metric image of the phantom with ribs made from soft tissue. 119

113 Background subtracted metric image for ribs made from bone. 119
114 An integral along Y axis combing all signal values. 120

List of Tables

1 Radiation lengths for relevant elements 31

2 Radiation lengths for relevant materials. 31

3 Composition of materials used in simulations. 40

4 Spatial resolution for every board. 108

5 Efficiency for every board. 109

References

[1] C Thomay. *Muon scattering tomography for nuclear security applications*. PhD thesis, University of Bristol, 2015.

[2] L Frazão. *Imaging and material identification of nuclear waste with muon scattering tomography*. PhD thesis, University of Bristol, 2019.

[3] P Baesso, D Cussans, C Thomay, JJ Velthuis, J Burns, C Steer, and S Quillin. A high resolution resistive plate chamber tracking system developed for cosmic ray muon tomography. *Journal of Instrumentation*, 8(08):P08006, 2013.

[4] Get it Right Initiative et al. Improving value by eliminating error. Research Report. `https://getitright.uk.com/live/files/reports/3-giri-research-report-revision-3-284.pdf`, 2016. Accessed: 2023-06-07.

[5] Cannon Steels Ltd. Rebar sizes: what you need to know. `https://www.cannonsteelsltd.co.uk/rebar-sizes-what-you-need-to-know/`. Accessed: 2021-02-10.

[6] Reinforcement Products Online. B785 Reinforcement Mesh. `https://www.reinforcementproductsonline.co.uk/b785-standard-mesh-2.html`. Accessed: 2021-02-21.

[7] L Frazão, JJ Velthuis, S Maddrell-Mander, and C Thomay. High-resolution imaging of nuclear waste containers with Muon Scattering Tomography. *Journal of Instrumentation*, 14(08):P08005, 2019.

[8] SK Verma, SS Bhadauria, and S Akhtar. Review of nondestructive testing methods for condition monitoring of concrete structures. *Journal of construction engineering*, 2013(2008):1–11, 2013.

[9] X Derobert, C Aubagnac, and O Abraham. Comparison of NDT techniques on a post-tensioned beam before its autopsy. *NDT & E International*, 35(8):541–548, 2002.

[10] O Büyüköztürk. Imaging of concrete structures. *Ndt & E International*, 31(4):233–243, 1998.

[11] GF Pla-Rucki and MO Eberhard. Imaging of reinforced concrete: State-of-the-art review. *Journal of infrastructure systems*, 1(2):134–141, 1995.

[12] BB Tefera and AG Tarekegn. Non-destructive testing techniques for condition assessment of concrete structures: A review. *American Journal of Civil Engineering*, 13(1):10–31, 2025.

[13] JH Bungey. Sub-surface radar testing of concrete: a review. *Construction and Building materials*, 18(1):1–8, 2004.

[14] A Tarussov, M Vandry, and A De La Haza. Condition assessment of concrete structures using a new analysis method: Ground-penetrating radar computer-assisted visual interpretation. *Construction and Building Materials*, 38:1246–1254, 2013.

[15] H Rathod, S Debeck, R Gupta, and B Chow. Applicability of GPR and a rebar detector to obtain rebar information of existing concrete structures. *Case Studies in Construction Materials*, 11:e00240, 2019.

[16] MA Almalki and KF Almutairi. Inspection of reinforced concrete structures using ground penetrating radar: Experimental approach. *Journal of King Saud University - Science*, 36(4):103140, 2024.

[17] B Milovanović and I Banjad Pečur. Review of active IR thermography for detection and characterization of defects in reinforced concrete. *Journal of Imaging*, 2(2):11, 2016.

[18] P Shrestha, O Avci, S Rifai, F Abla, M Seek, K Barth, and U Halabe. A review of infrared thermography applications for civil infrastructure. *Structural Durability and Health Monitoring*, 19(2), 2025.

[19] P Burrascano, S Callegari, A Montisci, M Ricci, and M Versaci. *Ultrasonic nondestructive evaluation systems: industrial application issues*. Springer, 2014.

[20] S Laureti, M Ricci, MNIB Mohamed, L Senni, LAJ Davis, and DA Hutchins. Detection of rebars in concrete using advanced ultrasonic pulse compression techniques. *Ultrasonics*, 85:31–38, 2018.

[21] T Arumaikani, S Sasmal, and T Kundu. Detection of initiation of corrosion induced damage in concrete structures using nonlinear ultrasonic techniques. *The Journal of the Acoustical Society of America*, 151(2):1341–1352, 2022.

[22] E Niederleithinger, S Maak, F Mielentz, UA Effner, C Strangfeld, and J Timofeev. *Review of recent developments in ultrasonic echo testing of concrete*. Bundesanstalt für Materialforschung und-prüfung (BAM), 2019.

[23] A du Plessis and WP Boshoff. A review of X-ray computed tomography of concrete and asphalt construction materials. *Construction and Building Materials*, 199:637–651, 2019.

[24] JR Moussa, D Harmon, and S Rane. Industrial radiography: Trends, market drivers, and alternatives to gamma-based devices. *Health Physics*, 129(3):174–183, 2025.

[25] Sardar KUR, Zainah I, Shazim AM, and Mohammed J. Nondestructive test methods for concrete bridges: A review. *Construction and Building Materials*, 107:58–86, 2016.

[26] N Gucunski, A Imani, F Romero, S Nazarian, D Yuan, H Wiggenhauser, P Shokouhi, A Taffe, and D Kutrubes. Nondestructive testing to identify concrete bridge deck deterioration, the second STRATEGIC HIGHWAY RESEARCH PROGRAM, REPORT S2R06ARR1.

[27] F Tosti and C Ferrante. Using ground penetrating radar methods to investigate reinforced concrete structures. *Surveys in Geophysics*, 41(3):485–530, 2020.

[28] K Knödel, G Lange, H Voigt, N Blindow, D Eisenburger, B Illich, H Petzold, and T Richter. Ground penetrating radar. *Environmental Geology: Handbook of Field Methods and Case Studies*, pages 283–335, 2007.

[29] C Maierhofer, M Röllig, and J Schlichting. Active thermography for evaluation of reinforced concrete structures. *Non-Destructive Evaluation of Reinforced Concrete Structures: Non-Destructive Testing Methods*, pages 370–402, 07 2010.

[30] A Ibrahim, N Faris, T Zayed, AH Qureshi, S Abdelkhalek, and EM Abdelkader. Application of infrared thermography in concrete bridge deck inspection: current practices, challenges and future needs. *Nondestructive Testing and Evaluation*, pages 1–44, 2024.

[31] DM McCann and MC Forde. Review of NDT methods in the assessment of concrete and masonry structures. *Ndt & E International*, 34(2):71–84, 2001.

[32] Krautkramer H Krautkramer J. Ultrasonic testing of materials, 1990.

[33] A Castellano, A Fraddosio, Mario D Piccioni, and T Kundu. Linear and nonlinear ultrasonic techniques for monitoring stress-induced damages in concrete. *Journal of Nondestructive Evaluation, Diagnostics and Prognostics of Engineering Systems*, 4(4):041001, 2021.

[34] M Schickert. Progress in ultrasonic imaging of concrete. *Materials and Structures*, 38:807–815, 2005.

[35] DM McCann and MC Forde. Review of NDT methods in the assessment of concrete and masonry structures. *NDT and E International*, 34(2):71–84, 2001.

[36] International Atomic Energy Agency. Manual on gamma radiography. `https://inis.iaea.org/collection/NCLCollectionStore/_Public/28/027/28027979.pdf`. Accessed: 2023-10-02.

[37] CERN. Cosmic rays: particles from outer space. https://home.cern/science/physics/cosmic-rays-particles-outer-space. Accessed: 2023-06-19.

[38] H Pleijel. Award ceremony speech, The Nobel Prize in Physics 1936. https://www.nobelprize.org/prizes/physics/1936/ceremony-speech. Accessed: 2023-06-19.

[39] M Tanabashi, K Hagiwara, K Hikasa, Katsumasa Nakamura, Y Sumino, F Takahashi, J Tanaka, K Agashe, G Aielli, Claude Amsler, et al. Review of Particle Physics: particle data groups. *Physical Review D*, 98(3):1–1898, 2018.

[40] I Morison. *Introduction to astronomy and cosmology.* John Wiley & Sons, 2008.

[41] G Bachmann and CGG Kirchberg. Cosmic rays. https://indico.cern.ch/event/318730/attachments/613330/843782/Cosmic_Radiation_LessonPlans.pdf. Accessed: 2023-06-20.

[42] MP De Pascale, A Morselli, P Picozza, RL Golden, C Grimani, BL Kimbell, SA Stephens, SJ Stochaj, WR Webber, G Basini, et al. Absolute spectrum and charge ratio of cosmic ray muons in the energy region from 0.2 GeV to 100 GeV at 600 m above sea level. *Journal of Geophysical Research: Space Physics*, 98(A3):3501–3507, 1993.

[43] PKF Grieder. *Cosmic rays at Earth.* Elsevier, 2001.

[44] D Reyna. A simple parameterization of the cosmic–ray muon momentum spectra at the surface as a function of zenith angle. *arXiv preprint hep-ph/0604145*, 2006.

[45] DE Groom, NV Mokhov, and SI Striganov. Muon stopping power and range tables 10 MeV-100 TeV. *Atomic Data and Nuclear Data Tables*, 78(2):183–356, 2001.

[46] Particle Data Group. Atomic and nuclear properties of materials for more than 350 materials. https://pdg.lbl.gov/2022/AtomicNuclearProperties/index.html. Accessed: 2023-06-07.

[47] LW Alvarez, JA Anderson, F El Bedwei, J Burkhard, A Fakhry, A Girgis, A Goneid, F Hassan, D Iverson, G Lynch, et al. Search for hidden chambers in the pyramids. *Science*, 167(3919):832–839, 1970.

[48] K Morishima, M Kuno, A Nishio, N Kitagawa, Y Manabe, M Moto, F Takasaki, H Fujii, K Satoh, H Kodama, et al. Discovery of a big void in Khufu's Pyramid by observation of cosmic-ray muons. *Nature*, 552(7685):386–390, 2017.

[49] K Nagamine, M Iwasaki, K Shimomura, and K Ishida. Method of probing inner-structure of geophysical substance with the horizontal cosmic-ray muons and possible application to volcanic eruption prediction. *Nuclear Instruments and*

Methods in Physics Research Section A: Accelerators, Spectrometers, Detectors and Associated Equipment, 356(2-3):585–595, 1995.

[50] HKM Tanaka, K Nagamine, SN Nakamura, and K Ishida. Radiographic measurements of the internal structure of Mt. West Iwate with near-horizontal cosmic-ray muons and future developments. *Nuclear Instruments and Methods in Physics Research Section A: Accelerators, Spectrometers, Detectors and Associated Equipment*, 555(1):164–172, 2005.

[51] G Ambrosi, F Ambrosino, R Battiston, A Bross, S Callier, F Cassese, G Castellini, R Ciaranfi, F Cozzolino, R D'Alessandro, et al. The MU-RAY project: Volcano radiography with cosmic-ray muons. *Nuclear Instruments and Methods in Physics Research Section A: Accelerators, Spectrometers, Detectors and Associated Equipment*, 628(1):120–123, 2011.

[52] C Carloganu, V Niess, S Béné, E Busato, P Dupieux, F Fehr, P Gay, D Miallier, B Vulpescu, P Boivin, et al. Towards a muon radiography of the Puy de Dôme. *Geoscientific Instrumentation, Methods and Data Systems*, 2:55–60, 2013.

[53] D Carbone, D Gibert, J Marteau, M Diament, L Zuccarello, and E Galichet. An experiment of muon radiography at Mt Etna (Italy). *Geophysical Journal International*, 196(2):633–643, 10 2013.

[54] M Tramontini, M Rosas-Carbajal, FI Zyserman, L Longuevergne, C Nussbaum, and J Marteau. Defining the sensitivity of cosmic ray muons to groundwater storage changes. *Comptes Rendus. Géoscience*, 356(G1):177–194, 2024.

[55] N Bonal, AT. Cashion, IV, G Cieslewski, DJ. Dorsey, A Foris, TJ. Miller, BL. Roberts, JC Su, W Dreesen, JA Green, et al. Using muons to image the subsurface. Technical report, Sandia National Laboratories (SNL), Albuquerque, NM, and Livermore, CA (United States), 11 2016.

[56] A Bonneville, R Kouzes, J Yamaoka, A Lintereur, J Flygare, GS Varner, I Mostafanezhad, E Guardincerri, C Rowe, and R Mellors. Borehole muography of subsurface reservoirs. *Philosophical Transactions of the Royal Society A*, 377(2137):20180060, 2019.

[57] F Riggi. *Messengers from the Cosmos: An Introduction to the Physics of Cosmic Rays in Its Historical Evolution.* Springer Nature, 2023.

[58] C Thomay, JJ Velthuis, T Poffley, P Baesso, D Cussans, and L Frazão. Passive 3D imaging of nuclear waste containers with muon scattering tomography. *Journal of Instrumentation*, 11(03):P03008, 2016.

[59] LJ Schultz. *Cosmic ray muon radiography.* PhD thesis, Portland State University Portland, OR, USA, 2003.

[60] LJ Schultz, GS Blanpied, KN Borozdin, AM Fraser, NW Hengartner, AV Klimenko, CL Morris, C Orum, and MJ Sossong. Statistical reconstruction for cosmic ray muon tomography. *IEEE transactions on Image Processing*, 16(8):1985–1993, 2007.

[61] M Stapleton, J Burns, S Quillin, and C Steer. Angle Statistics Reconstruction: a robust reconstruction algorithm for Muon Scattering Tomography. *Journal of Instrumentation*, 9(11):P11019, 2014.

[62] LJ Schultz, KN Borozdin, JJ Gomez, GE Hogan, JA McGill, CL Morris, WC Priedhorsky, A Saunders, and ME Teasdale. Image reconstruction and material Z discrimination via cosmic ray muon radiography. *Nuclear Instruments and Methods in Physics Research Section A: Accelerators, Spectrometers, Detectors and Associated Equipment*, 519(3):687–694, 2004.

[63] C Thomay, JJ Velthuis, P Baesso, D Cussans, PAW Morris, C Steer, J Burns, S Quillin, and M Stapleton. A binned clustering algorithm to detect high-Z material using cosmic muons. *Journal of Instrumentation*, 8(10):P10013, 2013.

[64] C Thomay, JJ Velthuis, P Baesso, D Cussans, C Steer, J Burns, S Quillin, and M Stapleton. A novel Markov random field-based clustering algorithm to detect high-Z objects with cosmic rays. *IEEE Transactions on Nuclear Science*, 62(4):1837–1848, 2015.

[65] L Frazão, J Velthuis, C Thomay, and C Steer. Discrimination of high-Z materials in concrete-filled containers using muon scattering tomography. *Journal of Instrumentation*, 11(07):P07020, 2016.

[66] M Dobrowolska, JJ Velthuis, L Frazão, and D Kikoła. A novel technique for finding gas bubbles in the nuclear waste containers using Muon Scattering Tomography. *Journal of Instrumentation*, 13(05):P05015, 2018.

[67] S Agostinelli, J Allison, K al Amako, J Apostolakis, H Araujo, P Arce, M Asai, D Axen, S Banerjee, G Barrand, et al. GEANT4 a simulation toolkit. *Nuclear instruments and methods in physics research section A: Accelerators, Spectrometers, Detectors and Associated Equipment*, 506(3):250–303, 2003.

[68] CJ Josey, AR Clark, JA Kulesza, EJ Pearson, and ME Rising. MCNP® Code Version 6.3.0 Verification & Validation Testing. Technical Report LA-UR-22-32951, Rev. 1, Los Alamos National Laboratory, Los Alamos, NM, USA, 12 2022.

[69] A Lechmann, D Mair, A Ariga, T Ariga, A Ereditato, R Nishiyama, C Pistillo, P Scampoli, M Vladymyrov, and F Schlunegger. SMAUG v1. 0–a user-friendly muon simulator for the imaging of geological objects in 3-D. *Geoscientific Model Development*, 15(6):2441–2473, 2022.

[70] N Zurlo, G Bonomi, A Donzella, D Pagano, A Zenoni, G Zumerle, et al. A new Monte Carlo muon generator for cosmic-ray muon applications. *POS PROCEEDINGS OF SCIENCE*, 409, 2022.

[71] D Heck, J Knapp, JN Capdevielle, G Schatz, T Thouw, et al. Corsika: A monte carlo code to simulate extensive air showers. *Report fzka*, 6019(11), 1998.

[72] P Biallass and T Hebbeker. Parametrization of the cosmic muon flux for the generator CMSCGEN. *arXiv preprint arXiv:0907.5514*, 2009.

[73] G Battistoni, A Margiotta, S Muraro, and M Sioli. FLUKA as a new high energy cosmic ray generator. *Nuclear Instruments and Methods in Physics Research Section A: Accelerators, Spectrometers, Detectors and Associated Equipment*, 626:S191–S192, 2011.

[74] G Carminati, M Bazzotti, A Margiotta, and Maurizio Spurio. Atmospheric MUons from PArametric formulas: a fast GEnerator for neutrino telescopes (MUPAGE). *Computer Physics Communications*, 179(12):915–923, 2008.

[75] C Hagmann, D Lange, and D Wright. Cosmic ray shower generator (CRY) for monte carlo transport codes. In *Nuclear Science Symposium Conference Record, 2007. NSS'07. IEEE*, volume 2, pages 1143–1146. IEEE, 2007.

[76] P Baesso, D Cussans, C Thomay, and JJ Velthuis. Toward a RPC-based muon tomography system for cargo containers. *Journal of Instrumentation*, 9(10):C10041, 2014.

[77] M Dobrowolska, JJ Velthuis, A Kopp, C De Sio, R Milne, and P Pearson. Development of muon scattering tomography for a detection of reinforcement in concrete. *Engineering Research Express*, 3(3):035037, 2021.

[78] M Dobrowolska, JJ Velthuis, A Kopp, M Perry, and P Pearson. Towards an application of muon scattering tomography as a technique for detecting rebars in concrete. *Smart Materials and Structures*, 29(5):055015, 2020.

[79] ROOT. TVirtualFFT Class Reference. `https://root.cern.ch/doc/master/classTVirtualFFT.html`. Accessed: 2023-06-19.

[80] M Dobrowolska, JJ Velthuis, C De Sio, A Kopp, R Milne, and P Pearson. Development of muon scattering tomography for detection of reinforcement in concrete. *Journal of Instrumentation*, 17(09):C09011, 2022.

[81] GF Knoll. *Radiation detection and measurement.* John Wiley & Sons, 2010.

[82] WJ Llope. Multigap RPCs in the STAR experiment at RHIC. *Nuclear Instruments and Methods in Physics Research Section A: Accelerators, Spectrometers, Detectors and Associated Equipment*, 661:S110–S113, 2012. X. Workshop on Resistive Plate Chambers and Related Detectors (RPC 2010).

[83] X Dong, L Ruan, M Shao, Y Sun, Z Tang, Z Xu, W Zha, and Y Zhang. Dilepton program with time-of-flight detector at the STAR experiment. *Symmetry*, 15(2), 2023.

[84] MA Shah, R Hadjiska, A Fagot, M Gul, C Roskas, M Tytgat, N Zaganidis, S. Fonseca De Souza, A Santoro, and F et al Torres Da Silva. The CMS RPC detector performance and stability during LHC RUN-2. *Journal of Instrumentation*, 14(11):C11012, 2019.

[85] D Ramos, G Pugliese, G Iaselli, J Eysermans, KS Lee, M Kang, and Y Jo. Characterization of a innovative RPC prototype with 1.0 mm of gas gap thickness. *Nuclear Instruments and Methods in Physics Research Section A: Accelerators, Spectrometers, Detectors and Associated Equipment*, 1055:168460, 2023.

[86] A Ferretti. The upgrade of the RPC-based ALICE Muon Trigger. *Journal of Instrumentation*, 14(06):C06011, 2019.

[87] GL Alberghi. Status of the present ATLAS RPC system and overview towards HL-LHC. *Journal of Instrumentation*, 14(10):C10018, 2019.

[88] R Guida, M Capeans, and B Mandelli. Characterization of RPC operation with new environmental friendly mixtures for LHC application and beyond. *Journal of Instrumentation*, 11(07):C07016, 2016.

[89] Gianluca R, Roberto G, and Beatrice M. Studies on RPC detectors operated with environmentally friendly gas mixtures in LHC-like conditions. *Nuclear Instruments and Methods in Physics Research Section A: Accelerators, Spectrometers, Detectors and Associated Equipment*, 1048:167961, 2023.

[90] S Blin, P Barrillon, and Ch de La Taille. MAROC, a generic photomultiplier readout chip. *Journal of Instrumentation*, 5(12):C12007, 2010.

[91] R Frazier, G Iles, M Magrans de Abril, D Newbold, A Rose, D Sankey, and T Williams. The IPbus Protocol: An IP-based control protocol for ATCA, 2013.

[92] J Kodosky. LabVIEW. *Proceedings of the ACM on Programming Languages*, 4(HOPL):1–54, 2020.

[93] JJ Velthuis, Z Drasal, G Hanninger, R Kohrs, M Mathes, L Reuen, D Scheirich, L Andricek, I Carbonell Pascual, X Chen, et al. A DEPFET based beam telescope with submicron precision capability. *IEEE Transactions on Nuclear Science*, 55(1):662–666, 2008.

[94] E Bär, A Lalonde, G Royle, H-M Lu, and H Bouchard. The potential of dual-energy CT to reduce proton beam range uncertainties. *Medical physics*, 44(6):2332–2344, 2017.

[95] H Paganetti. Range uncertainties in proton therapy and the role of Monte Carlo simulations. *Physics in Medicine & Biology*, 57(11):R99, 2012.

[96] M De Simoni, M Fischetti, E Gioscio, M Marafini, R Mirabelli, V Patera, A Sarti, A Schiavi, A Sciubba, and G Traini. FRED: a fast Monte Carlo code on GPU for quality control in Particle Therapy. In *Journal of Physics: Conference Series*, volume 1548, page 012020. IOP Publishing, 2020.

[97] M Esposito, C Waltham, JT Taylor, S Manger, B Phoenix, T Price, S Poludniowski, Gand Green, PM Evans, PP Allport, et al. PRaVDA: the first solid-state system for proton computed tomography. *Physica Medica*, 55:149–154, 2018.

[98] RW Schulte and SN Penfold. Proton CT for improved stopping power determination in proton therapy, invited. *Transactions of the American Nuclear Society*, 106:55, 2012.

[99] J Dickmann, S Rit, M Pankuch, RP Johnson, RW Schulte, K Parodi, G Dedes, and G Landry. An optimization algorithm for dose reduction with fluence-modulated proton CT. *Medical physics*, 47(4):1895–1906, 2020.

[100] M Aehle, J Alme, GG Barnaföldi, T Bodova, V Borshchov, A van den Brink, M Chaar, V Eikeland, G Feofilov, C Garth, et al. The bergen proton CT system. *Journal of Instrumentation*, 18(02):C02051, 2023.

[101] S Guatelli, B Mascialino, MG Pia, and W Pokorski. Geant4 anthropomorphic phantoms. In *2006 IEEE Nuclear Science Symposium Conference Record*, volume 3, pages 1359–1362. IEEE, 2006.

[102] WS Snyder, MR Ford, and GG Warner. Revision of MIRD pamphlet No. 5 entitled"estimates of absorbed fractions for monoenergetic photon sources uniformly distributed in various organs of a heterogeneous phantom". Technical report, 1974.

[103] I Sedgwick, D Das, N Guerrini, B Marsh, and R Turchetta. LASSENA: A 6.7 megapixel, 3-sides buttable wafer-scale CMOS sensor using a novel grid-addressing architecture. *Proc Int Image Sens Work*, pages 3–6, 2013.

[104] R Mohan and D Grosshans. Proton therapy-present and future. *Advanced drug delivery reviews*, 109:26–44, 2017.

[105] Ka Manikantan, S Khode, SI Sayed, J Roe, CM Nutting, P Rhys-Evans, KJ Harrington, and R Kazi. Dysphagia in head and neck cancer. *Cancer treatment reviews*, 35(8):724–732, 2009.